Chem Soc Rev

A Critical Review on Cathodes for Rechargeable Mg batteries

Journal:	*Chemical Society Reviews*
Manuscript ID	CS-SYN-04-2018-000319.R3
Article Type:	Review Article
Date Submitted by the Author:	27-Sep-2018
Complete List of Authors:	Mao, Minglei; Hunan University College of Chemistry and Chemical Engineering Gao, Tao; University of Maryland at College Park Hou, Singyuk; University of Maryland, Department of Chemical & Biomolecular Engineering Wang, Chunsheng; University of Maryland, Department of Chemical & Biomolecular Engineering

A Critical Review on Cathodes for Rechargeable Mg Batteries

Minglei Mao,[ab] Tao Gao,*[a] Singyuk Hou,[a] Chunsheng Wang*[a]

Received 00th January 20xx,
Accepted 00th January 20xx

DOI: 10.1039/x0xx00000x

www.rsc.org/

Benefit from higher volumetric capacity (3833 mA h/cm^3 for Mg vs. 2046 mA h/cm^3 for Li) and dendrite-free Mg metal anode, reversible Mg batteries (RMBs) is a promising chemistry for beyond Li ion batteries. However, RMB is still severely restricted by the absence of high performance cathodes for any practical application. In this review, we provide a critical and rigorous review on Mg battery cathode materials mainly reported since 2013, focusing on the impact of structure and composition on magnesiation kinetics. We discuss cathode materials including intercalation compounds, conversion materials (O_2, S, organic compounds), water co-intercalation cathodes (V_2O_5, MnO_2 et al), as well as hybrid systems using Mg metal anode. Among them, intercalation cathodes are further categorized by 3D (Chevrel phase, spinel structure et al), 2D (layered structure), and 1D materials (polyanion: phosphate and silicate), according to the diffusion pathway of Mg^{2+} in the framework. Instead of discussing every published work in detail, this review selects the most representative works and highlight the merits and challenges of each class of cathodes. The advance in theoretical analysis is also reviewed and compared with experimental results. This critical review will provide comprehensive knowledge of Mg cathodes and guideline for exploring new cathodes for rechargeable magnesium batteries.

1. Introduction

Since its invention in 1991, Li-ion batteries (LIBs) have gradually become the dominant mobile power source for various applications, especially for consumer electronics. With over two decades innovation and engineering in materials and cell design, the energy density of LIBs has reached 240 Wh/kg and 670 Wh/L at the cell level.[1, 2] However, a ceiling in capacity and energy density is expected when LIBs approach the theoretical limitation of intercalation chemistry.[1-3] Rechargeable metal batteries, which pair metal anodes with various cathode materials, offer great promise for further improving battery energy density, because metal anodes provide much higher capacity and lower reduction potential than intercalation anodes (Fig. 1a). Among all metal anodes, the high capacity (especially volumetric capacity of 3833 mA h/cm^3 for Mg vs. 2046 mA h/cm^3 for Li), low reduction potential (-2.4 V vs. SHE) and most importantly, dendrite-free deposition with 100% coulombic efficiency in some electrolytes make Mg metal an ideal anode.[4] For this reason, there is a growing interest to develop rechargeable Mg batteries during the past decade, especially after 2013 (Fig. 1b).

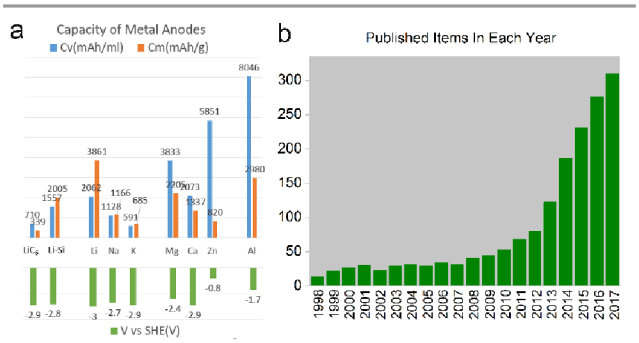

Fig. 1 (a) Capacity and redox potential of various metal anodes; (b) Publication numbers in the past two decades on the topic of "magnesium batteries"

Due to its bivalent nature, the diffusion of Mg^{2+} in solid state cathode materials is much more sluggish than monovalent cations like Li^+, which leads to large voltage hysteresis and low magnesiation degree for most materials.[5-7] For this reason, finding cathode materials with acceptable kinetics has become the major challenge for the development of rechargeable Mg batteries. In this review, we will retrospect efforts in this field, especially those made after 2013, with a special emphasis on the influence of structure and composition on magnesiation kinetics.

This review is organized as follows: major attention will be focused on intercalation materials, followed by conversion materials. Elemental redox chemistries will be discussed in some details due to their unique advantages of either high

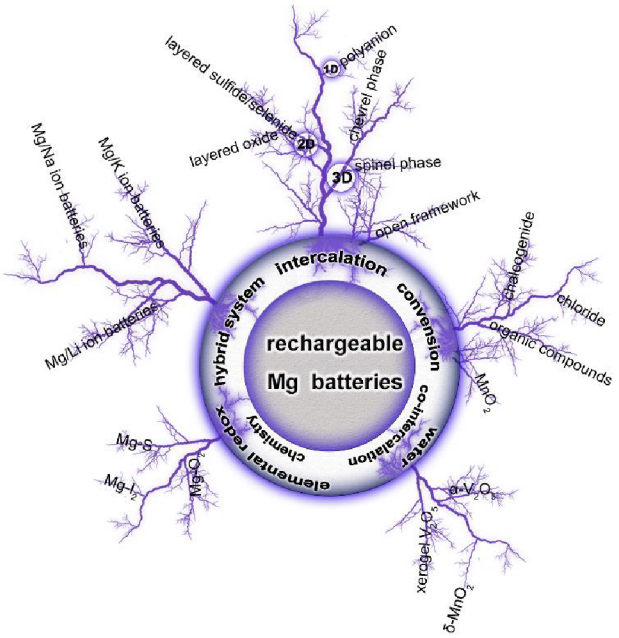

Fig. 2 An overview of cathodes for rechargeable Mg batteries.

[a] Department of Chemical and Biomolecular Engineering, University of Maryland, College Park, Maryland 20742, United States. E-mail: taogao@umd.edu cswang@umd.edu
[b] College of Chemistry and Chemical Engineering, Hunan University, Changsha 410082, China

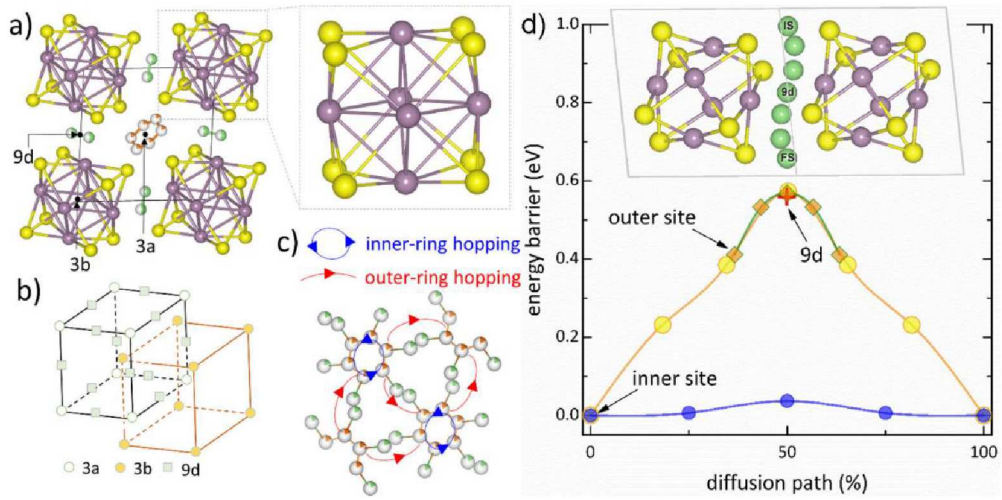

Fig. 3 Crystalline structure and sublattices in Chevrel phase Mo_6S_8. (a) Mo_6S_8 superanion and positions of highly symmetric 3a, 3b, and 9d sites (viewed along the [211] direction. (b) Sublattice of 3a and 3b sites. (c) Outer-ring and inner-ring hopping between partially occupied inner and outer sites. (d) NEB path for the hopping in Chevrel phase Mo_6S_8 at dilute Mg concentrations. Reproduced from ref. 18 with permission from American Chemical Society, Copyright 2017.

capacity or fast kinetics, while promising organic cathode materials, water co-intercalation cathode materials and hybrid battery systems are also briefly reviewed (Figure 2). We will not elaborate on every individual cathode material, but emphasize the most representative cathodes. The theoretical and experimental results will be compared to highlight the merits and challenges of each class of cathode materials. We hope this review can provide insights on the frontier of this emerging but not fully exploited field.

2. Intercalation

Intercalation compounds are the only commercialized cathode materials for rechargeable LIBs, because the topotactic intercalation reaction maintains their structure during discharge/charge, which guarantees good cycling stability and fast Li-ion diffusion.[2, 8, 9] Also, intercalation compounds are most investigated for rechargeable magnesium batteries (RMBs).

The kinetics of Mg intercalation are intrinsically dependent on the ion mobility in these materials. In general, ion mobility is mainly determined by three structural factors: (1) connectivity between sites; (2) sizes of the diffusion channel/cavity and intercalant; (3) and interaction strength between the intercalant and host structure. The site connectivity divide cathode materials into 3D, 2D or 1D intercalation topology, which in turn affects the diffusion behavior of a material dramatically as, in principle, a well-distributed diffusion network should facilitate mobility by providing improved tolerance towards defects and changes in lattice parameters.[10, 11] Moreover, the channel size should be large enough to accommodate the intercalant. Finally, high mobility is facilitated by weak interaction between the intercalant and host anion lattice.

Ab initio quantum calculation also confirms that multivalent cation diffusion is firstly dependent on structure,[12] which determines the diffusion pathway, and then on its chemistry, which determines the interactions between the intercalant and the host anion lattice.[7, 13] In different structures, coordination preference of the multivalent cation dictates the energy level change during their migration along the possible diffusion pathways, so that structures where the intercalants occupy its non-preferred coordination can reduce the migration energy barrier to ~525-650 meV, a value necessary for acceptable migration kinetics at room temperature.

In the below section, we will try to discuss how the structure affects the mobility and intercalation kinetics of Mg^{2+} based on current experimental and theoretical understanding, especially in spinel, layered, olivine cathodes. We will expand our discussion starting from structures with 3D diffusion channels (Chevrel phase, spinel), and then structures with 2D diffusion channels (layered structure) and finally to structures with 1D diffusion channel (polyanion compounds).

2.1 Chevrel phase

Chevrel phase (CP) (Mo_6S_8) is the first intercalation cathode that shows reversible Mg storage capability.[14-17] It has a unique structure where six Mo atoms reside on the faces of a cube forming an octahedron (Mo_6) and eight S anions (S_8) occupying the corners of the cube (Fig. 3a).[18-20] Therefore, its structure possesses a quasi-simple-cubic packing of the Mo_6S_8 superanions, in which 3a and 9b sites form 3D channels that are available for Mg^{2+} transport.[19] The unique metallic electronic structure of CP allows the easy accommodation of electrons, because within Mo_6 the electronic bonding is non-directional and orbitals are highly delocalized. The neutralizing electrons do not reside entirely (nor predominantly) on the Mo_6 clusters, but instead on the anions (S_8 clusters). The charge carried by Mg^{2+} is mostly balanced by the S atoms, resulting in a screening cloud that can effectively shield its 2+ charge.[21] In one word, the highly delocalized orbitals and a screening cloud contribute to realizing the fast diffusion of Mg^{2+} at room temperature.

Generally, a migration barrier of ~525 meV corresponds to ionic diffusivity of ~10^{-12} cm^2 s^{-1} at room temperature, representing the low limit for reasonable charge and discharge time (~2 h in micron-size active particles). An increase/decrease

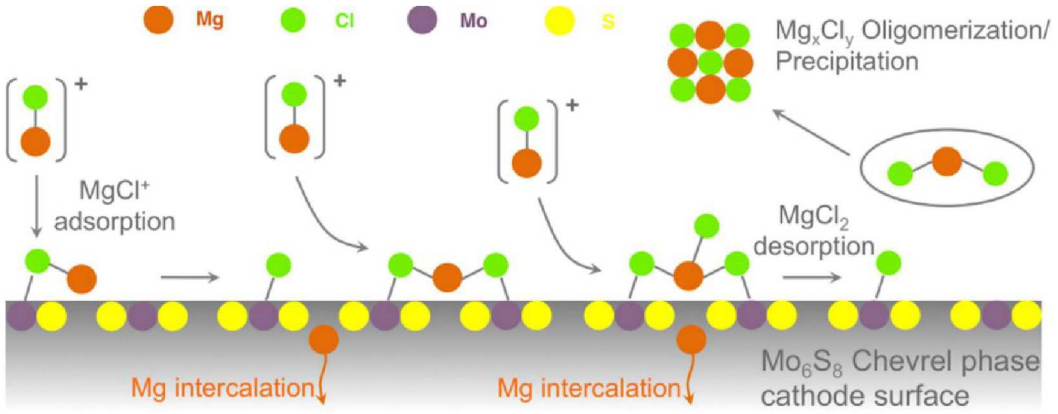

Fig. 4 Mg desolvation and absorption in Mo_6S_8 from Cl^--containing electrolyte. Reproduced from ref. 25 with permission from American Chemical Society, Copyright 2015.

of 60 meV in the migration energy corresponds to an order of magnitude decrease/increase in the diffusion. Since diffusion time scales to the square of length, larger barriers can be tolerated with smaller particle size: every order of magnitude in size reduction allows for two orders of magnitude smaller diffusion constant.[13] Meanwhile, an increase in temperature can reduces the diffusion barrier.[22-24] Based on nudged elastic band (NEB) calculation, the inner-ring and out-ring diffusion energy barriers of CP are estimated to be 40 meV and 570 meV, respectively, at dilute Mg concentration (Fig. 3d),[18] which explains the fast diffusion of Mg in CP.

Besides fast Mg^{2+} diffusion, the special structure of CP also facilitates the charge transfer at the interface by aiding the desolvation process.[25] In a typical Mg electrolyte based on transmetalation reaction between Grignard reagent and Lewis acid like $AlCl_3$, Mg exists in the electrolyte in the form of a complex cation, e.g. $Mg_2Cl_3^+$. The intercalation of Mg cation needs first to peel Mg^{2+} from the complex cation. Mo atoms on the CP surface act as a catalyst to reduce the required energy from 3000 meV to 200 meV, which facilitates the breaking of Mg-Cl bond. Once Mg is intercalated, it leaves the counter ion (Cl^-), on the surface, bound to Mo (Fig. 4).[25] The chlorinated surface continues to interact with incoming $MgCl^+$ species and form the neutral $MgCl_2$ unit, which may be released from these surface adsorbates to reopen Mo sites on the surface and permit continuous Mg-Cl bond breaking.

Benefiting from the high mobility of Mg^{2+} and fast interfacial charge transfer, Mo_6S_8 has been the most successful cathode material at room temperature up to now, which exhibits an excellent intercalation kinetics and reversibility with a capacity of 120 mA h/g at 1.2 V.[4]

As mentioned, reducing particle size will result in shorter Mg^{2+} diffusion length, thus improving the intercalation kinetics. To investigate that, the electrochemical performance of nanosized and microsized Mo_6S_8 were compared.[26] During the first discharge process, the overpotential for nanoparticles to initiate the first Mg^{2+} intercalation was noticeably lower than microparticles. During charge, more Mg^{2+} were extracted and the trapping effect for nanoparticles was reduced. In addition, the kinetics of the stabilized electrochemical reaction for nanoparticles was better.

A mathematical model was developed to investigate the performance limiting factors of Mg/Mo_6S_8 battery systems.[27] Limitation analysis indicates that the solid diffusion and kinetics in the higher voltage plateau limit the capacity and increase the overpotential in the thin (20 μm) electrodes. The polarization losses on charge is higher than that on discharge, because of the differences in the kinetics and solid diffusion between the two reactions of the Chevrel phase. Also, the model reveals that the

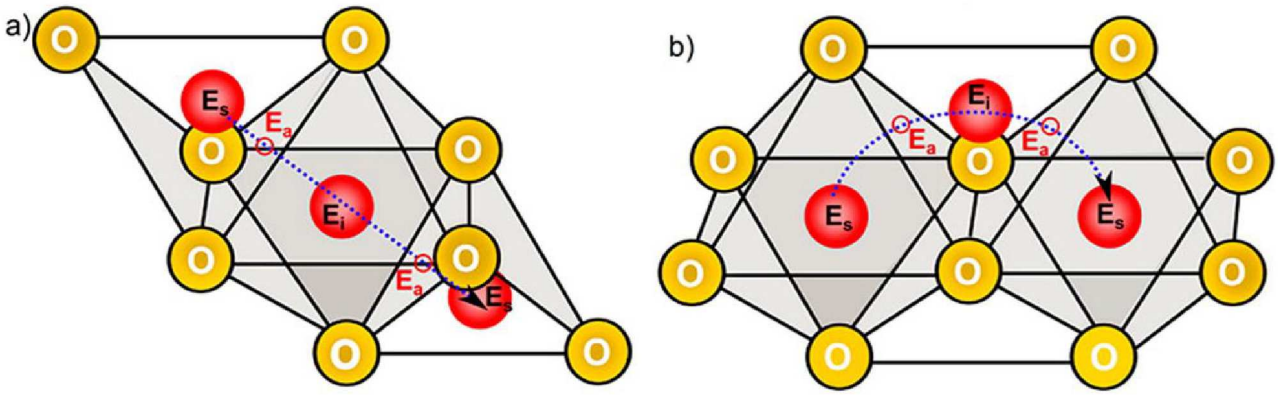

Fig. 5 Low-energy ion migration paths in close-packed oxides adopt either (a) tet → oct → tet or (b) oct → tet → oct diffusion topologies: stable insertion sites (Es), active sites (Ea), and intermediate site (Ei). Reproduced from ref. 12 with permission from American Chemical Society, Copyright 2015.

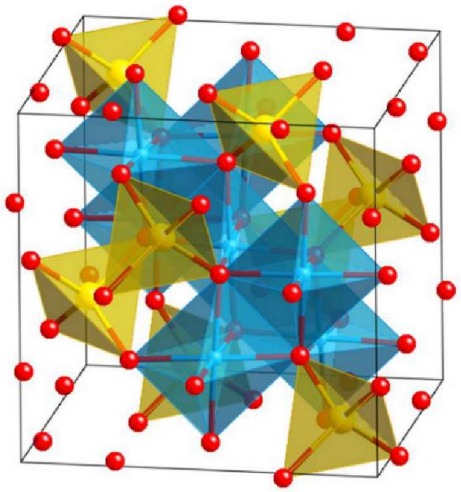

Fig. 6 Crystal structure of spinel MgT_2X_4. The Mg atoms sit within the yellow tetrahedral and the T atoms sit within the blue octahedral. The T atoms can be Ti, V, Cr, Mn, Fe, Co, Ni, and the anion X can be O, S, or Se.

performance of the cells with practical electrode thickness (80 μm) would be subject to electrolyte-phase limitations.

In short, the low voltage and capacity of Mo_6S_8 remain a major limitation, which encourages extensive efforts on other high voltage or capacity intercalation materials. Among them, spinel structures have received a particular attention.

2.2 Spinel: from oxide to sulfide

In the close-packed oxygen (or sulfur) structures (face-centered cubic fcc for spinel and layered, and hexagonal close-packed hcp for olivine), the diffusion path for Mg alternates through tetrahedral and octahedral sites along zigzag-shaped paths, leading to diffusion topologies that are either tet → oct → tet (Fig. 5a) or oct → tet → oct (Fig. 5b) (tri-vacancy hops) depending on which site is stable.[12] In a normal spinel, the intercalating Mg^{2+} initially resides in the stable tetrahedral site (with energy Es), then migrates through a three-coordinated oxygen face (with energy Ea) shared with the adjacent intermediate octahedral site (with energy Ei), and finally follows a symmetric path to the next equivalent stable site (Fig. 5a). In the layered and olivine structures, diffusion proceeds in a similar fashion but between stable octahedral sites through an intermediate tetrahedral site (Fig. 5b). Spinel compounds belong to space group Fd3m with the general formula MgT_2X_4. The anion X can be O, S, or Se. The cation T is octahedrally coordinated by X, and these edge-sharing octahedra extend in space and create 3D diffusion channels (Fig. 5a and 6).[12] The Mg diffusion energy barrier in spinel structure with different transitional metal (T = Ti, V, Cr, Mn, Fe, Co, Ni) were calculated and compared.[13] Results show that the transition metal chemistry does not significantly affect the Mg^{2+} diffusion barriers, which all lie within ~600 to 800 meV in the empty lattice limit, higher than the ~525 meV threshold. Therefore, Mg^{2+} intercalation into those spinel oxides are not likely, unless elevating the temperature and/or using nanosized particles. Despite Cr_2O_4, Ni_2O_4, and Co_2O_4 have slightly smaller diffusion barrier, spinel Mn_2O_4 (Fig. 7a) is considered as a better spinel oxide cathode when thermodynamic properties are also considered, since it has a high voltage and volumetric capacity and acceptable volume change (less than 15%), and more importantly, both its charged and discharged state are thermodynamically stable.[13]

Based on the calculated results, spinel Mn_2O_4 (λ-MnO_2) with various sizes and morphologies have been investigated in non-aqueous electrolytes.[28-30] The nanoflakes of λ-MnO_2 (~50 nm in thickness and several hundred nanometers in diameter) show a quite low degree of Mg^{2+} intercalation (<3 at. % Mg per Mn_2O_4) and extremely high voltage hysteresis in $Mg(TFSI)_2$-diglyme or propylene carbonate (PC) electrolyte at RT (Fig. 8a, b).[29] Other than kinetic limitation, a phase transformation from cubic spinel Mn_2O_4 to tetragonal spinel $MgMn_2O_4$ during Mg^{2+} intercalation is also cited as a probable cause for the low magnesiation degree.[28] The tetragonal spinel structure, a partially inverted spinel with a majority of Mn(III) in the octahedral site as well as a fraction of Mn(IV) and Mn(II) in the octahedral and tetrahedral sites, respectively, is considered to block the Mg^{2+} intercalation. To demonstrate that, both phases were cycled in the same electrolyte, separately, and the cubic phase exhibited reversible Mg^{2+} electrochemical activity with charge capacity approaching 250 mA h/g (in theory: 270 mA h/g),[28] while no significant

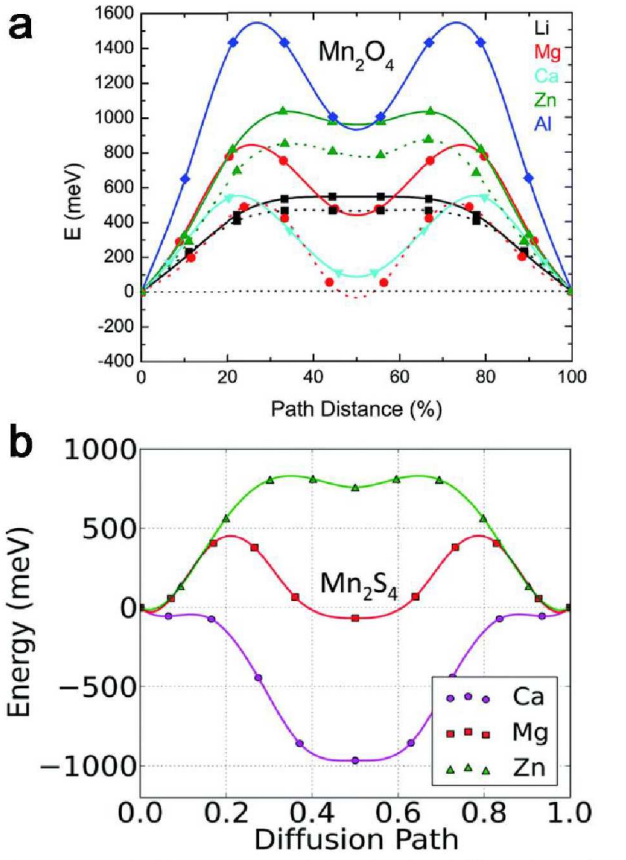

Fig. 7 Computed minimum energy paths for migration of different intercalants between the tetrahedral sites in (a) spinel Mn_2O_4 at the high vacancy limit (solid line) and dilute vacancy limit (dotted line). Reproduced from ref. 13 with permission from Royal Society Chemistry, Copyright 2015. (b) Thiospinel Mn_2S_4 within dilute limit of cation insertion. Reproduced from ref. 7 with permission from Royal Society Chemistry, Copyright 2016.

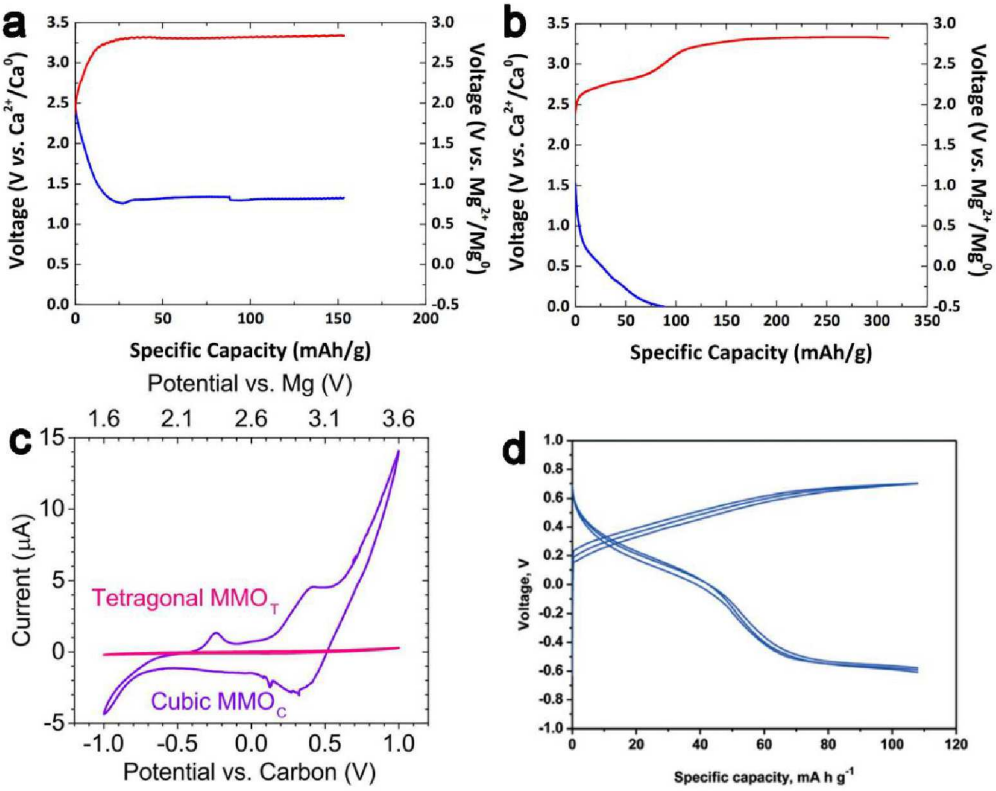

Fig. 8 (a) and (b) voltage vs. capacity profiles for 3-electrode cells with Mn_2O_4 (made by delithiation of $LiMn_2O_4$) working electrodes, using 0.2 M $Mg(TFSI)_2$ in diglyme (G2) and propylene carbonate (PC) as electrolytes, respectively. Reproduced from ref. 29 with permission from Wiley-VCH, Copyright 2015. (c) Cyclic voltammetry (CV) of tetragonal $MgMn_2O_4$ (pink) and cubic $MgMn_2O_4$ (purple) thin film. Reproduced from ref. 28 with permission from American Chemical Society, Copyright 2015. (d) Typical voltage-capacity curves of tetragonal $MgMn_2O_4$ for a magnesium-ion battery in 0.5 M $Mg(ClO_4)_2$ in EC:DEC. Reproduced from ref. 30 with permission from Royal Society of Chemistry, Copyright 2015.

insertion behavior was observed for tetragonal phase (Fig. 8c), indicating that the phase stabilization of spinel Mn_2O_4 is critical to acquire the reversible electrochemical activity. However, opposite results were obtained when the tetragonal $MgMn_2O_4$ nanoparticles were employed with 0.5 M $Mg(ClO_4)_2$ in EC:DEC as the electrolyte, which delivered a reversible capacity of 120 mA h/g (Fig. 8d).[30] Such inconsistent results may be due to the different current density and particle sizes in their experiments.[28, 30] Despite the low mobility of Mg^{2+} in spinel Mn_2O_4,[13, 28, 30] reducing current density and particle sizes can potentially enable higher Mg storage in spinel Mn_2O_4, and these experimental work seem to provide encouraging results to demonstrate that. Nevertheless, a more systematic experimental study is necessary to clear the confusion and confirm how phase transformation affects capacity of the spinel Mn_2O_4.

Given the low mobilities of Mg^{2+} in oxide spinel, sulfide spinels (thiospinel), expected to have higher Mg^{2+} mobility due to moderate increase of diffusion channel size and less ionic interaction between Mg^{2+} and the host structure, were also investigated.[7, 31, 32] Similar to oxide spinel, Mg^{2+} diffuse in the thiospinel along zigzag-shaped paths through a narrow, triangular aperture of three sulfur atoms (Fig. 5). Calculation of Mg^{2+} mobility in thiospinel with different transition metal (Ti, V, Cr, Mn, Fe, Co, Ni) shows several thiospinel compounds exhibit reasonable Mg^{2+} mobility including Mn_2S_4 (515 meV), Cr_2S_4 (567 meV), and Ti_2S_4 (615 meV) (Fig. 7b),[7] which are slightly more than or close to the 525 meV threshold. Comparison between DFT calculations and experimental results show that thiospinel TiS_2 have a ~200 meV reduction in migration barrier than spinel MnO_2, which means ~4 order of magnitude improvement in diffusion, though still higher than Mo_6S_8. Considering the thermodynamic stability, voltage, capacity, and migration activation energy, Cr_2S_4, Ti_2S_4, and Mn_2S_4 emerge as the top three cathode candidates amongst the 3d transition-metal thiospinel compounds.

To validate the theoretical prediction, thiospinel TiS_2 was synthesized and tested in an APC electrolyte at 60 °C, yielding an initial capacity of 200 mA h/g (corresponding to $Mg_{0.84}Ti_2S_4$) with an average potential of 1.2 V at C/20 (Fig. 9a).[24] In addition, it exhibits excellent rate capabilities and the small volume change during cycling promotes good capacity retention. Fourier mapping on electrochemical magnesiation of 0.8 Mg demonstrated that ~30% of Mg^{2+} occupied octahedral 16c sites and ~20% on tetrahedral 8a sites, corresponding to the composition of $Mg[oct]_{0.59}Mg[tet]_{0.189}Cu_{0.1}Ti_2S_4$. In addition, Mg^{2+} only occupied octahedral sites in partially discharged Ti_2S_4 (0.4 and 0.6 Mg/Ti_2S_4). Therefore, a stepwise Mg^{2+} intercalation

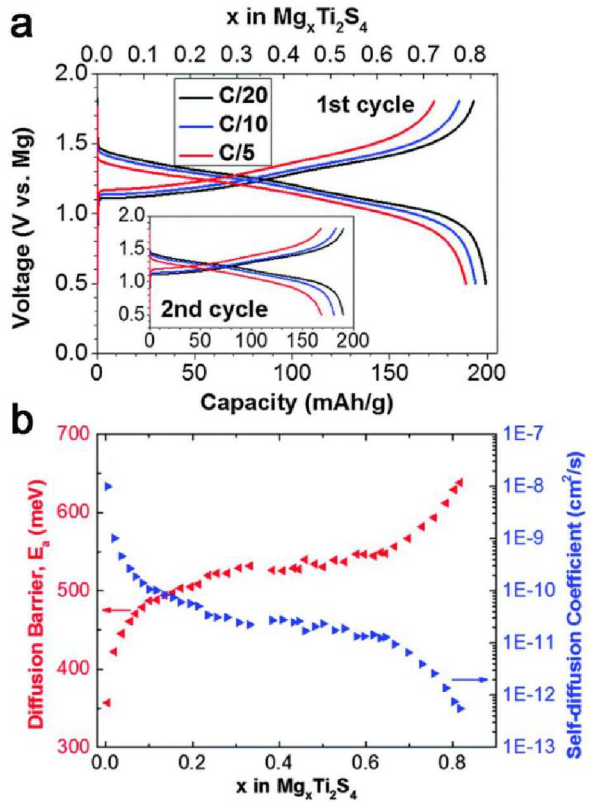

Fig. 9 Electrochemistry of C-Ti_2S_4 coin cells with an APC electrolyte and a Mg negative electrode at 60 °C. (a) Discharge and charge curves of the first and second (inset) cycles at various rates in APC/THF electrolyte. (b) Capacity and coulombic efficiency (CE) evolution at a C/10 rate in APC/G4 electrolyte (inset showing 99% CE). Reproduced from ref. 24 with permission from Royal Society of Chemistry, Copyright 2016.

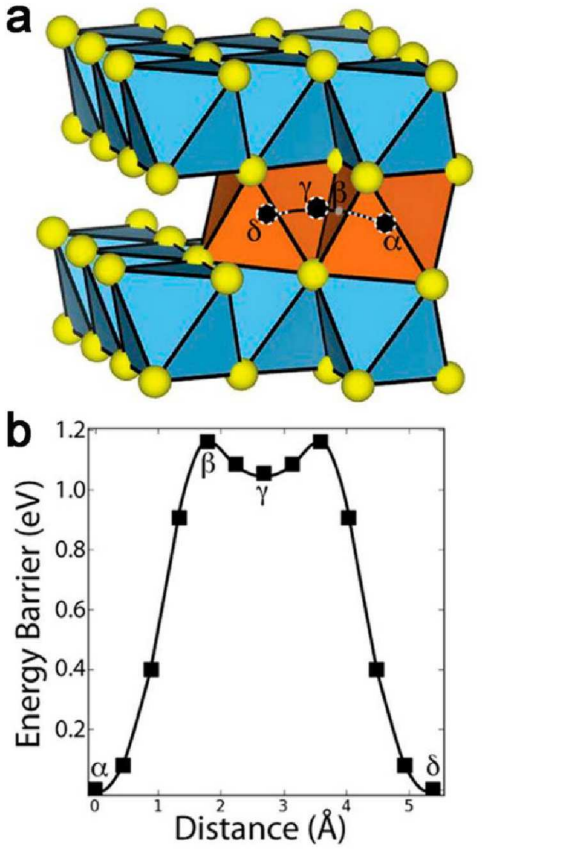

Fig. 10 (a) Crystal structure and pathway, and (b) migration barrier in layered TiS_2. Reproduced from ref. 33 with permission from American Chemical Society, Copyright 2015.

mechanism is proposed: octahedral 16c sites are filled first, followed by population of tetrahedral 8a sites, which is driven by subtle thermodynamic and kinetic factors. The experimental results partially confirm simulations, however, tri-vacancy hops mechanism employed in simulations should be improved because it shows some inconsistency with experimental results (Fig. 9b).

Compared with Chevrel phase (Mo_6S_8 or Mo_6Se_8), spinel compounds hold the promise to obtain high voltage and capacity, thus high energy density as cathodes for RMBs. However, Mg^{2+} can hardly intercalate spinel compounds reversibly at room temperature, which is the biggest obstacle of spinel. Several methods have been used to remit the problem, such as elevating the operating temperature, reducing the particle sizes, and increasing the volume of the spinel crystal structure.[33] In addition, Mg desolvation process followed by surface diffusion greatly affects intercalation overpotential. To our best knowledge, there is no study on the Mg desolvation process at the surface of spinel, which needs to be clarified in any future study concerning the kinetics of spinel. For oxide and sulfide spinel, the gravimetric capacities of sulfur spinel compounds are approximately 30% lower than their oxide counterparts due to the added mass of the S ion, in addition to the lower voltage. However, it is possible that sulfur-based compounds, with their improved intrinsic bulk cation mobility and less requirement (presumably) for electronically conductive coatings, could achieve a higher fraction of their theoretical energy density (~400 W h/kg), and thus higher practical energy densities.[7]

2.3 Layered sulfide/selenide

As a typical layered material, layered TiS_2 can serve as a model to investigate the thermodynamics and kinetics associated with Mg intercalation into layered structure. Layered TiS_2 consists of stacking sequences of the TiS_2 slabs, each of which is composed of a stacking of close-packed two-dimensional triangular lattices of sulfur. Ti atoms occupy octahedrally coordinated interstitial sites between sulfur planes (Fig. 10a).[22, 33] Mg^{2+} diffuse between stable octahedral sites through intermediate tetrahedral sites, where the energy exhibits a local minimum before moving to the adjacent octahedral sites. The migration barriers at the dilute Mg concentrations are calculated, and the maximum barrier (1160 meV) occur when Mg^{2+} passes through a triangle face created by three of the sulfur atoms of the MgS_6 octahedron (point β in Fig. 10a, b).[33] The shortest Mg-S distances along the migration path lie at the center of the triangular face separating the tetrahedral and octahedral sites, and the Ti-S bond length decides the size of diffusion channels.

The electrochemical performance of layered TiS_2 was measured in APC/THF at 60 °C.[22] An initial discharge capacity of

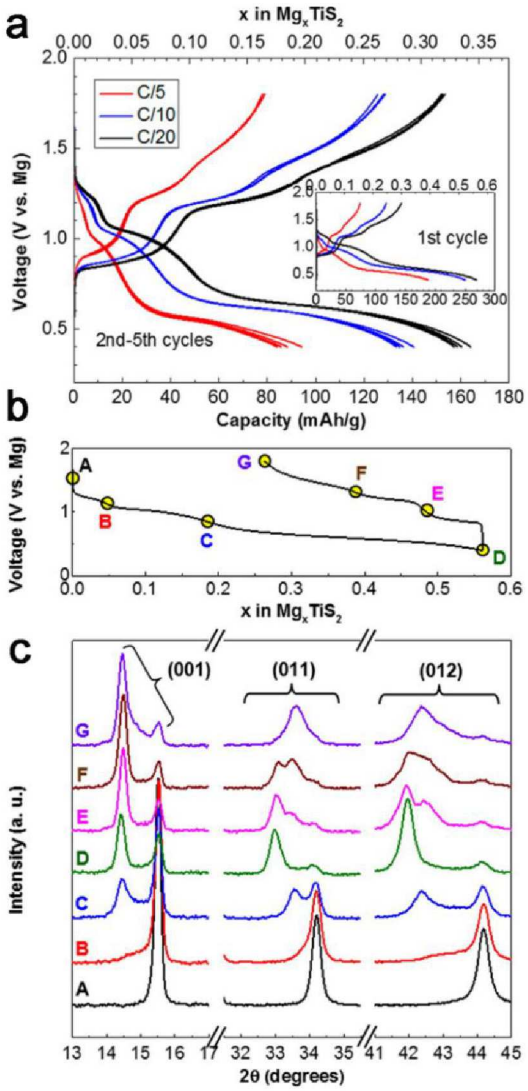

Fig. 11 (a) Discharge and charge profiles of layered TiS_2. (b) Electrochemical discharge-charge profile at C/20 on the first cycle. (c) XRD profiles. Reproduced from ref. 22 with permission from American Chemical Society, Copyright 2016.

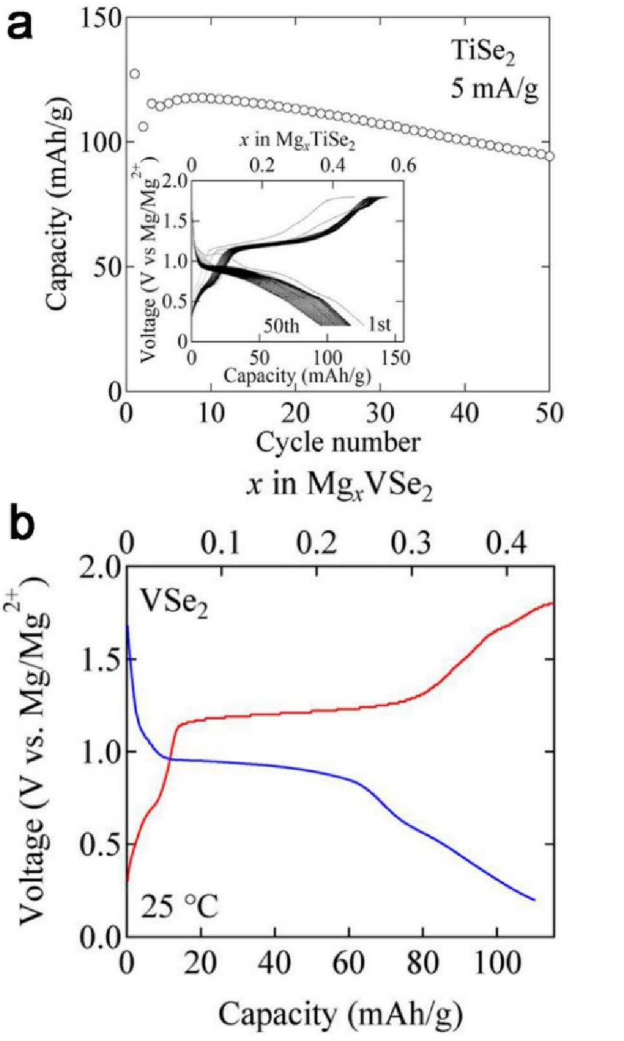

Fig. 12 (a) Cycle performance of RMBs with $TiSe_2$ for capacity measured at 25 °C. The inset shows the charge/discharge curves on each cycle. (b) The charge/discharge curve (on second cycle) with VSe_2 cathode measured at 25 °C. Reproduced from ref. 38 with permission from Springer Nature, Copyright 2015.

270 mA h/g (0.56 Mg/TiS_2) at a C/20 rate (inset in Fig. 11a) could be obtained. Three voltage plateaus are observed, and the corresponding phase transformation is confirmed by *in situ* XRD results (Fig. 11b, c). Both the experimental and calculation results demonstrate that Mg^{2+} can intercalate reversibly into layered TiS_2. However, the low mobility renders its performance at RT unsatisfactory. Other than raising temperature and reducing the particle size, substituting Se for S in layered TiS_2 could be an effective way to increase the mobility of Mg^{2+}.[34-37]

Despite no quantitative studies on how Se substitution affects the thermodynamics and kinetics of Mg^{2+} intercalation into layered TiS_2, qualitative analysis shows that the substitution will enlarge the channel for Mg^{2+} diffusion owing to longer Ti-Se bond, and reduce the interaction between Mg^{2+} and the host lattice, especially at the center of the triangle (point β in Fig. 10), where Mg^{2+} encounters the maximum energy batteries.[34] For this reason, layered $TiSe_2$ hold more possibility for practical use at RT, especially when considering its much higher volumetric capacity (~551 mA h/cm^3) than that of TiS_2 (~370 mA h/cm^3). $TiSe_2$ (~10 μm) was employed as cathode at 25 °C, which showed a specific capacity of ~108 mA h/g in the first 50 cycles (Fig. 12a).[38] In contrast, TiS_2 can only achieve the comparable capacity at 60 °C and with smaller particle sizes.[22]

Above we discussed how substituting S by Se affects the diffusion of Mg^{2+} in layered $TiSe_2$, which provides a reasonable explanation for the better kinetics of $TiSe_2$ than TiS_2. However, this may not be the only reason that accounts for the improvement in kinetics, as some research points out that the electronic structure also plays an important role.[39-43] In transition-metal chalcogenides, electronic delocalization happens in metal-ligand units through orbital mixing because of good energy and symmetry match, and the electronic wave

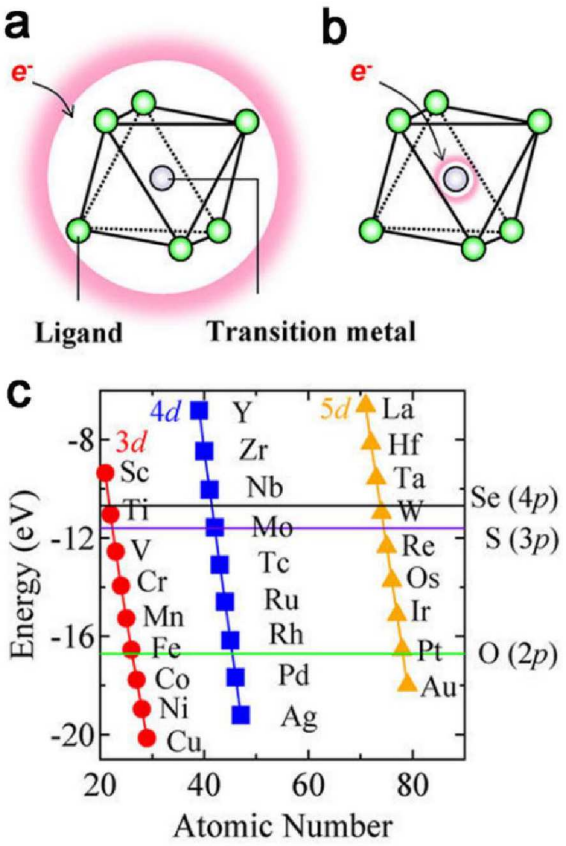

Fig. 13 (a) Charge distribution in the electronic state with (a) strong d-p mixing (b) weak d-p mixing. (c) Energy diagram of atomic orbitals. Reproduced from ref. 38 with permission from Springer Nature, Copyright 2015.

function of transition-metal chalcogenide spreads on both constituent atoms.[44] The charge density of the introduced electrons distributes over metal-ligand units (Fig. 13a). In a system with weak orbital mixing because of poor energy and/or spatial overlap of orbitals, the electrons will be accommodated only in the transition metal orbitals (Fig. 13b). In the case of selenides, d-p orbital mixing are enhanced by high orbitals overlap due to the large 4p-orbital size of Se, compared with oxides or sulfides. Since the energy levels of valence atomic orbitals in $TiSe_2$, 3d-orbital of Ti and 4p-orbital of Se, are close to each other, the mixed electronic structure is expected around Fermi energy (Fig. 13c), which enables a better accommodation of electrons accompanied with the intercalated Mg^{2+}, resulting in good electrochemical activity for Mg storage (Fig. 12a) even with micro-sized particles at RT.[38] Likewise, layered VSe_2 (Fig. 12b)[38] and WSe_2[45] show the good electrochemical activity for Mg^{2+} intercalation at ambient temperature.

In view of many misunderstanding on the term of orbital hybridization, it is necessary to elaborate it in this review. Orbital hybridization refers to mixing atomic orbitals into new hybrid orbitals within a single atomic site. The phenomenon that adjacent atomic orbitals with comparable energy from different atoms overlap and form a covalent bond or

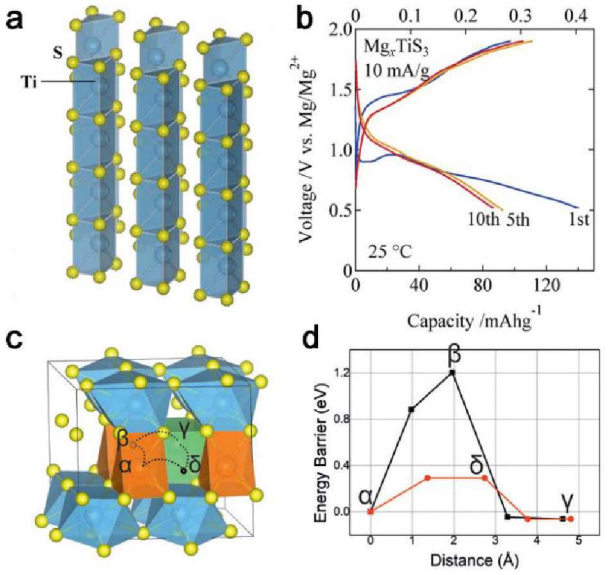

Fig. 14 (a) Crystal structure of TiS_3. (b) Charge/discharge curve (on the 1st, 5th, and 10th cycles) of the Mg battery cell with TiS_3 measured at 25 °C. Reproduced from ref. 46 with permission from The Japan Society of Applied Physics, Copyright 2015. (c) Migration pathway and (d) diffusion energy barrier of Mg in $Mg_{0.375}TiS_3$. Reproduced from ref. 49 with permission from American Chemical Society, Copyright 2017.

delocalized bond should be called as orbital mixing, not orbital hybridization. The orbital mixing is dictated by the energy match between neighbouring atoms orbitals and their symmetry. The more closely the energy of adjacent atomic orbitals from different atoms match and the better spatial overlap they have, the more covalent the interaction is and the electrons occupying the orbital are more delocalized between the two or more atoms.

The orbital mixing theory is further validated by reversible Mg storage in titanium trisulfide (TiS_3).[46] The crystal structure of TiS_3 consists of chains of trigonal prismatic [TiS_6] units sharing opposite faces along the b-axis (Fig. 14a).[46-48] Neighbouring chains are connected laterally into slabs parallel to the (001)-plane and separated by a van der Waals gap, which allows Mg^{2+} to insertion into the space between chains. As the energy level of the S 3p orbital (-11.60 eV) is close to that of the Ti 3d orbital (-11.04 eV), the electronic structure is spread over cluster-like [TiS_3] units by d-p orbital mixing. In the electronic structure, electrons introduced by Mg^{2+} insertion process will be accommodated into a d-p orbital mixed electronic state, in which electron density is delocalized over both Ti and S atoms. In addition, the local electrostatic interaction between Mg^{2+} and the host lattice could be suppressed through the delocalization of electron density. Thus, micro-sized TiS_3 shows the first discharge capacity of 140 mA h/g at 10 mA/g and RT (Fig. 14b), corresponding to Mg concentration of $Mg_{0.37}TiS_3$, which is further confirmed by a low migration barrier of 292-698 meV calculated along the [010] direction (Fig. 14c, d).[49] This value is much lower than that in spinel and layered TiS_2 (615-1160 meV), also the ~525 meV threshold.

Since d-p orbital mixing contributes to the good electrochemical performance of $TiSe_2$ and TiS_3, further study

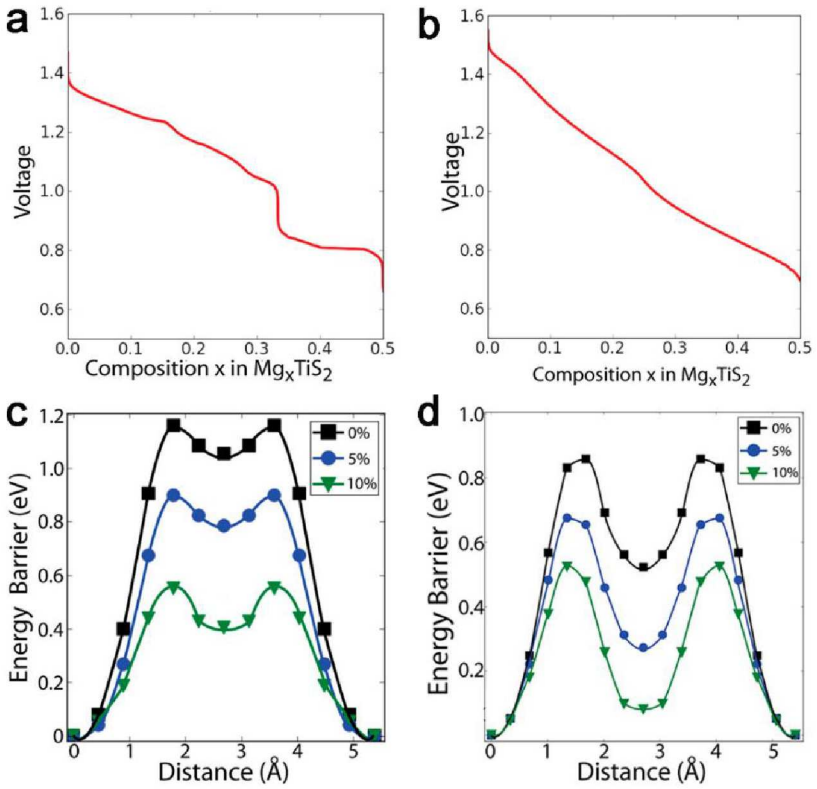

Fig. 15 Voltage curve for (a) spinel and (b) layered Mg_xTiS_2 calculated with Monte Carlo simulations at 300 K. Migration barriers in (c) spinel and (d) layered TiS_2 for different volume expansion. Reproduced from ref. 33 with permission from American Chemical Society, Copyright 2015.

based on the electronic structure could open a new way to design cathode materials for RMBs.

2.4 Layered vs. spinel: TiS_2

Based on calculation and experimental results,[7, 13, 22, 33] spinel and layered structures are compared systematically in this section using TiS_2 as an example. Mg^{2+} tend to occupy the octahedral sites in both layered and spinel TiS_2 with diffusion mediated by hops between octahedral sites that pass through adjacent tetrahedral sites (Fig. 5b and Fig. 10a). The calculated voltage profile for layered Mg_xTiS_2 shows three plateau (Fig. 15a), corresponding to three stable Mg-vacancy orderings: $Mg_{1/6}TiS_2$, $Mg_{1/3}TiS_2$, and $Mg_{1/2}TiS_2$, while the sloping regions at low and intermediate Mg concentration can be ascribed to solid solutions characterized by Mg-vacancy disorder.[33] In contrast, spinel Mg_xTiS_2 exhibits a sloping voltage profile (Fig. 15b) as x varies between 0 and 0.5 in Mg_xTiS_2, which represents more of a solid solution across the entire composition range. As we have discussed before, both spinel and layered TiS_2 hold high diffusion barriers for Mg^{2+}.[7, 33] To improve the mobility of Mg^{2+}, an effective method is to increase the size of diffusion pathway by increasing the c-lattice parameter or crystal volume. In layered $Mg_{1/32}TiS_2$, increasing the c-lattice parameter by 5% or 10% lowers mobility barriers to 900 and 550 meV (Fig. 15c), while in spinel $Mg_{1/32}TiS_2$, a 5% volume increase lowers mobility barrier to 680 meV (Fig. 15d). The results indicate that both layered and spinel TiS_2 are sensitive to the size of octahedral and tetrahedral sites and artificially increasing the distance between layers in layered TiS_2 and crystal volume of spinel TiS_2 benefits Mg^{2+} mobility.

The interaction between the intercalants (the cation) and the host (the intercalation compound) can be understood by evaluating the degree of remixing between the transition metals and anions of the host. Charge difference plots were compared for Mg insertion into tetrahedral sites of layered and spinel TiS_2 (Fig. 16),[33] in which the remixing in the spinel tetrahedral sites is more evenly distributed than that in the tetrahedral site of layered TiS_2. In spinel, each S anion coordinating a tetrahedral Mg site mixes with three Ti (Fig. 16b). In layered TiS_2, only one of the four S anions coordinating a tetrahedral Mg site mixes evenly with three Ti (the top sulfur atom in Fig. 16a), while the remaining three S mix primarily with only one Ti each and partially mix with two additional Ti that are "shared" by the other S anions. Such a higher coordination of the S sublattice with Ti is likely to distribute the remixing over more Ti-S bonds, accounting much for the lower migration barrier in spinel compared to that in layered TiS_2.[33]

The migration barriers for Mg hops in layered and spinel TiS_2 correlate with the difference in energy between octahedral and tetrahedral site occupancy. Several factors contribute to energy difference between tetrahedral and octahedral sites: the size of sites, the flexibility of coordinating ions, and the electrostatic energy. Also, more complex quantum mechanical effects exist, including the flexibility of adjacent ions to remix as the positively charged cation migrates from one site to another.

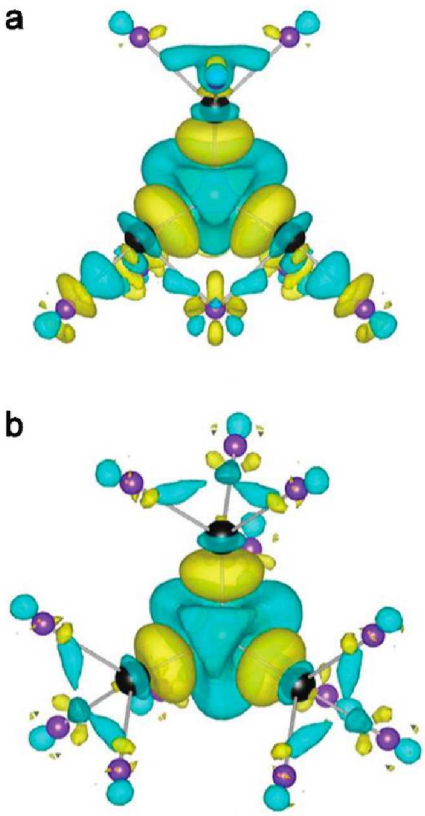

Fig. 16 Charge remixing upon insertion of a Mg in the tetrahedral site of (a) layered and (b) spinel TiS_2 with identical S-S bond lengths. Areas of charge accumulation are shown in yellow while depletion is shown in blue. Sulfur atoms are shown as large black spheres, Ti as small purple spheres, and Mg at the center as an orange sphere. Bonds are drawn in gray. Reproduced from ref. 33 with permission from American Chemical Society, Copyright 2015.

However, no unambiguous ways can disentangle the role of purely electrostatic interactions from the quantum mechanical interactions responsible for remixing.

The conclusion drawn in this charge remixing calculation is also in accordance with the aforementioned d-p mixing mechanism,[38, 46] in which high Mg migration mobility and low migration barrier are expected when the electronic structure of the transition metal (d orbital) overlaps more with the electronic structure of the anion (p orbital) so that charge can be better distributed over the Ti-S/Se bonds.

Summarizing the above discussions, several measures can be taken to improve the migration kinetics of Mg^{2+} in intercalation cathodes: 1) increasing temperature, which can improve the Mg^{2+} activity.[22, 23] 2) Downsizing the particles of cathodes, which will shorten the diffusion distance of Mg^{2+} in cathodes.[34] 3) Substituting O with S and Se. The substitution will reduce the ionicity of the hosts, and enlarge the channel for Mg^{2+} diffusion, both of which weaken the interaction between Mg^{2+} and the host lattice.[7, 35, 38] Besides, the substitution will decrease site energy difference along the diffusion pathway, contributing to Mg^{2+} hopping.[50] 4) Employing compounds with the similar d-p orbital energy, which can contribute to the accommodation of charge brought by Mg^{2+}, according to the d-p mixing mechanism discussed above.[33, 38, 46] 5) Using transition metal ions that readily shift by more than one valence state, such as Mo, as they are likely to be more flexible in remixing as Mg migrates through the crystal.

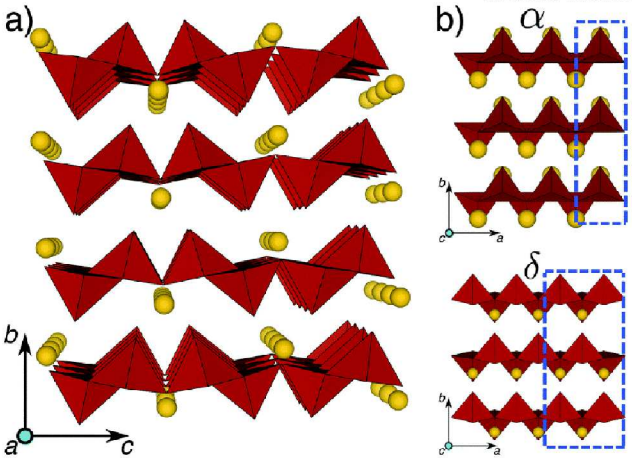

Fig. 17 (a) The V_2O_5 structure of both the α and δ polymorphs on the b-c plane with the yellow spheres indicating the intercalant sites while (b) shows the α and δ polymorphs on the a-b plane. Reproduced from ref. 65 with permission from Royal Society of Chemistry, Copyright 2015.

2.5 Layered oxides

In last section we discussed layered sulfides/selenides. Despite layered sulfides are a large group among inorganic compounds, TiS_2 stands out as a model system for our discussion because extensive experimental, theoretical and computational studies. In this section, our discussion proceeds to layered oxides, also a very rich family of inorganic materials. Unfortunately, we could not find a similar representative example to focus on, so we will expand the discussion on several typical oxides.

Similar to layered sulfide, the weak van der war force between layers renders layered oxide presumably good intercalation compounds, and their higher voltage vs. sulfide make them more attractive in terms of energy density.[51-53] Besides, the structural flexibility, which can accommodate the expected severe structural deformations upon insertion of Mg^{2+},[54-57] also makes layered transition metal oxides a kind of promising cathode candidate for RMBs.

2.5.1 V_2O_5

V_2O_5 received the most attention for Mg batteries among all layered oxides[57-65] Its lattice is comprised of layers of alternating edge- and corner- sharing VO_5 pyramids (Fig. 17), with the intercalant atoms (yellow spheres) located between the layers.[65] The main difference between α and δ polymorphs lies in the different stacking of layers along a direction (perpendicular to the b-c plane) (Fig. 17b). When intercalated into V_2O_5, Mg atoms occupy the center of four VO_6 octahedrons running along the a-direction of the orthorhombic lattice. The calculation shows that the migration barriers in the δ phase (~600-760 meV) are much lower than those in the α phase (~975-1120 meV), with the respective migration energies adopting "valley" and "plateau" shapes, which can be attributed to the changes in the coordination environment of Mg along the diffusion path (Fig. 18).[58, 61] In the α phase, Mg migrates between adjacent 8-fold coordinated sites through a shared 3-

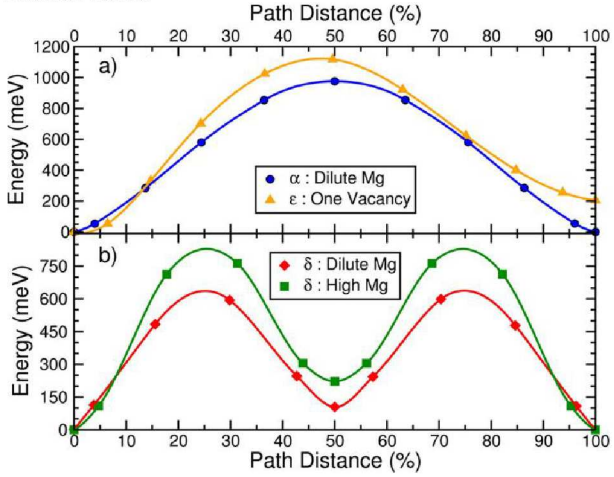

Fig. 18 Activation barriers for Mg diffusion in (a) α-V_2O_5 and (b) δ-V_2O_5. Reproduced from ref. 61 with permission from American Chemical Society, Copyright 2015.

fold coordinated site (activated state), a net 8 → 3 → 8 coordination change, while in the δ phase Mg migrates between adjacent 6-fold coordinated sites through two 3-fold coordinated sites separated by a metastable 5-fold coordinated "valley", a net 6 → 3 → 5 → 3 → 6 coordination change.[61] Hence, for Mg^{2+} that prefers a lower coordination number, a α to δ transition upon Mg^{2+} insertion in V_2O_5 is likely.

In order to systematically evaluate the difference of α- and δ-V_2O_5 in Mg^{2+} insertion/extraction, the interlayer spacing, average voltage, and thermodynamical stability of α- and δ-V_2O_5 are calculated.[65] The interlayer spacing in α- and δ-polymorphs are calculated for empty V_2O_5 and intercalated MgV_2O_5 (Fig. 19a). At the same intercalant composition, the δ structures consistently have larger layer spacing than α (~3–5% larger). The change in the layer spacing is much smaller in δ (less than 2%) than α (9-14%). The higher layer spacing, plus the smaller coordination changes, contribute to the lower migration barriers of the δ phase. The average voltage of δ-V_2O_5 (2.56 V) is higher than α-V_2O_5 (2.21 V) (Fig. 19b). In the de-intercalated limit, α-V_2O_5 is thermodynamically stable, while δ phase is metastable at RT. In the intercalated state, δ phase is more stable than α (by 75 meV per atom) (Fig. 19c), aligning well with the preferred coordination environment of Mg^{2+}, and accordingly the insertion voltage for δ is higher than α (Fig. 19b). Considering lower energy barriers, larger layer spacing, higher average voltage, and moderate thermodynamical stability, δ-V_2O_5 is a more promising cathode candidate for RMBs.

However, no experimental results have been reported for Mg^{2+} intercalated into δ-V_2O_5 up to now, which is likely related with the possibility of metastability in the de-intercalation limit at RT. On the other hand, reversible Mg intercalation/de-intercalation was observed in thin-film α-V_2O_5 with nanoscale thickness (~100 nm).[57] A capacity of 150 mA h/g, corresponding to $Mg_{0.5}V_2O_5$, was achieved with the voltage of ~2.35 V at 5 μA/cm² (Fig. 20), in agreement with the calculation results which predicted a voltage drop at x_{Mg}~0.5 due to the formation of a stable Mg vacancy ordering.[61]

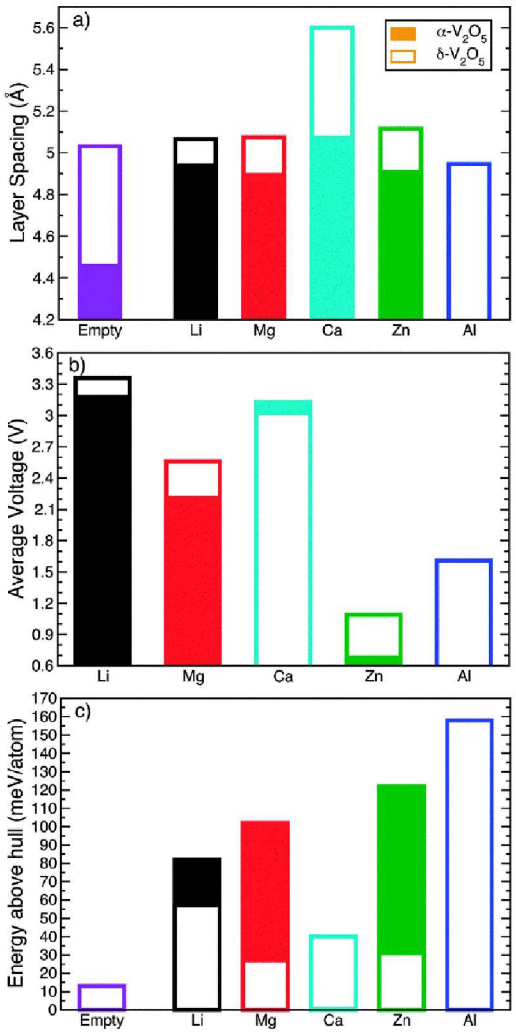

Fig. 19 (a) Plots the layer spacing values for the empty and intercalated versions of AV_2O_5 (A = Li, Mg, Ca, Zn and Al) for both α and δ polymorphs. (b) Displays the calculated average voltage values for the intercalation of the different ions and (c) shows the energy above hull, which quantifies the stability of a structure, for the empty and intercalated versions of α and δ. Reproduced from ref. 65 with permission from Royal Society of Chemistry, Copyright 2015.

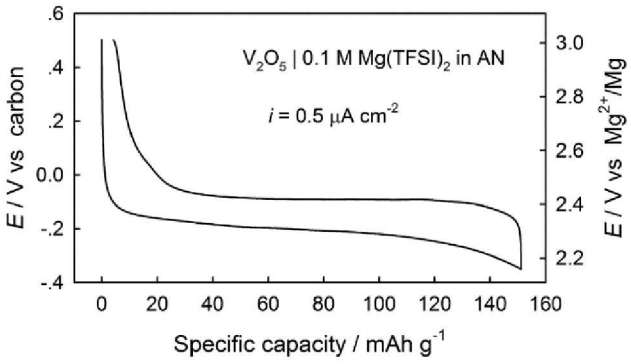

Fig. 20 Typical galvanostatic titration curve of a V_2O_5 thin-film electrode in 0.1 M $MgTFSI_2$ in AN (current density = 0.5 μA/cm). Reproduced from ref. 57 with permission from American Chemical Society, Copyright 2013.

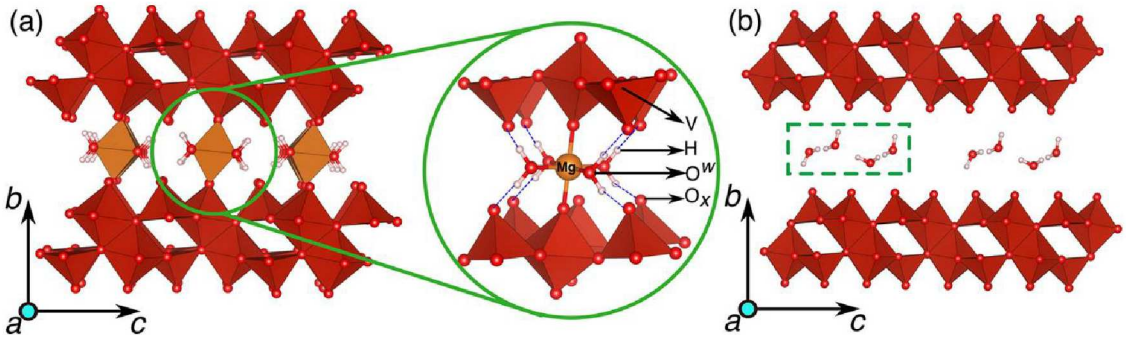

Fig. 21 The structures of the fully magnesiated (x_{Mg}= 0.5) and the fully demagnesiated xerogel structures, with **1**H_2O per formula unit of V_2O_5 are displayed in (a and b), respectively. Reproduced from ref. 66 with permission from American Chemical Society, Copyright 2016.

In another work, "solvent" molecules are incorporated in the cathode structure, which can presumably "shield" the charge on the Mg^{2+} electrostatically and attenuate the structural distortions.[66, 67] Xerogel V_2O_5 ($V_2O_5{\cdot}nH_2O$) comprises a "bilayer" arrangement of V_2O_5 layers (Fig. 21),[66, 68] in contrast with the monolayer in α- and δ-V_2O_5.[69, 70] A single bilayer of V_2O_5 is made up of two individual V_2O_5 monolayers (red polyhedra in Fig. 21), and intercalated guest species and H_2O molecules are present in the space between two bilayers. Such a bilayered framework host, with the interbilayer spacing of ~13.5 Å,[71] can provide the structure flexibility to adapt to the geometry of the intercalant ions by adjusting the interlayer separation. While each mole of H_2O added (removed) to (from) the structure results in an increase (decrease) of the interbilayer spacing by ~2.8 Å, the intercalated Mg^{2+} will lead to a decrease in the spacing.

The cycling of Xerogel-V_2O_5 in $Mg(TFSI)_2$/diglyme electrolyte achieved a discharge capacity of ~50 mA h/g (0.25 $Mg/V_2O_5{\cdot}nH_2O$) at 20 μA/cm² (Fig. 22).[67] A plausible mechanism of the intercalation process was proposed: during discharge, a solvation shell (diglyme) coordinated Mg^{2+} enters the $V_2O_5{\cdot}nH_2O$ bilayer and largely sheds the lattice water, resulting in the compression of interlayer distance ascribed from the attraction between V_2O_5 layers and Mg complex. Upon galvanostatic charge, Mg coordinated clusters are pulled out of the lattice, which is accompanied by free diglyme molecules and/or a reservoir of composed diglyme filling the lattice to compensate the void, resulting in the largest interlayer distance. This mechanism appears to be reversible at the expense of further electrolyte decomposition, likely accounting for a slightly gradual capacity escalation, and Mg metal passivation via decomposed electrolyte species and the removal of lattice water. However, the intercalation mechanism needed to be further confirmed in view of large overpotential. The function of crystal water, whether just keeping the crystal structure or doing good to the kinetics of Mg^{2+} diffusion, is still unknown.

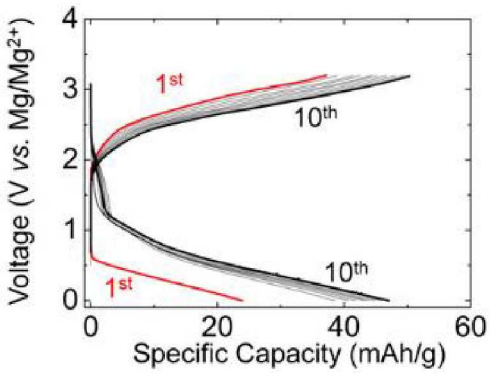

Fig. 22 (a) Galvanostatic charge-discharge curves of $V_2O_5{\cdot}nH_2O$ in 1.0 M $Mg(TFSI)_2$/diglyme electrolyte at 20 μA/cm². Reproduced from ref. 67 with permission from American Chemical Society, Copyright 2016.

2.5.2 α-MoO_3

Sharing the similar layered structure with V_2O_5, orthorhombic α-MoO_3 is known as an intercalation host for monovalent and divalent cations.[72-76] It is built up by double layers of edge- and corner- sharing [MoO_6] octahedra, which is held together by weak van der Waals attraction forces, with the interlayer distance of ~6.929 Å (Fig. 23a).[54, 57, 72] When intercalated into α-MoO_3, Mg^{2+} will occupy the sites within and between α-MoO_3 layers, running along the c-axis.[77] The migration barriers were calculated to be 880 meV, corresponding to the diffusion constant of 10^{-17} cm²/S, much higher than ~525 meV threshold, indicating the sluggish diffusion kinetics.[57, 77-79] A thin α-MoO_3 film (~100 nm) electrode was prepared to reduce the diffusion path for the intercalating ion, mitigating somewhat the sluggish kinetics.[57] α-MoO_3 film delivered a magnesiation capacity of ~220 mA h/g, corresponding to 0.59 Mg^{2+}/MoO_3, with voltage of 1.7-2.8 V at 0.3 μA/cm² (Fig. 23b). The voltage difference (0.2-0.4 V) between the magnesiation and de-magnesiation process of α-MoO_3 (Fig. 23b), 3-6 times larger than that for V_2O_5 film,[57] indicates greater kinetic limitations. The large overpotential and

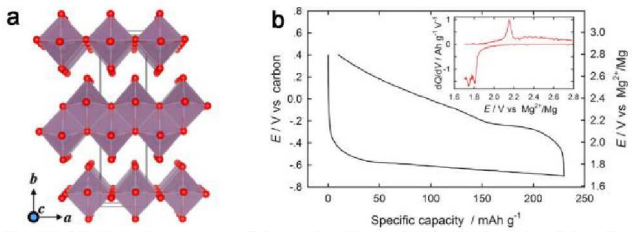

Fig. 23 (a) Crystal structure of layered α-MoO_3 (with Mo ions in violet six-coordinated by oxygens in red); layers stack along the b axis. Reproduced with permission.[5] Copyright 2017, American Chemical Society. (b) Galvanostatic titration curve of α-MoO_3 thin-film electrode in 0.1 M $Mg(TFSI)_2$/AN solutions (current density = 0.3 μA cm^{-2}). Corresponding dQ/dV plot is provided in the inset. Reproduced from ref. 57 with permission from American Chemical Society, Copyright 2013.

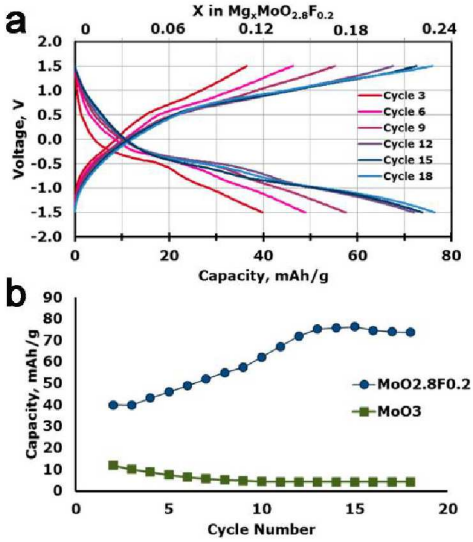

Fig. 24 (a) Voltage Profile for $MoO_{2.8}F_{0.2}$ over the first 18 cycles and (b) capacity versus cycle number. Electrolyte is 0.2 M $Mg(TFSI)_2$ in PC. Reproduced from ref. 84 with permission from American Chemical Society, Copyright 2016.

some degree of irreversibility may be due to the voltage-induced structural damage,[80] lower electronic conductivity of demagnesiated MoO_3,[81, 82] and some possible conversion reactions at the surface of α-MoO_3.[83] Therefore, modifications are needed to make α-MoO_3 a promising cathode candidate for RMBs.

2.5.3 $MoO_{2.8}F_{0.2}$

To enhance the kinetics of Mg intercalation, $MoO_{2.8}F_{0.2}$ with the α-MoO_3 structure was prepared by a mild fluorination.[84] The introduction of fluorine liberates an electron that is delocalized over the entire Mo-O layer in the ac plane, which will increase the electronic conductivity of $MoO_{2.8}F_{0.2}$.[85-87] Delocalization, introduced by fluorine atoms, will contribute to the accommodation of charge introduced by Mg^{2+} intercalation, and reduce the diffusion barrier of Mg^{2+}.[77] Like in α-MoO_3, when intercalated into $MoO_{2.8}F_{0.2}$, Mg^{2+} occupy the sites within and between $MoO_{2.8}F_{0.2}$ layers, and run along the c-axis. Whereas, the migration barriers are lowered to ~490 meV, smaller than the 525 meV threshold.[77] Micrometer-sized $MoO_{2.8}F_{0.2}$ delivered a first-discharge capacity of~40 mA h/g at 5μA, which increased to ~70 mA h/g (0.25 $Mg^{2+}/MoO_{2.8}F_{0.2}$) in 18th cycle, better than the micron-sized α-MoO_3 (Fig. 24),[84] indicating halogen substitution may be a viable strategy for improving the kinetics of layered oxides.[88]

2.5.4 $Mo_{2.5+y}VO_{9+\delta}$

Slow Mg diffusion in layered oxide-based cathodes (V_2O_5 and α-MoO_3) can be managed by the orthorhombic Mo-V oxides with open-tunnel structure.[89] The structure of Mo-V oxides contain layers, each of which is stacked by corner-sharing to form a microporous framework with three-, six-, and seven-membered ring tunnels (Fig. 25a, b).[89-92] The diameters of the six- and seven-membered ring channels are approximately 3 and 5 Å, respectively,[90] which can provide facile diffusion of Mg^{2+}. In Mo-V oxides, molybdenum or vanadium ions, which can change by two or more oxidation states, will facilitate achieving local electroneutrality and lower barriers to Mg^{2+} diffusion.[33, 37]

$Mo_{2.5+y}VO_{9+\delta}$ (~200 nm in diameter) achieved a capacity of 397 mA h/g (1st discharge) at C/70 and RT, corresponding to 3.49 Mg^{2+} per formula unit (Fig. 25c). The attainable capacity dropped to ~114 mA h/g and 90 mA h/g at rates of C/40 and C/12, respectively. An intercalation reaction mechanism is confirmed by the continuous XRD peak shifts with increasing Mg concentration.[89] Hence, combining mixed transition metal ions in oxides with an open-tunnel structure might contributes to the Mg^{2+} intercalation. Though with low Mg mobility in the material, in view of its high capacity and cycle stability, $Mo_{2.5+y}VO_{9+\delta}$ might warrant further theoretical and experimental investigation.

2.6 Polyanion

Above we discussed oxides, sulfides, and selenides with 3D and 2D diffusion pathways as cathodes for RMBs. In this part, we will further discuss polyanion compounds with 1D diffusion channel. Given great success in LIBs,[93-96] polyanion compounds (mainly olivine), could be promising cathodes for RMBs.

The olivine structure consists of a distorted hexagonal-close packed (hcp) framework of oxygen with tetrahedral sites occupied by P or Si and two distinct octahedral sites: 4a occupied by Mg or Li and 4c occupied by M ions (M = Fe, Mn, Co) (Fig. 26a).[97] 4a sites form linear chains of edge sharing

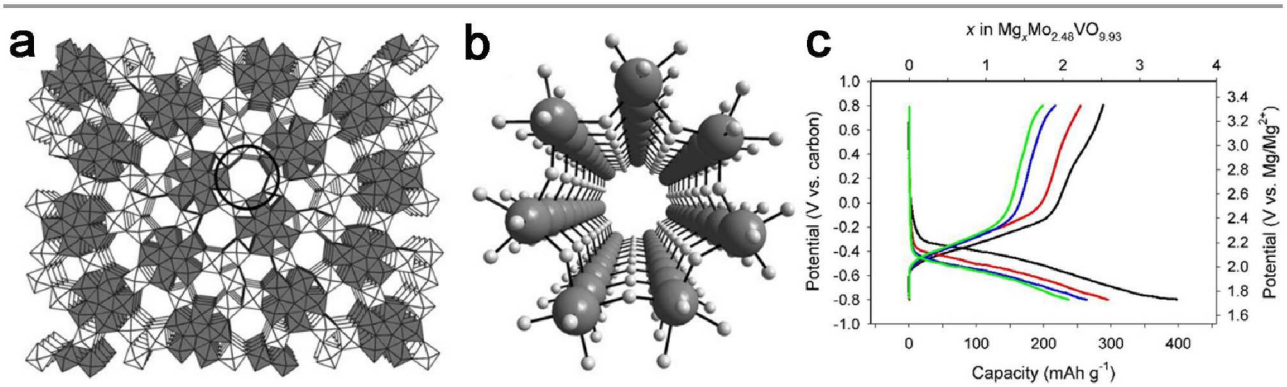

Fig. 25 Polyhedral representation of orthorhombic Mo-V oxide. The circle in (a) indicates a seven-membered ring. (b) Balland-stick representation of the channel structure. Reproduced from ref. 91 with permission from Royal Society of Chemistry, Copyright 2011. (c) Electrochemical discharge–charge profiles of an AC/$Mo_{2.48}VO_{9.93}$ cell at C/70 (1C = 140 mA/g): 1st cycle, black; 2nd cycle, red; 5th cycle, blue; 10th cycle, green. Reproduced from ref. 89 with permission from American Chemical Society, Copyright 2016.

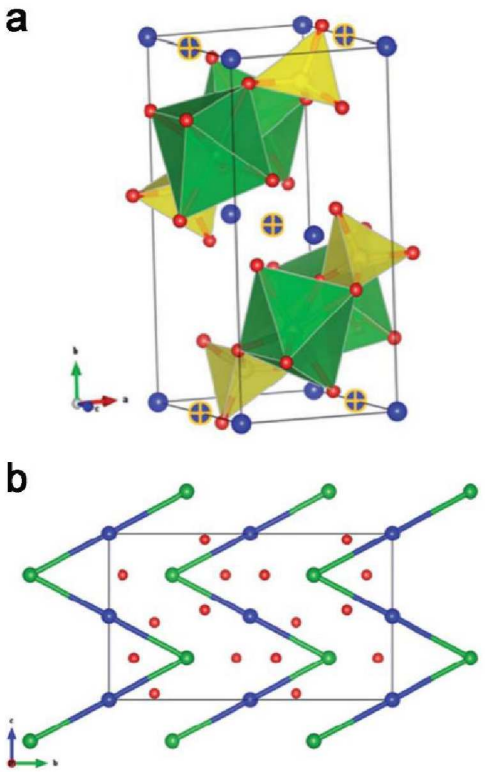

Fig.26 (a) Crystal structure of olivine compounds. Red: oxygen; yellow: Si or P; green: transition metal (M) at 4c sites; and blue: Mg or Li at 4a sites. (b) 2D view of olivine structures along the (100) plane. Si/P atoms are neglected for simplicity. Reproduced from ref. 97 with permission from Royal Society of Chemistry, Copyright 2012.

octahedral that favors the diffusion of ions along the 1D channel while maintaining the topology of olivine during cycling.[98, 99] Each 4a site connects two nearest neighbored 4c sites forming a zigzag 1D chain (Fig. 26b).

2.6.1 Phosphates

Mg^{2+} diffuse in olivine $FePO_4$ along the "wave-like" path from the octahedral (O) sites to the tetrahedral (T) sites (Fig. 27a).[100] The migration barrier of Mg^{2+} in $FePO_4$ is 580 meV, corresponding to a diffusivity of 10^{-13} cm^2/s, while the migration barrier in the magnesiated $FePO_4$ ($Mg_{0.5}FePO_4$) is 1025 meV, much higher than the ~525 meV threshold, corresponding to diffusivity constant of ~10^{-20} cm^2/s, indicating that removal of Mg^{2+} from $Mg_{0.5}FePO_4$ is not possible (Fig. 27a). Olivine $FePO_4$ only delivered a capacity of ~12 mA h/g at 20 μA/cm^2 (Fig. 27b), 6% of its theoretical capacity, which is attributed to surface amorphorization that prohibits the electrochemical reaction from penetrating deeply into the bulk.[100] The amorphorization is explained by the thermodynamically metastable intercalated product (Fig. 27c), which is demonstrated by calculations and failure to synthesize $Mg_{0.5}FePO_4$ via the solid state route.

2.6.2 Silicates

Similarly, Mg^{2+} diffuse in silicate along the 1D channel from octahedral sites to tetrahedral sites (Fig. 26).[97] The migration barriers in $MgMSiO_4$ (M=Fe, Mn, Co) were calculated to be 740-770 meV (Fig. 28a),[101] which is higher than the ~525 meV threshold, corresponding to diffusivity constant of ~10^{-16} cm^2/s, too high for Mg^{2+} to diffuse in silicates.

The majority of reports about silicates are presented by the same research group,[102-109] showing high capacity and stable

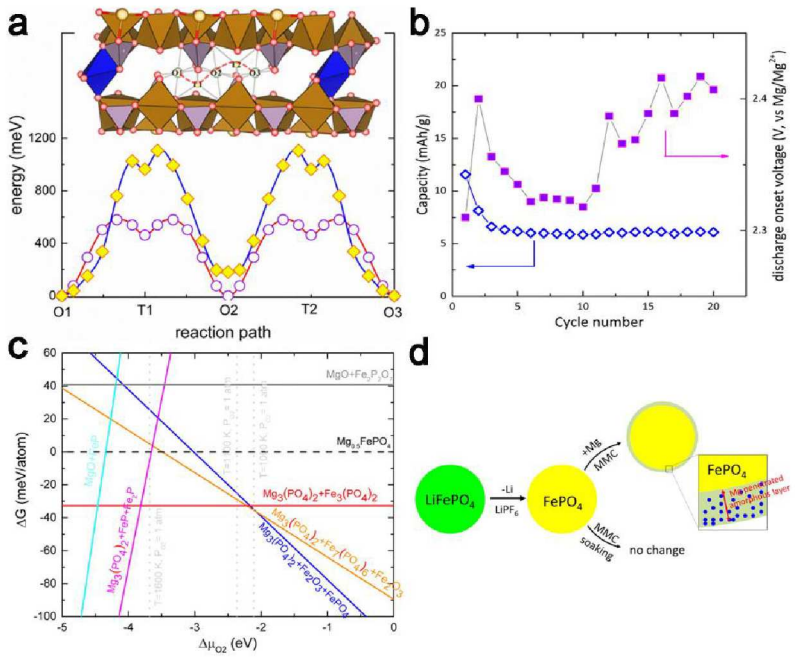

Fig. 27 (a) Energy profile for Mg^{2+} to diffuse in olivine $FePO_4$ (open circle) and $Mg_{0.5}FePO_4$ (solid diamond) lattice. (b) Cycled discharge capacity and onset voltage of olivine $FePO_4$. (c) Free energy to decompose olivine $Mg_{0.5}FePO_4$. (d) Schematic evolution of $FePO_4$ after different operations. Reproduced from ref. 100 with permission from American Chemical Society, Copyright 2016.

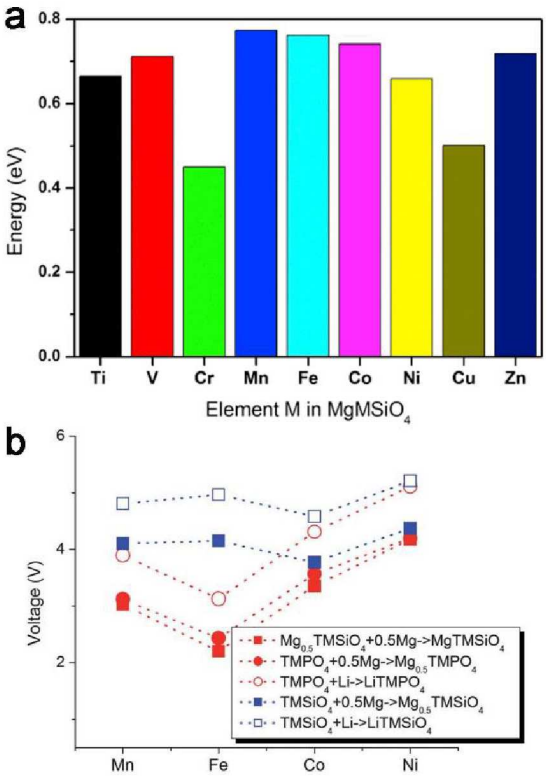

Fig. 28 (a) Migration barriers for Mg^{2+} diffusion in olivine silicate. Reproduced with permission.[101] Copyright 2016, Elsevier. (b) The voltage calculated for the lithiation and magnesiation of olivine compounds. Reproduced from ref. 97 with permission from Royal Society of Chemistry, Copyright 2012.

cycling performance. However, the reported average voltages are significantly lower than calculated results (Fig. 28b).[97] A more recent study re-examined silicates under the same conditions, but little capacity was achieved.[101]

The metastable orthorhombic $MgFeSiO_4$, with tetrahedrally coordinated Mg (Fig. 29a), delivered a reversible capacity of ~330 mA h/g at ~2.5 V at 6.62 mA/g and 55 °C (Fig. 29c).[110] The improved kinetics could be due to the tetrahedrally coordinated Mg, less favorable in energy than octahedrally coordinated Mg, which favors the Mg^{2+} diffusion.

In summary, reversible magnesiation of phosphate is prohibited by the surface amorphorization, which blocks the electrochemical reaction from penetrating deeply into the bulk phase. Limited by high migration barriers, diffusion of Mg^{2+} in normal silicates is not possible, unless at elevated temperature. Utilizing the less stable, tetrahedrally coordinated Mg site in silicates can achieve superior Mg diffusivity and improved kinetics for Mg insertion/extraction. Despite some inconsistency in the full-cell studies, probably due to the electrochemical setup and electrolytes, it is worthwhile to further investigate Mg^{2+} intercalation into olivine silicate given the promise of the excellent energy density and safety.

2.7 Open Framework

The open framework structure is a system containing voids whose sizes may range from a few angstroms up to hundreds of angstroms.[111-115] The large channels and interstices, beneficial for ion intercalation, fundamentally distinguish the open framework structure from other intercalation compounds.[116] A typical example is the Prussian blue analogues (PBAs). PBAs

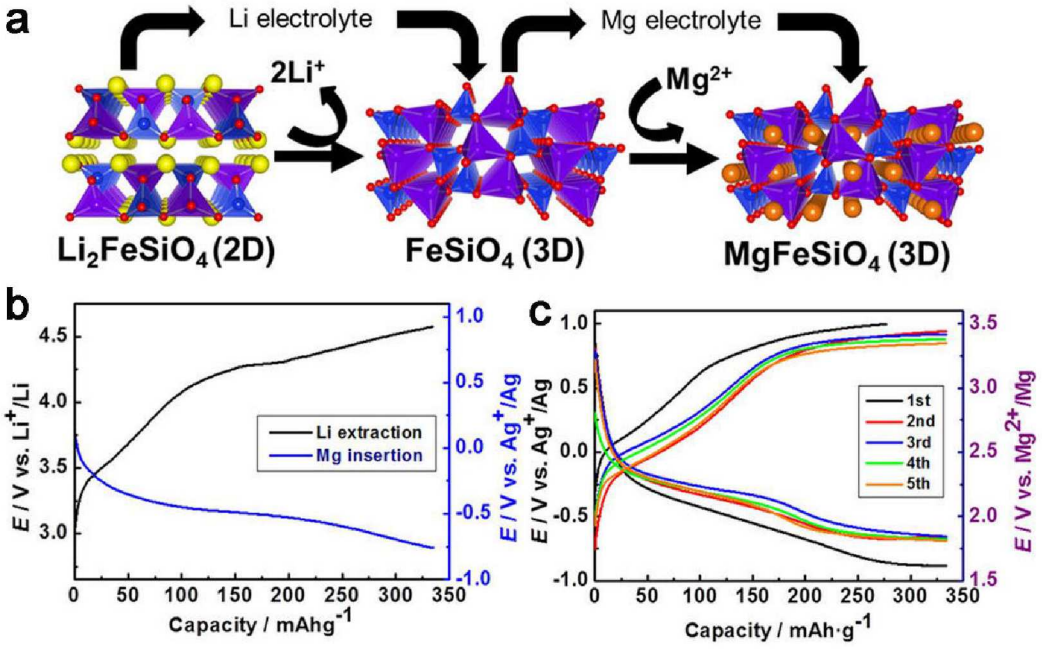

Fig. 29 (a) Schematic illustration of the ion-exchange methodology for the electrochemical synthesis of metastable orthorhombic $MgFeSiO_4$ from Li_2FeSiO_4. (b) Charge–discharge profiles for ion exchange process from Li_2FeSiO_4 to $MgFeSiO_4$. (c) Charge-discharge profiles of ion-exchanged $MgFeSiO_4$. All the Measurements were conducted at 55 °C. Reproduced from ref. 110 with permission from Springer Nature, Copyright 2014.

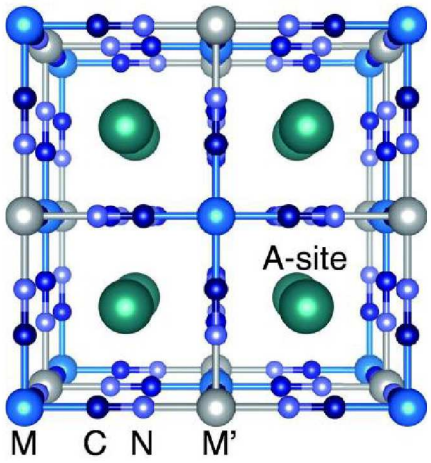

Fig. 30 Structure of a PBA $A_xM_y[M'(CN)_6]\cdot nH_2O$. Cations A and water are accommodated in A-sites. M and M' are transition metal ions. Reproduced from ref. 118 with permission from The Electrochemical Society, Copyright 2015.

have a typical formula of $A_xM_y[M'(CN)_6]$, in which M and M' refer to transition metal and CN refers to the ligand which connects all transition metals and therefore forms an open framework (Fig. 30).[116-119] The triple-bonded CN ligands increase the separation between M and M' ions, and open up the structure for ion and small molecule insertion. Intercalated ions are likely to be at least partially hydrated,[120, 121] and larger hydrated ions occupy the interstitial A sites (4.6 Å in diameter) and diffuse along the open <100> channels (3.2 Å in diameter).[122] Materials in the PBA family have been explored for monovalent, divalent, and trivalent ion insertion reversibly.[120, 123-127] However, the impact of various transition metals in the PBAs on the thermodynamics (theoretical capacity and voltage) and kinetics (diffusivity) of the intercalation process still lacks studying.

Reversible Mg^{2+} intercalation was demonstrated with nickel hexacyanoferrate (NFCN), showing an initial capacity of ~40 mA h/g in $Mg(TFSI)_2$/PC electrolyte, and increasing to 80 mA h/g in the 50th cycle (Fig. 31a), with a relatively high potential of ~2.9 V vs Mg/Mg^{2+} and low overpotential (Fig. 31b).[128]

Apart from the study in the organic electrolyte, PBAs, including nickel hexacyanoferrate,[129] manganese

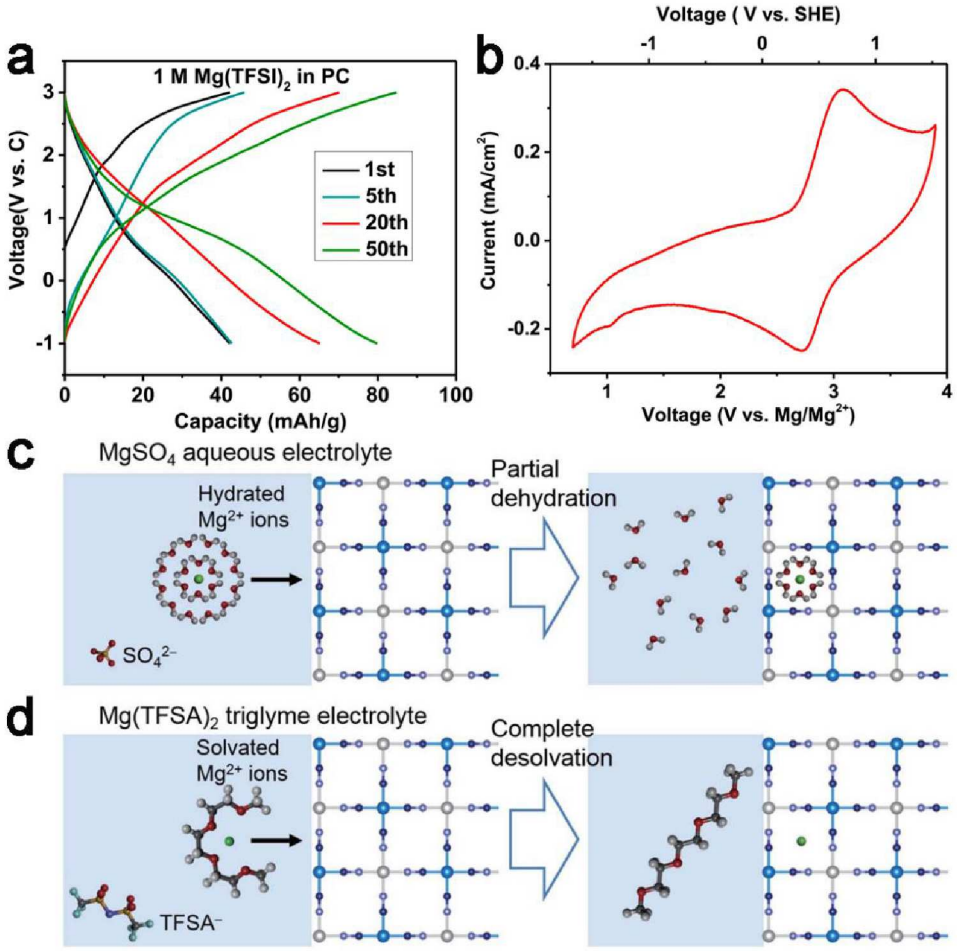

Fig. 31 (a) Galvanostatic cycling, and (b) Cyclic voltammograms of nickel hexacyanoferrate at a rate of 10 mA g^{-1} with 1 M $Mg(TFSI)_2$ in PC as the electrolyte. Reproduced from ref. 128 with permission from Elsevier, Copyright 2016. Schematic illustration of the insertion of Mg^{2+} ions into CuFe-PBA in (c) $MgSO_4$ aqueous electrolyte and (d) $Mg(TFSA)_2$ triglyme electrolyte. Reproduced from ref. 118 with permission from The Electrochemical Society, Copyright 2015.

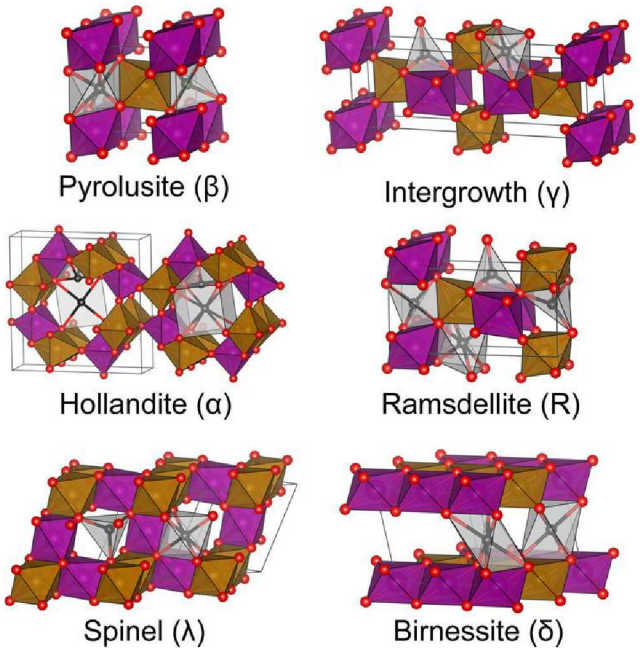

Fig. 32 Common polymorphs of MnO_2 and predicted sites for Mg intercalation. The purple and yellow spheres and surrounding octahedra denote spin-up and spin-down Mn atoms and MnO_6 octahedra, while the black spheres and surrounding gray polyhedra denote potential intercalation sites for Mg ions in the structure. Reproduced from ref. 135 with permission from American Chemical Society, Copyright 2017.

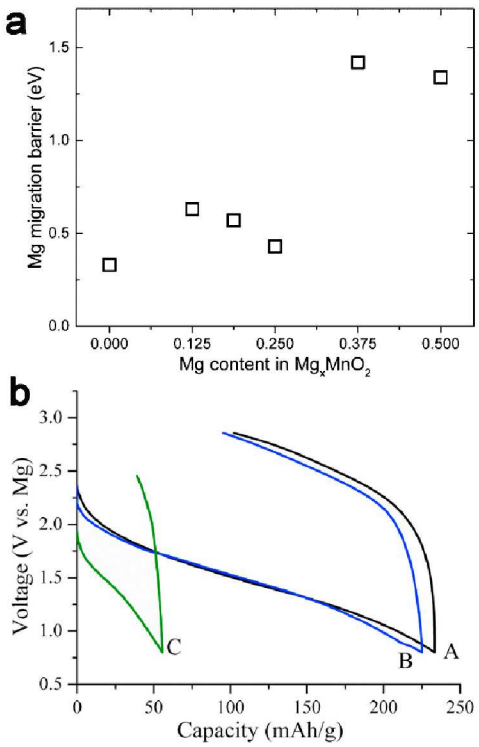

Fig. 33 (a) Mg hopping barrier in the ground states of α-Mg_xMnO_2. Reproduced from ref. 141 with permission from American Chemical Society, Copyright 2015. (b) Initial discharge–charge profiles of α-MnO_2 nanorods (A, B, and C) with different surface areas (231, 149, and 30 m^2/g, respectively). The cells were operated at a current density of 0.02 mA/cm^2 under room temperature. Reproduced from ref. 143 with permission from Elsevier, Copyright 2015.

hexacyanomanganate,[116] copper hexacyanoferrate,[116, 123] and $K_{0.1}Cu[Fe(CN)_6]_{0.7}\cdot 3.6H_2O$,[130] are also reported to intercalate Mg^{2+} reversibly in aqueous electrolyte (details in the following section). In order to investigate the different mechanisms of Mg^{2+} intercalation in PBAs in aqueous and nonaqueous electrolyte, PBA composed of Cu and Fe ions was studied using both aqueous and organic electrolytes.[118] The redox potential of CuFe-PBA was approximately 3 V vs. Mg/Mg^{2+} in electrolytes with Fe^{III}/Fe^{II} as the main redox active species. It delivered negligible capacities in organic electrolyte, while a capacity of 40-60 mA h/g at 1 C rate could be achieved in an aqueous electrolyte, suggesting the incomplete desolvation in the aqueous electrolyte could alleviate the electrostatic interaction of Mg^{2+} with the framework constituents, resulting in fast diffusion of Mg^{2+} ions (Fig. 31c, d).[118]

Reversible Mg^{2+} intercalation into PBAs is demonstrated both in organic and aqueous electrolytes, indicating that open framework structures with large voids can tolerate the diffusion of highly polarizing Mg^{2+} and co-intercalation of water molecules. However, limited energy densities yielded by most PBAs frameworks hinders their practical application in RMBs.

3. Conversion cathode

Other than intercalation compounds, materials undergoing conversion reaction, which can achieve higher energy density in theory, are also investigated. In contrast to intercalation cathodes, magnesiation and de-magnesiation of conversion materials break chemical bonds and create new ones during insertion and extraction of Mg.[131-133] According to equation (1), cathode particles typically convert into nanocomposite particles

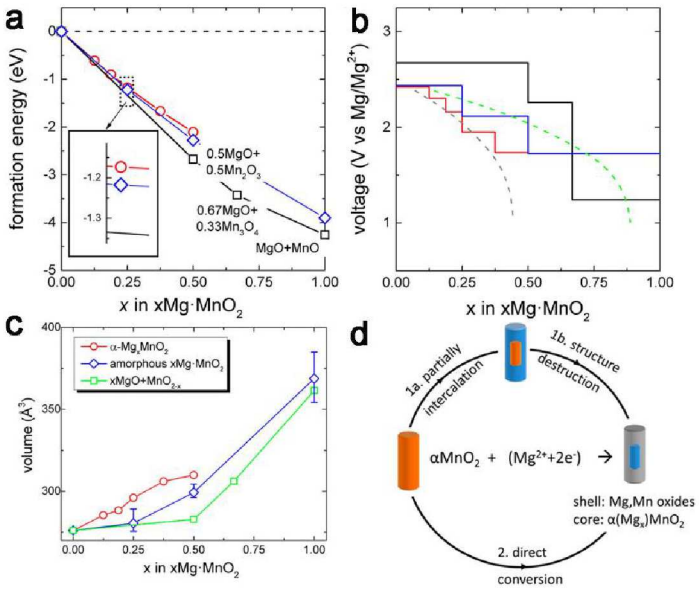

Fig. 34 (a) Reaction energy with the formation of intercalated compound (red), amorphous magnesium and manganese oxides (blue), and crystalline magnesium oxide and manganese oxides (black). (b) Voltage profile for the reaction between Mg and α-MnO_2 to form intercalated compound (red), amorphous magnesium and manganese oxides (blue), and crystalline magnesium oxide and manganese oxides (black). The dashed line shows the average experimental voltage profile, assuming that all (gray) or half (green) of α-MnO_2 participates in the first cycling. (c) Volumetric evolution of magnesiated α-MnO_2 following different reaction paths. (d) Possible reaction routes for the magnesiation of α-MnO_2. Reproduced from ref. **141** with permission from American Chemical Society, Copyright 2015.

comprising metal M nanoparticles dispersed in a $Mg_{z/2y}X$ matrix during magnesiation. The morphology and spatial correlation of the new phases may be controlled by diffusion coefficients of cations and anions, by electronic and ionic conductivity of new phases as well as by interfacial energies. Conversion reaction usually occurs during ion insertion when the electrode materials do not have open ion diffusion channels, or the number of inserted ions exceeds the maximum available sites. Materials of this type include many transition metal oxides, sulfides, chloride and etc. Some manganese oxide, e.g. α-MnO_2 and ramsdellinte-MnO_2, despite of their open channels for ion transport, are shown to undergo conversion reaction due to the strong distortion that damages the structure integrity.[134]

+ +— □ +

3.1 MnO_2

Transition metal oxides are the most studied conversion material for Mg batteries due to the richness of compositions and crystal structures, especially manganese oxide. Mn atom usually coordinates with six O atoms, forming a MnO_6 octahedra. Such octahedra act as the building block for different polymorphs of MnO_2. Depending on the size and orientation of the open channel between these octahedra building blocks, MnO_2 can be categorized as α-, β-, γ-, δ-, and λ- phases, which has 2×2, 1×1, 2×1 sized 1-D tunnel, 2D tunnel and 3D tunnel, respectively (Fig. 32).[135]

3.1.1 α-MnO_2

α-MnO_2 (also Hollandite phase) has 2×2 sized tunnels (Fig. 32), which provides large ion transport channels. For this reason, it has been demonstrated as an intercalation cathode for LIBs.[136-139] Since the size of the channel (~5 Å) is much larger than the size of Mg^{2+} (0.86 Å), transport of Mg^{2+} along the channels is speculated to be energetically feasible.[140-144] For Mg concentration less than 0.25 in α-Mg_xMnO_2, the migration barriers of ~300-600 meV (Fig. 33a) are comparable to that for Li diffusion in typical LIBs cathodes.[145] At a Mg concentration higher than 0.25, the diffusion barrier significantly increases to ~1300-1400 meV, much higher than the threshold of ~525 meV, suggesting that the insertion of Mg^{2+} beyond 0.25 is not kinetically practical.[11]

It was experimentally demonstrated when a low magnesium concentration was intercalated (0.14 or 0.26 Mg/α-MnO_2), α-MnO_2 showed a good cycling performance. While a high magnesium concentration was intercalated (0.47 Mg/α-MnO_2), the capacity faded quickly, in accordance with the calculations.[142, 143, 146] Attempts have been made to advance the cycling performance, such as adding acetylene black into α-MnO_2 to enhance its electronic conductivity,[144] and stabilizing α-MnO_2 tunnels with K^+ cation,[83] but without success.

The experiment on MnO_2 with various morphologies further revealed that the magnesiation process was strongly governed by the active surface area of MnO_2 (Fig. 33b).[143] Microscopic and spectroscopic investigations found that an amorphous layer was generated in the α-MnO_2 after the first electrochemical magnesiation,[83] while crystalline grains were still observed in the center of the nanorod, forming a core@shell morphology. Manganese was reduced to Mn^{2+} in the shell, whereas Mn^{4+} remained in the core. This experimental observation indicates

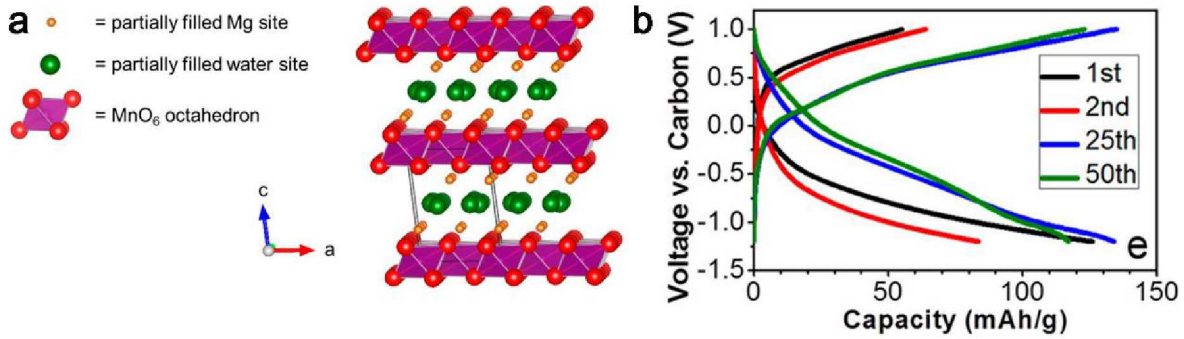

Fig. 35 (a) Birnessite crystal structure showing a water monolayer between the MnO_2 sheets. (b) Electrochemistry of δ-MnO_2/carbon cloth for RMBs in the nonaqueous electrolyte at C/10. Reproduced from ref. 149 with permission from American Chemical Society, Copyright 2016.

the discharge of alpha-MnO_2 results in a conversion reaction outcome.

To reveal why the conversion reaction occurs during magnesiation of α-MnO_2, a comprehensive analysis is conducted.[141] Most stable phase of discharge products is calculated to be the mixture of crystalline MgO and manganese oxide (Fig. 34a), which, however, may not form in practical operation due to kinetic hindrance from phase transformation. The energy to form amorphous Mg_xMnO_2 is lower than that to form intercalated α-Mg_xMnO_2, and the voltage for the formation of amorphous oxides is always higher than that for the intercalation reaction (Fig. 34b), indicating the thermodynamic preference for the reaction to occur via the conversion path. Besides, volumes of amorphous oxide are reduced compared to the intercalated crystalline compounds (Fig. 34c), which is beneficial for relaxing the expansion caused by the insertion of Mg, and further improves the thermodynamic stability of amorphous Mg_xMnO_2 relative to intercalated α-Mg_xMnO_2. Therefore, two possible reaction routes exist (Fig. 34d): the direct conversion from the beginning, which is thermodynamically preferable, or starting with partial Mg-intercalation, followed by the structure destruction. Even if the metastable intercalation could occur, the concentration of intercalated Mg is limited to α-$Mg_{0.125}MnO_2$, beyond which the structure of intercalated compound undergoes a strong tetragonal to orthorhombic distortion, resulting in the formation of magnesium and manganese oxides. Above all, the conversion path is thermodynamically preferable against the intercalation path, consistent with the experimental observation that the discharge of α-MnO_2 forms an amorphous shell of magnesium and gradually reduced manganese oxides.

Other than α-MnO_2, few studies are performed on other 1D MnO_2 either due to their small size of the tunnel (β) or the complexity of the structure.[135, 143, 147, 148]

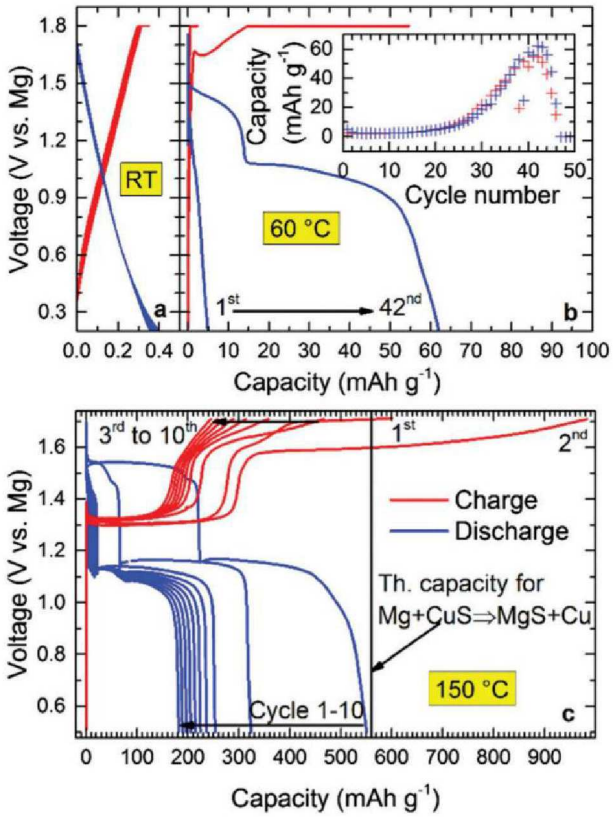

Fig. 36 Galvanostatic discharge and charge curves of CuS cycled at: (a) 25 °C in APC-THF; (b) 60 °C in APC-THF; (c) 150 °C in APC-G4. Reproduced from ref. 155 with permission from Royal Society of Chemistry, Copyright 2016.

3.1.2 δ-MnO_2

δ-MnO_2, or birnessite, consists of stacked MnO_2 planes with structural water in the interlayer space with interlayer distance of ~7 Å, which provides 2-dimensional diffusion path for Mg^{2+} (Fig. 35a).[149]

Mg^{2+} intercalation into δ-MnO_2 has been reported under aqueous conditions,[149, 150] which will be discussed in the following section. In 0.25 M $Mg(TFSI)_2$/diglyme electrolyte, δ-MnO_2 showed a capacity of ~135 mA h/g after 20 cycles at C/10 before the capacity slowly decayed (Fig. 35b).[149] A conversion mechanism takes place during cycling in the non-aqueous electrolyte, with the formation of MnOOH, MnO, and $Mn(OH)_2$ upon discharge, which might not only result from the slow diffusion kinetics of Mg^{2+}, but also the presence of surface bonded $TFSI^-$ blocking the intercalation. No calculations about the diffusion barriers of Mg^{2+} in δ-MnO_2 have been done, neither for the thermodynamic stability of intercalated products. However, according to the experimental results, the diffusion barriers are probably too high to intercalate Mg^{2+}.

For spinel λ-MnO_2, as discussed in section 2, a very low degree of magnesiation was obtained (<3 at. % Mg per λ-MnO_2)

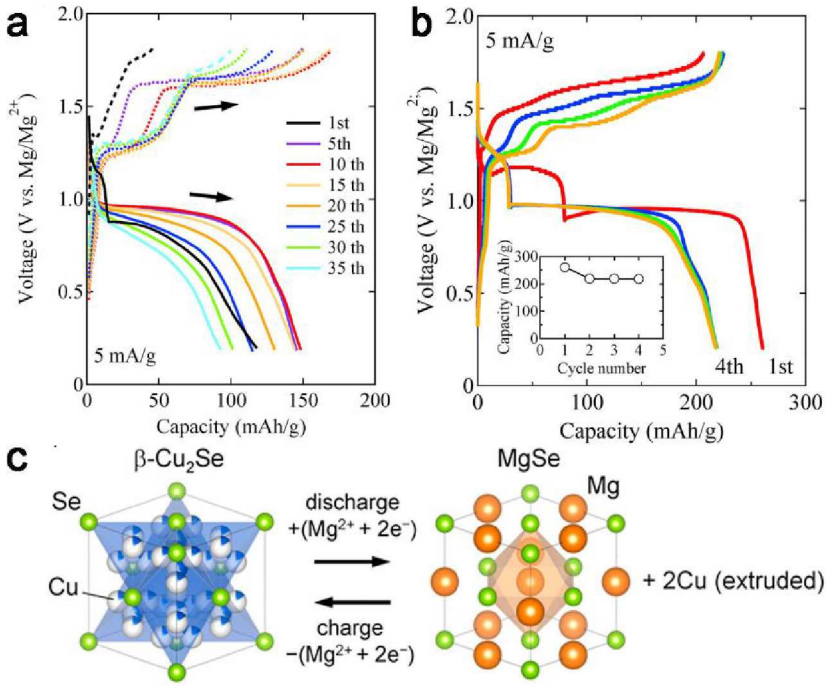

Fig. 37 The charge/discharge curve of β-Cu_2Se cathode with the length of (a) 1μm and (b) ~100 nm. (c) The schematic Fig. for the displacement of Cu ions in β-Cu_2Se with Mg ions to MgSe. Reproduced from ref. 163 with permission from Elsevier, Copyright 2016

in non-aqueous.[29] However, no convincing evidence exists for Mg^{2+} intercalation into λ-MnO_2. Based on the discussion on α-MnO_2 and β-MnO_2, a conversion reaction may also happen, generating amorphous magnesium and manganese oxide, which blocks the further magnesiation of λ-MnO_2. This speculation needs to be further confirmed.

3.2 Chalcogenide

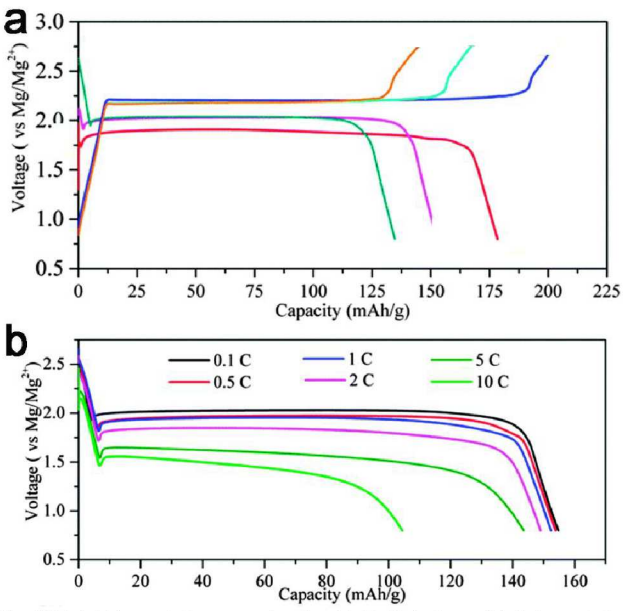

Fig. 38 (a) Galvanostatic curves for the Mg/AgCl battery. (b) Galvonostatic discharge curve for the AgCl/Mg batteries at different C rate. 1C is equal to 186 mA/g. Reproduced from ref. 164 with permission from Royal Society of Chemistry, Copyright 2015

3.2.1 CuS

As ion diffusion in solid state and desolvation process upon interfacial charge transfer are thermal activated process,[151-154] high temperature test is necessary for many materials which do not show electrochemical activity at RT. Recently, Nazar et al. proposed a high temperature test protocol, and successfully realized reversible Mg intercalation/de-intercalation in both spinel[24] and layer TiS_2[22] at 60 °C. Also, with modified Swagelok cell in APC/G4, CuS with 5-10 mm particles achieved an initial discharge capacity of 550 mA h/g at 150 °C, corresponding to 98% of the theoretical capacity (Fig. 36),[155] in contrast to its negligible capacity at RT. Although the high temperature helps to overcome the low mobility of Mg^{2+}, it also increases the kinetics of parasitic reactions. Further work, like binder optimization and nanosizing CuS particles,[156] need be done to achieve comparable capacity at lower temperature.

3.2.2 Cu_2Se

According to the discussion in section 2, selenides can present a better kinetics than oxides and sulfides. β-Cu_2Se, as a super ionic conductor due to the high mobility of Cu^+,[157-159] has been demonstrated to be feasible for the reversible displacement reaction, which belongs to a subcategory of conversion reaction.[160-162] When used as the cathode for RMBs, β-Cu_2Se delivered a specific capacity of ~120 mA h/g at 5 mA/g (Fig. 37a), which increased to 230 mA h/g (88.5 % of its theoretical capacity) with nanosized crystals (Fig. 37b) at RT (Fig. 37c).[163] Despite of high capacities at RT, the practical application of β-Cu_2Se is limited, due to the heavy and poisonous selenium.

Displacement reactions open a path to search a new class of electrode materials for RMBs. However, up to now, only several copper compounds have been reported to follow the displacement mechanism, because of the high mobility of

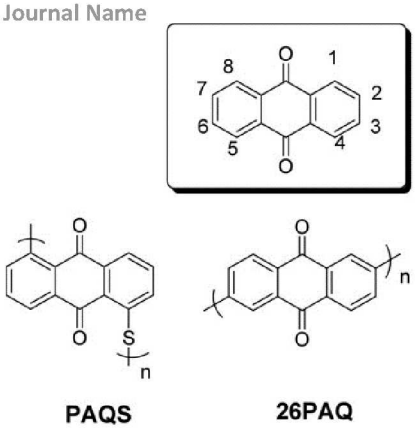

Scheme 1. The nomenclature of anthraquinone and the chemical structures of PAQS, 26PAQ, and 14PAQ. Reproduced from ref. 173 with permission from Wiley-VCH, Copyright 2016.

copper ion. Further study on other metal compounds with high mobility needs to be done.

3.3 Chloride

Given slow solid state diffusion of Mg^{2+}, a novel conceptual Mg battery is proposed to address the kinetic hurdle by using chloride as the cathode.[164] In these materials, formed $MgCl_2$ can easily dissolve into the electrolyte, avoiding the sluggish solid state Mg^{2+} diffusion, thus achieving ultrafast rate capability. AgCl/Mg battery achieved an initial discharge capacity of 178 mA h/g (95.2 % of the theoretical capacity) at 0.12 C (23 mA/g) with a flat plateau of ~2.0 V (Fig. 38a). Even at 10 C, the capacity remains at 104 mA h/g (Fig. 38b), which is the highest rate capability ever reported for RMBs and can be attributed to the high mobility and high reversibility of Cl^- anion species.

In view of high solubility of chloride in organic electrolyte, AgCl/Mg battery suffers from poor cyclability. Also, the energy density of the AgCl/Mg battery system is compromised by the adequate amount of electrolyte imperative to dissolve the discharged product, "$MgCl_2$".[164] Nevertheless, its high rate capability enables AgCl/Mg battery suitable for special applications requiring high rate like unmanned planes.

3.4 Organic compounds

As discussed above, inorganic intercalation materials are limited by slow diffusion of Mg^{2+}, along with low intrinsic conductivity. An alternative approach is to use redox-active organic materials in which intermolecular forces may be weaker than those in inorganic materials and thus interacting less

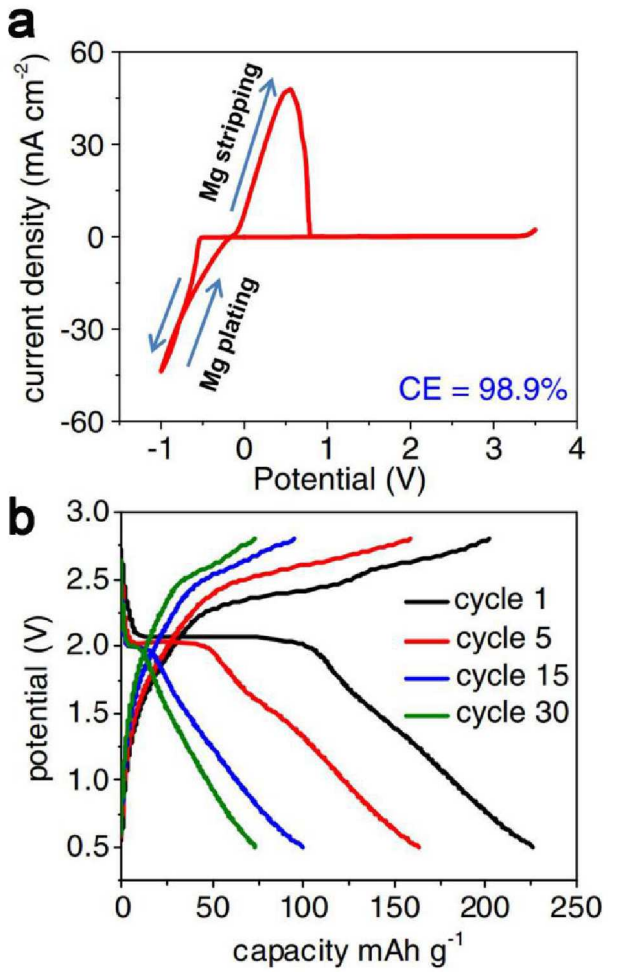

Fig. 39 (a) Steady state cyclic voltammograms in 0.5 M $Mg(TFSI)_2$-$2MgCl_2$/DME (b) Representative charge-discharge profiles of the Mg-DMBQ cell using the 0.5 M $Mg(TFSI)_2$-$2MgCl_2$ in DME electrolyte at a current rate of 0.2C. Reproduced from ref. 171 with permission from The Electrochemical Society, Copyright 2016.

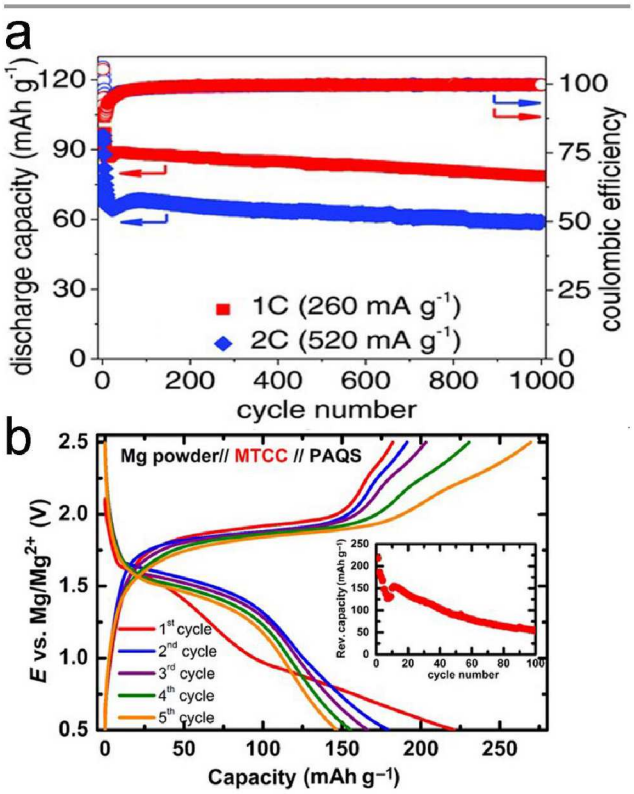

Fig. 40 (a) Mg-14PAQ cycling performance in the $Mg(HMDS)_2$-$4MgCl_2$/THF electrolyte: capacities and Coulombic efficiency profiles at the current rates of 1 C and 2 C (1C=520 mA g^{-1}). Reproduced from ref. 173 with permission from Wiley-VCH, Copyright 2016. (b) Galvanostatic curves for cycling of PAQS in MTCC between 0.5 and 2.5 V with a current density of 50 mA/g. Reproduced from ref. 175 with permission from Wiley-VCH, Copyright 2015.

strongly with Mg^{2+}.[6] In contrast to the valence change of the transition-metal in inorganic cathodes, the redox reaction is based on the charge state change of the electroactive organic group or moiety in organic cathodes.[165-168] The abundance and diversity of organic materials, benefiting from their flexible structure and tunability, can provide an opportunity for high-capacity and high-rate organic cathodes for RMBs, especially in terms of the resource sustainability and environmental friendliness.

An typical organic material is quinone.[169] 2,5-dimethoxy-1,4-benzoquinone (DMBQ) was reported to have low solubility in electrolyte,[170] high theoretical capacity (319 mA h/g),[171] and much slower capacity decaying upon cycling in LIBs.[170] However, when used as cathodes for RMBs, its capacity faded fast, and low discharge voltage and large overpotential (~1 V) were observed, which was likely due to the non-compatibility of electrolytes with metal Mg.[172]

Another two magnesium electrolytes ($Mg(TFSI)_2$-$MgCl_2$/DME and $Mg(TFSI)_2$/diglyme) were applied to study DMBQ.[171] $Mg(TFSI)_2$-$2MgCl_2$/DME, which were capable of plating/stripping Mg (Fig. 39a), enabled Mg-DMBQ batteries with a discharge potentials of ~2.0 V (Fig. 39b), higher than the previously reported potential (1.1 V).[169, 172] However, a considerable capacity loss, caused by electrode dissolution, was observed upon cycling.[171]

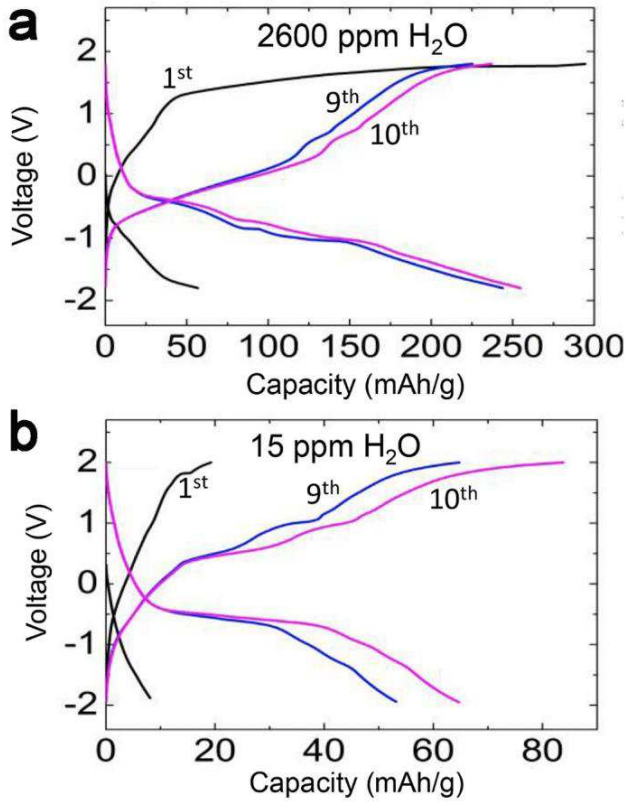

Fig. 41 Galvanostatic cycling of α-V_2O_5 vs carbon coin cell in 1 M $Mg(TFSI)_2$/G2 (a) with 2600 ppm H_2O, (b) 15 ppm H_2O at 20 mA/cm^2. Reproduced from ref. 60 with permission from Elsevier, Copyright 2016.

In addition to DMBQ, two new quinone-base polymers, 2,6-polyanthraquinone (26PAQ) and 1,4-polyanthraquinone (14PAQ) (Scheme 1) are reported.[173] In contrast to the slow capacity fading of 26PAQ, 14PAQ showed the best cycling stability in the $Mg(HMDS)_2$-$4MgCl_2$/THF electrolyte. Beyond the considerable capacity loss in the first few cycles, more than 1000 cycles with slight loss of capacity and good rate capacity of 14PAQ were achieved (Fig. 40a).[173] Unlike the structurally rigid polymer chain of 26PAQ, the redox-active quinonyl moieties in 14PAQ lies on the side of the main polymer chain (Scheme 1), which allows the rotation flexibility of anthraquinonyl groups along the polymer chain. The rotation flexibility helps to minimize the space hindrance and relax the structural stress of the polymer, which in turn provides better structure stability for 14PAQ.[173] In addition, upon discharging, the inserted Mg^{2+} species can be better stabilized by the two adjacent carbonyl (C=O) groups via the chelating effect, which have also been demonstrated to account for the enhanced cycling performance.[174]

PAQS was also investigated as the cathode for RMBs with three different non-nucleophilic electrolytes: [Mg_2Cl_3-6THF][$HMDSAlCl_3$] in THF (MHCC), $MgCl_2$-$AlCl_3$ in THF (MACC), $MgCl_2$-$Mg(TFSI)_2$ in a mixture of THF and glyme (MTCC). Capacities between 150 and 200 mA h/g at 1.5-2.0 V were obtained (Fig. 40b).[175] Among the three electrolytes, MTCC showed the best performance in terms of capacity and rate capability, but without significant improvement in long-term cycling over MHCC and MACC.[175]

In summary, benefit from low cost and environmentally benign, organics can be promising cathodes for RMBs. Yet, some challenges remain: the development of electrolyte systems to suppress electrode dissolution, discovery of more efficient electroactive structures, understanding of charge/ion transport mechanism, and approaches to improve electrode stability.

4. Water co-intercalation

As discussed above, kinetics of intercalation cathodes with organic electrolytes are limited by slow interfacial charge transfer and sluggish diffusion. Studies have revealed that trace water in organic electrolyte can co-intercalate with Mg^{2+}, which could accelerate both interfacial ion transfer and ionic diffusion because of screening effect.[29, 30, 60, 149, 150, 176]

The important role of water in wet electrolyte during Mg^{2+} intercalation is investigated in α-V_2O_5 without H_2O in the structure. α-V_2O_5 could achieve the capacity of 260 mA h/g using 1 M $Mg(TFSI)_2$/G2 with 2600 ppm water in the electrolyte (Fig. 41a), much higher than 60 mA h/g in the dry electrolyte system (with 15 ppm H_2O) (Fig. 41b).[60] NMR results indicate that protons might participate in the intercalation process. However, the content of intercalated protons, as well as the relationship between the proton intercalation and the water concentration in electrolyte, are to be explored.

To identify which species (e.g., desolvated magnesium ions, protons, hydronium ions, water- or solvent-solvated magnesium ions, or any combination of these) are intercalated

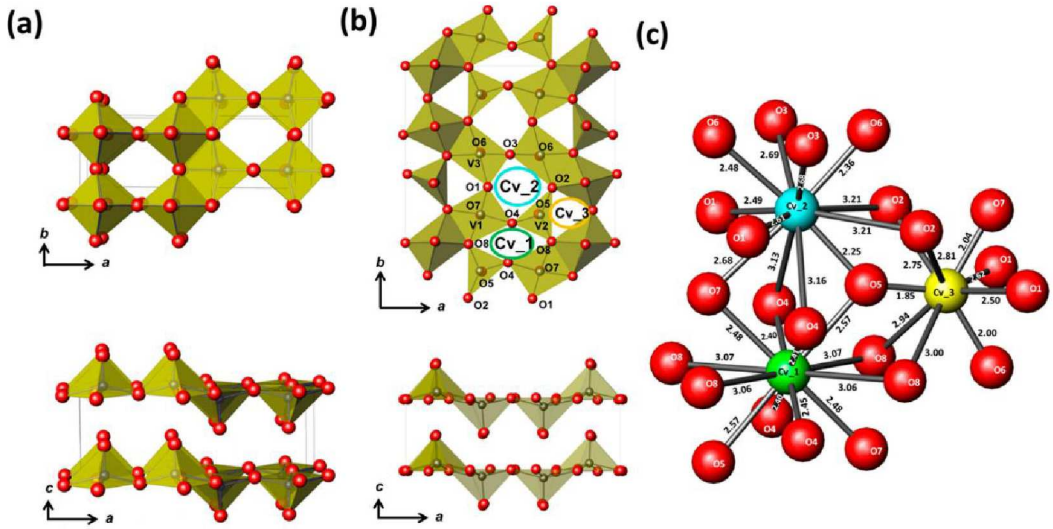

Fig. 42 (a) Crystal structure of the pristine V_2O_5, (b) Mg-inserted V_2O_5, and (c) local structures surrounding the cavity sites denoted as Cv m(m= 1, 2, 3) in panel b. The numbers denote interatomic distances. Reproduced from ref. 177 with permission from American Chemical Society, Copyright 2017.

into host structure during the electrochemical reduction, the crystal structure of the magnesium-inserted α-V_2O_5, electrochemically reduced in the wet organic electrolyte, was studied.[177] The refined crystal structure was compared with the original V_2O_5 structure (Fig. 42). Distortions from the original VO_3 square pyramidal symmetry can be clearly found (Fig. 42b), where V1 and V3 maintain the five-coordination with oxygen, while V2 has only four oxygen atoms like a tetrahedron. Eight oxygen atoms with similar center-to-oxygen distances of ~2.47 Å coordinate the Cv_1 site (Fig. 42c). Therefore, the Cv_1 cavity size is sufficient for a single ion (Mg^{2+} or proton), but too small for solvated magnesium, such as $Mg(H_2O)_n^{2+}$ or Mg(solvent, $H_2O)_n^{2+}$, or for H_3O^+ or H_2O.

The Cv_2 site is coordinated by 12 oxygen atoms with various center-to-oxygen distances (average of 2.76 Å) (Fig. 42c). Even though this cavity appears to be slightly larger than Cv_1, it is unlikely occupied by species other than single magnesium or protons, because the closest distance to lattice oxygen, not the average value, is the determining factor for its suitability. The closest distance of the 12 center-to-oxygen distances in Cv_2 is shorter than 2.25 Å. The Cv_3 site is surrounded by nine oxygen atoms with an average center-to oxygen distance of 2.48 Å (Fig. 42c), which, similarly, is too small to accommodate H_2O or larger chemical species other than single magnesium ions or protons. Consequently, the only species intercalated into the vanadium pentoxide can be Mg^{2+} and H^+, and not the other species ($Mg(H_2O)_n^{2+}$, Mg(solvent, $H_2O)_n^{2+}$, H_3O^+ or H_2O), which is not consistent with the previous simulation[66]. Yet, it is still not clear about how many H^+ are intercalated, and further work need to be done.

In Xerogel V_2O_5 with structural H_2O (Fig. 21), water co-intercalation with Mg^{2+} depended on the water activity in the electrolyte, ranging from full co-intercalation in wet to none in superdry conditions (Fig. 43a). The measured voltages would change if the co-intercalation of the solvent/electrolyte with the redox ion occurs, leading to a co-dependence on the solvent/electrolyte chemical potential (Fig. 43b). The Mg^{2+} intercalation voltage was calculated to be higher in a wet electrolyte than in a dry electrolyte.

Birnessite MnO_2, with structural H_2O (Fig. 35a), achieved increasing specific capacity as the water concentration in acetonitrile-based electrolyte rises, in conjunction with decreased overpotential values (Fig. 43c).[150] As the water concentration in the electrolyte increases, the water content in Birnessite MnO_2 host becomes higher (Fig. 43d), which confirms the insertion of hydrated Mg^{2+}. The maximal number of water molecules that are co-intercalated into Birnessite MnO_2 together with each Mg^{2+} is around 3.

In wet electrolyte, the proton intercalation will always happen,[178, 179] while the amount of intercalated protons are related with the water activity. The hydrated Mg^{2+} intercalation depends on the sufficient interlayer space of cathodes. Even though the capacity and rate capability of Mg^{2+} intercalation into cathodes can be improved by the presence of water in organic electrolytes, this approach has some drawbacks. It leads to a large effective radius of the intercalated moieties, which may lead to excessive structural deformations of the host. Also, wet solutions are not compatible with magnesium anodes. The feasibility of Mg^{2+} co-intercalation with polar organic molecular, which can screen the interaction between Mg^{2+} and the host lattice, is worth investigating.

5. Elemental redox chemistry

As introduced above, cathodes based on intercalation and conversion mechanism suffer from limited energy density. With regard to the high energy density system, the ideal materials to couple with Mg are O_2 and S. Mg/O_2 system exhibits a higher energy density of 3900 Wh/kg than Li/O_2 if MgO is the final product, while Mg/S system offers a theoretical energy density of 1722 Wh/kg, both of which are over ten times higher than that of Chevrel phase (140 Wh/kg).

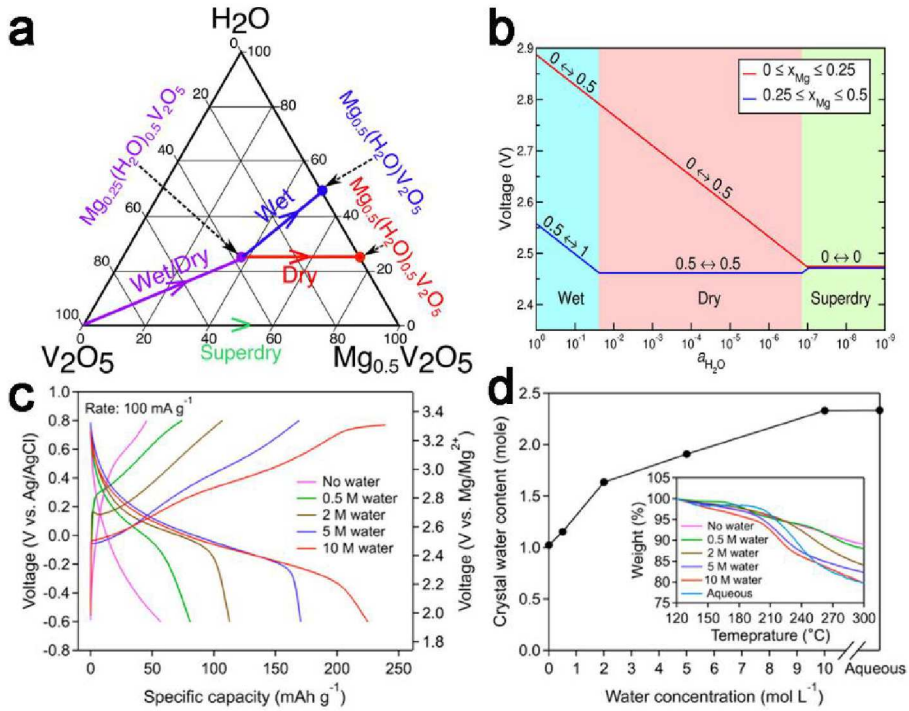

Fig. 43 (a) Ternary phase diagram of the Mg-(Xerogel) V_2O_5-H_2O system, which summarizes the possible equilibrium phases under different electrolyte conditions. (b) Average Mg insertion voltage for low (red line) and high (blue) Mg concentrations as a function of the electrolyte water content (aH_2O). Reproduced from ref. 66 with permission from American Chemical Society, Copyright 2016. (c) The first discharge-charge voltage profiles of the Birnessite MnO_2 cathodes with different water concentrations in acetonitrile-based electrolyte. (d) The water contents in Mg-B at fully discharged state obtained from TGA profiles (inset). Reproduced from ref. 150 with permission from American Chemical Society, Copyright 2015.

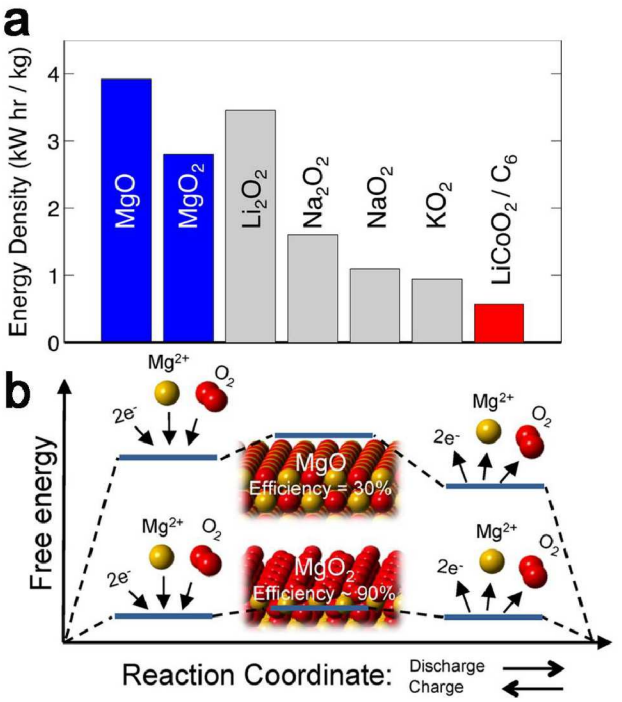

Fig. 44 (a) Theoretical specific energies (per mass of discharge product) of selected metal-oxygen chemistries (blue and gray bars) compared to Li-ion (red bar). Reproduced with permission. (b) The free energy and efficiency of MgO_2- and MgO-based cells. Reproduced from ref. 182 with permission from American Chemical Society, Copyright 2016.

5.1 Mg-O_2

Nonaqueous metal/oxygen batteries possess high theoretical energy densities (Fig. 44a).[180-182] Chemistries based on alkali metals, such as Li/O_2,[181, 183-185] Na/O_2,[181, 186, 187] and K/O_2,[188] are the most studied, while Mg/O_2 chemistry receives much less attentions. In a Mg/O_2 cell, the half-reactions (2) and (3) could be anticipated at the gas electrode.[189] A Mg/O_2 cell with a MgO discharge product would exhibit theoretical volumetric and gravimetric energy densities of approximately 14 kWh L^{-1} and 3.9 kWh kg^{-1}, respectively, surpassing Li/O_2 cells that discharge to Li_2O_2 (8.0 kWh L^{-1} and 3.4 kWh kg^{-1}) (Fig. 44).[189]

The mechanism of Li/O_2 system is well understood, in which oxygen reduction via a one-electron transfer is the most kinetically favorable, which leads to the formation of LiO_2 ($Li^+ + O_2 + e^- \rightarrow LiO_2$).[190, 191] As LiO_2 is highly unstable, it further reacts to form lithium peroxide (Li_2O_2) either by one-electron-transfer electrochemical process ($LiO_2 + Li^+ + e^- \rightarrow Li_2O_2$) or by disproportion reaction ($2LiO_2 \rightarrow Li_2O_2 + O_2$).[186] In contrast, the reaction mechanism for Mg/O_2 cell remains poorly understood.

Density Functional Theory calculations are employed to characterize discharge/charge mechanisms on the surfaces of plausible discharge products, MgO and MgO_2.[182] MgO_2-based cells were predicted to be much more efficient: superoxide-terminated facets on MgO_2 crystallites enabled high round-trip

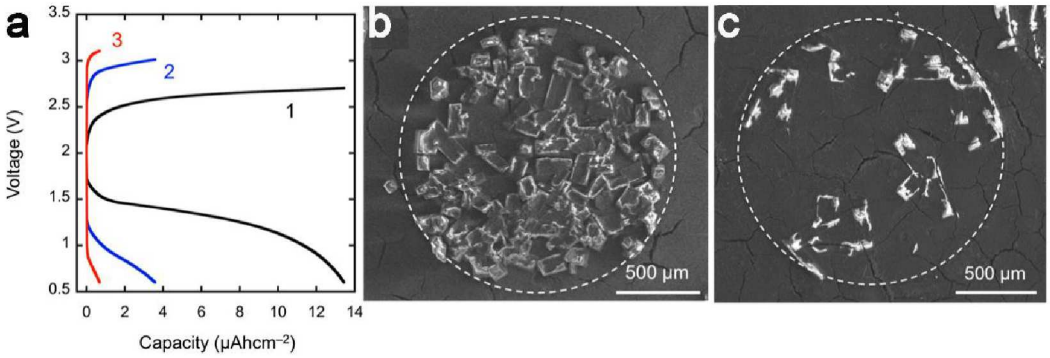

Fig. 45 (a) Discharge/recharge cycles for a room-temperature Mg/O_2 cell. SEM images of the positive-electrode surface on the side closest to the O_2 gas inlet. The dashed circles represent boundaries of the regions that were directly exposed to O_2 through perforations in the Pt-coated current collector. (b) An electrode after first discharge. (c) An electrode at the end of first recharge. Reproduced from ref. 189 with permission from American Chemical Society, Copyright 2015.

efficiencies approaching 90% (Fig. 44b), and low overpotential, ranging from 0.11 to 0.18 V for discharge and 0.07 to 0.33 V for charge, which are slightly lower than 0.35 and 0.68 V for discharge and 0.2 and 0.4 V for charge with Li_2O_2 as the discharged product in Li/O_2 system.[192] In contrast, cells discharged to MgO exhibit low round-trip efficiencies (30%), which were rationalized by the presence of large thermodynamic hysteresis (the calculated discharge/charge voltages of 1.15/~4 V). This trend that superoxide-based cells exhibit much lower overvoltage and higher round-trip efficiencies than those that discharge to a peroxide, is consistent with the behavior of other metal oxygen batteries based on potassium,[188] sodium.[186, 193]

Experiments are performed to probe the discharged and charged products and verify the reaction mechanism. During the first cycle (Fig. 45a), the discharged product comprises roughly 70% MgO and 30% amorphous MgO_2 on a volumetric basis (Fig. 45b). This product was formed after electrochemical superoxide formation (equation (2)), through chemical precipitation and disproportionation steps (equation (4)).[189] The recharged positive electrode contains a small amount of residual MgO (Fig. 45c), suggesting that MgO_2 decomposes first during charging, followed by the slower MgO decomposition. Accordingly, the reaction pathway is concluded: during discharge, MgO_2 is firstly formed, followed by partial MgO_2 decomposed to MgO through a disproportionation step, during charge, MgO_2 decomposes first, followed by more limited MgO decomposition.

According to the calculated and experimental results, several measures can be taken to improve the performance of Mg/O_2 system. By using a redox mediator, MgO can be cycled reversibly via a liquid-phase reaction pathway, with lower overvoltage and higher capacities. Increasing the oxygen pressure and reducing the operation temperature can produce MgO_2 rather than MgO, resulting in much higher round-trip efficiency. Besides, development of electrolytes with higher O_2 solubility and ionic conductivity could facilitate improvements in both the capacity and rate capability.

Based on the analysis above, iodine was added into $Mg(ClO_4)_2$-DMSO electrolyte to form iodine-DMSO complex by a charge-transfer interaction between DMSO and the bonds of the iodine molecule to catalyze the decomposition of MgO.[194] The catalytic cycle for the $Mg-O_2$ electrode was proposed by combining decomposition of MgO with the $I^{3-}/3I^-$ redox couple (Fig. 46a). $Mg-O_2$ batteries with iodine showed a discharge capacity of 2131 mA h/g and charge capacity 1590 mA h/g in the first cycle, in contrast with no charging behavior without iodine (Fig. 46b). Similarly, 2,2,6,6-tetramethylpiperidine-oxyl (TEMPO)-anion complex was also employed to catalyze the decomposition of MgO during the charge of Mg-oxygen battery, which exhibited rechargeable behavior over several cycles (Fig. 46c).[195] Also, two dual redox mediators, 1,4-Benzoquinone (BQ) and 5,10,15,20-Tetraphenyl-21H,23H-porphine cobalt(II) (Co(II)TPP), were introduced to facilitate both the discharge and recharge processes of $Mg-O_2$ battery operations, showing promising results.[196]

On the basis of the calculations, MgO_2-based cells can achieve high round-trip efficiencies and low thermodynamic hysteresis. And development of electrolytes with higher O_2 solubility facilitates producing MgO_2. Recently, a nonaqueous Mg/O_2 cell based on the all-inorganic magnesium aluminum chloride complex in dimethoxyethane electrolyte (MACC/DME) with higher O_2 solubility and ionic conductivity, was demonstrated to exhibit high discharge capacity (Fig. 46d).[197] However, poor rechargeability is observed, which is explained by the formation of an insulating product film, a mixture of $Mg(ClO_4)_2$ and $MgCl_2$ likely from the decomposition of electrolyte.[197] An additional impedance rises from an inert film formation on the Mg negative electrode, which can be attributed to the detrimental O_2 crossover.

Overall, despite some progress, several challenges for pursuing Mg/O_2 with substantial performance improvement: (1) the traditional ether-based electrolytes are not compatible with oxygen chemistry; (2) the dissolved O_2 in electrolytes will passivate Mg anode; (3) redox mediators in electrolytes may react with Mg anode.

5.2 Mg-S

As a high capacity cathode material (1675 mA h/g), sulfur has attracted intense interest in Li-S and Na-S systems.[198-201] The combination of Mg with sulfur offers a theoretical of 957 mA h/g with an average voltage of 1.77 V, corresponding to the energy density of 1722 Wh/kg, over four times that of a

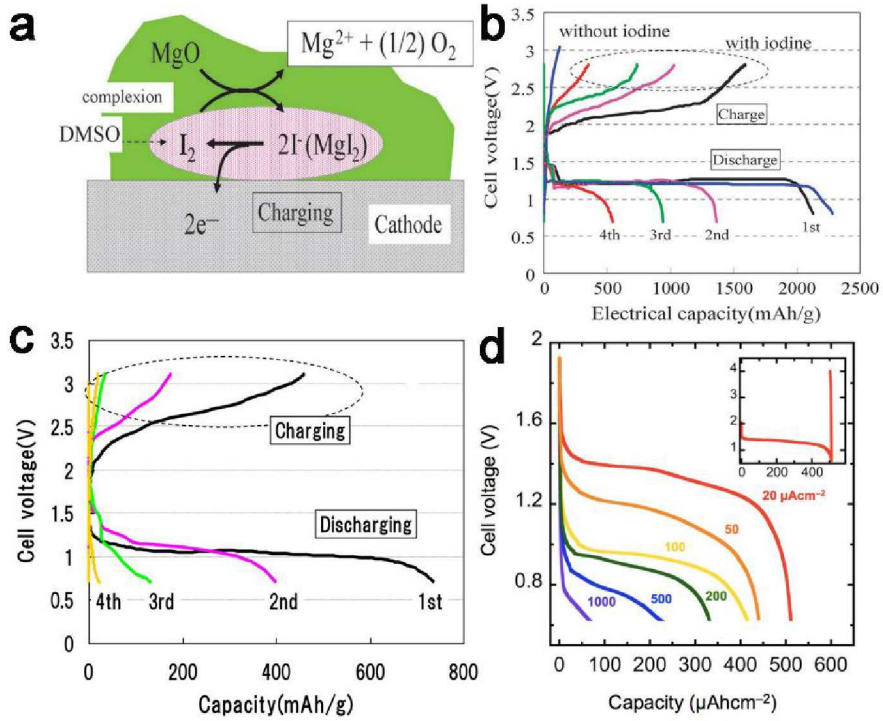

Fig. 46 (a) A proposed catalytic mechanism for the charging process. (b) Discharge-charge profiles of the non-aqueous Mg-O_2 battery with iodine, Reproduced from ref. 194 with permission from Royal Society of Chemistry, Copyright 2013, (c) with TEMPO+ClO_4^- incorporating PTMA in the cathode at 60 C, respectively. Reproduced from ref. 195 with permission from American Chemical Society, Copyright 2014. (d) Cell voltage vs capacity for Mg/O_2 cells in MACC/DME at current densities ranging from 0.02 to 1 mA/cm (superficial). The inset shows a typical discharge/charge cycle at 0.02 mA/cm. Reproduced from ref. 197 with permission from American Chemical Society, Copyright 2016.

commercial $LiCoO_2$/graphite cell.[202] However, compared to the substantial progress in Li-S batteries, the study on Mg-S battery is still on an early stage. One major challenge is to discover a suitable electrolyte that is chemically compatible to the electrophilic sulfur and capable of reversible Mg deposition/dissolution.[203] In addition, similar issues to Li/S batteries, dissolution of polysulfide and its shuttling effect, low active material utilization, and fast capacity fade, are also expected.[204, 205] In order to solve these challenges, the discovery of suitable electrolytes and a fundamental understanding of the mechanism of Mg/S chemistry are of paramount importance.

Quasi-equilibrium discharge of Mg/S battery has revealed that sulfur reaction occurs through three consecutive steps. Stage (I) elemental is sulfur to long-chain polysulfide, showing a short slope at 2.5-1.5 V ($S_8 + Mg^{2+} + 2e^- \rightarrow MgS_8$ (2.5-1.5 V)). Stage (II) is chain-shortening of polysulfide, showing a long plateau at 1.5 V ($MgS_8 + 3Mg^{2+} + 6e^- \rightarrow 4MgS_2$ (1.5 V)). Stage (III) is solid-state transition from short-chain polysulfide to MgS, showing another slope at 1.5-0.5 V ($MgS_2 + Mg^{2+} + 2e^- \rightarrow MgS$ (1.5 – 0.5 V)) (Fig. 47a).[206, 207] The reaction in stage (II) shows the fastest kinetics with small overpotential due to the synergetic effect of a fast surface reaction enabled by the dissolved polysulfide and the relative

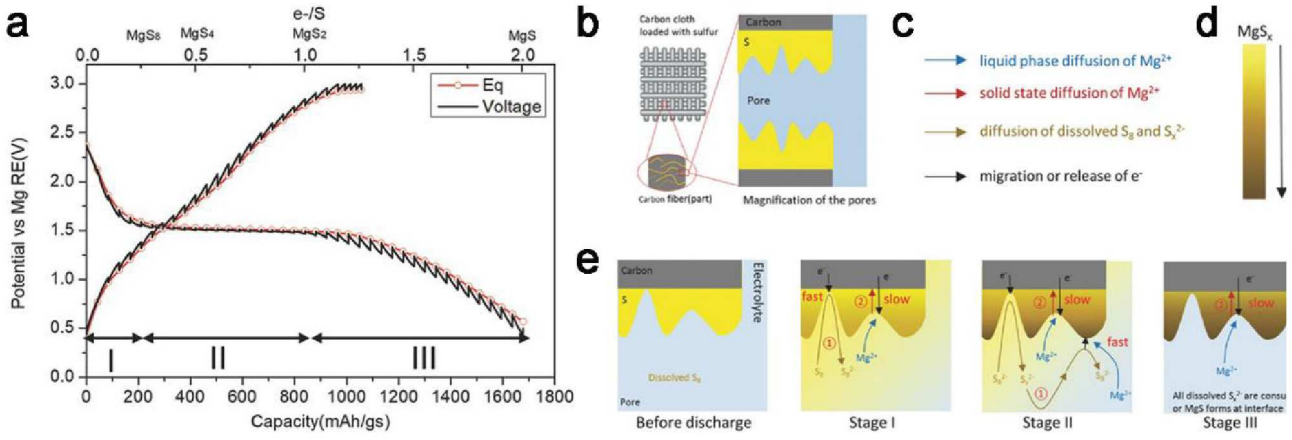

Fig. 47 (a) Thermodynamic equilibrium potential and three stages for sulfur reduction process. Schematic of sulfur reduction mechanism: (b) the structure of the carbon/sulfur composite cathode. (c) The kinetic processes during discharge. (d) Concentration of Mg in Mg-S binary compound. (e) Sulfur reduction mechanism. Reproduced from ref. 207 with permission from Wiley-VCH, Copyright 2017.

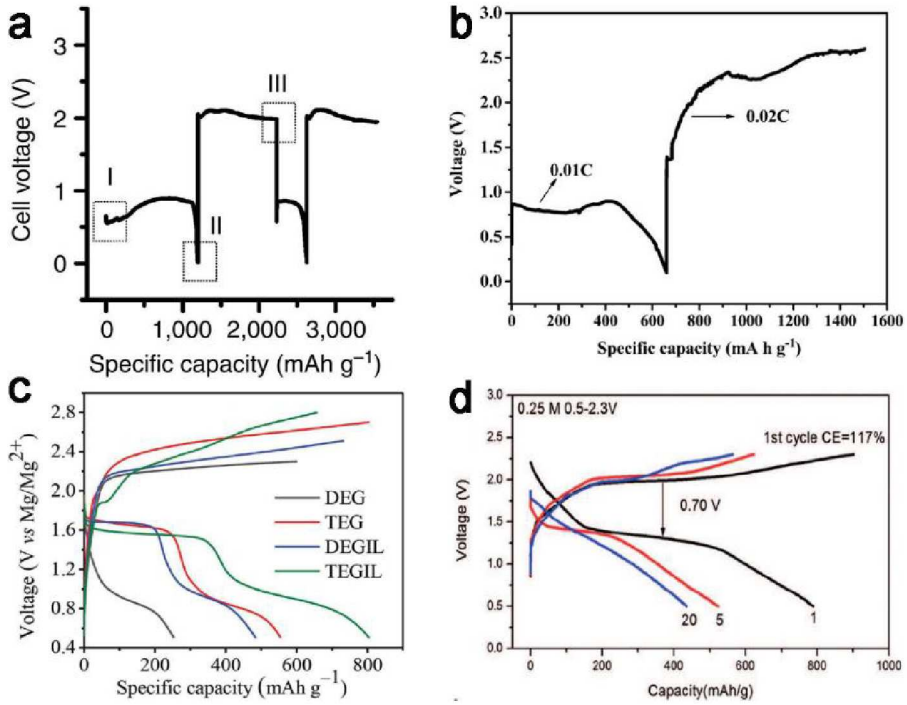

Fig. 48 (a) Discharge and charge of a Mg/S coin cell with the $[Mg_2(\mu\text{-}Cl)_3\cdot 6THF][HMDSAlCl_3]$ electrolyte, in which the Coulombic efficiency for Mg deposition/stripping is 100% at 50 and 25μA. Reproduced from ref. 208 with permission from Springer Nature, Copyright 2011. (b) The first discharge and charge profiles of Mg/S cells with the $[Mg(THF)_6][AlCl_4]_2$ electrolyte, in which the Coulombic efficiency for Mg deposition/stripping is close to 100 %. Reproduced from ref. 209 with permission from Wiley-VCH, Copyright 2016. (c) Initial discharge-charge curves of S/CMK400PEG composite using PVDF binder in diglyme (gray), tetraglyme (red), diglyme/PP14TFSI (blue), tetraglyme/PP14TFSI (green). Reproduced from ref. 206 with permission from Wiley-VCH, Copyright 2014. (d) Voltage profiles in 0.25M $MgTFSI_2/MgCl_2$/DME electrolyte with Coulombic efficiency for Mg deposition/stripping of 93%. Reproduced from ref. 210 with permission from Wiley-VCH, Copyright 2017.

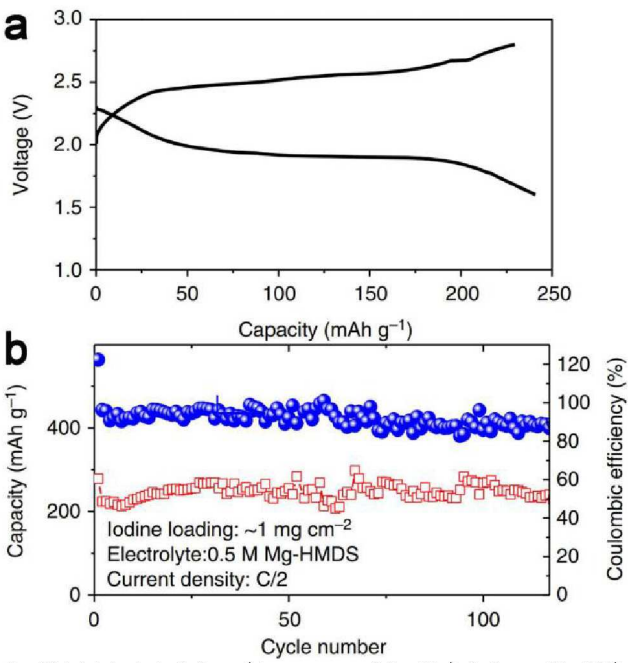

Fig. 49 (a) A typical discharge/charge curve of the Mg/I_2 battery with ACC/I_2 cathode. (b) Cycling stability of the Mg/I_2 battery at 0.5C (105.5 mA/g) with ACC/I_2 cathode. Reproduced from ref. 215 with permission from Springer Nature, Copyright 2017.

fast Mg^{2+} diffusion in the amorphous MgS_x, while the stage (III) suffers from the slowest kinetics and high polarization because of solid-state magnesiation from MgS_2 to MgS (Fig. 47b-e).

Several measures are applied to improve the performance of Mg/S system: utility of new electrolyte and/or additives,[206-210] cathode design,[211, 212] and Li^+ activating MgS_x species.[202] Progress has been achieved, but reported electrochemical performance (discharge/charge curve, voltage hysteresis, etc.) has many discrepancies (Fig. 48). These discrepancies are likely resulted from the kinetics limitation of the magnesiation of sulfur, which can alter the discharge curve to different representations due to different kinetics at different stages. Factors that can affect kinetics include: current, sulfur loading (S/C ratio), carbon host, and electrolyte chemistry. As for the large voltage hysteresis observed in some studies, the Mg anode overpotential is probably the main cause.[210]

Significant progress has been achieved regarding electrolyte development and the fundamental understanding of reaction mechanism. Yet low sulfur loading (both sulfur/carbon ratio and sulfur/electrolyte ratio), short cycling stability remain major challenges to convert Mg/S chemistry to usable technology. Some strategies in Li/S system are translatable to Mg/S system to tackle these challenges, e.g. engineering carbon host to achieve high sulfur loading, using high concentrated electrolyte, customized separators or special current collector (chemo or physio adsorption) to suppress shuttle effect and achieve better cycling stability, as demonstrated by recent experimental

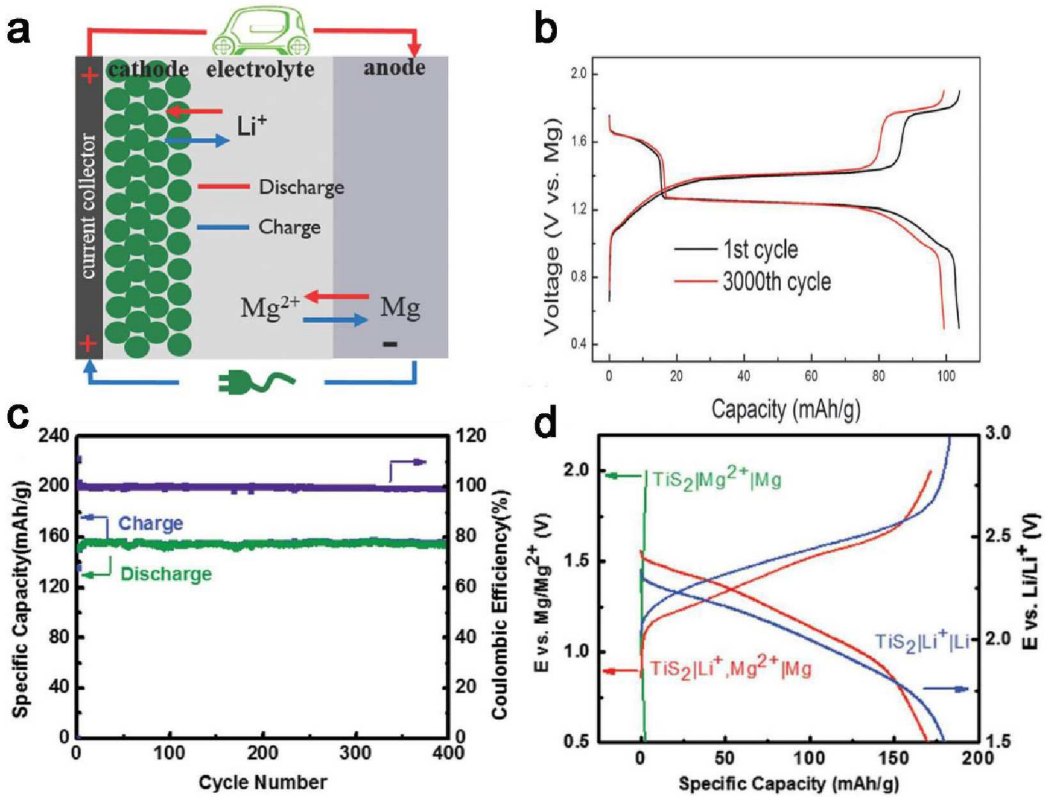

Fig. 50 (a) The operating mechanism of the hybrid Mg/Li ion battery. Reproduced from ref. 216 with permission from Wiley-VCH, Copyright 2015. (b) The charge-discharge profiles of Mo_6S_8 in hybrid Mg/Li ion battery for the first cycle and the 3000th cycle at 10 C. Reproduced from ref. 229 with permission from Royal Society of Chemistry, Copyright 2014. (c) Cycling stability of a $TiS_2|Li^+, Mg^{2+}|Mg$ battery at C/3 (1C = 240 mA h/g). (d) Discharge/charge curves of TiS_2 cathode in the $TiS_2|Mg^{2+}|Mg$ cell (1st cycle), $TiS_2|Li^+|Li$ cell (1st cycle), $TiS_2|Li^+, Mg^{2+}|Mg$ cell (2nd cycle) at 0.1 C. Reproduced from ref. 216 with permission from Wiley-VCH, Copyright 2015.

studies.[206, 210] In addition, concerns regarding the passivation of Mg anode by dissolved sulfur species may not be a threat, as recent studies point out that SEI conducting Mg ion can also form on Mg anode.[213, 214]

5.3 Mg-I_2

To address the sluggish solid-state diffusion and the slow interfacial charge transfer discussed above, a two-phase (solid-liquid or liquid-solid) reaction pathway is considered as a promising direction. I_2 is considered as a good two-phase reaction cathode, because I_2 and its partial reduction product,

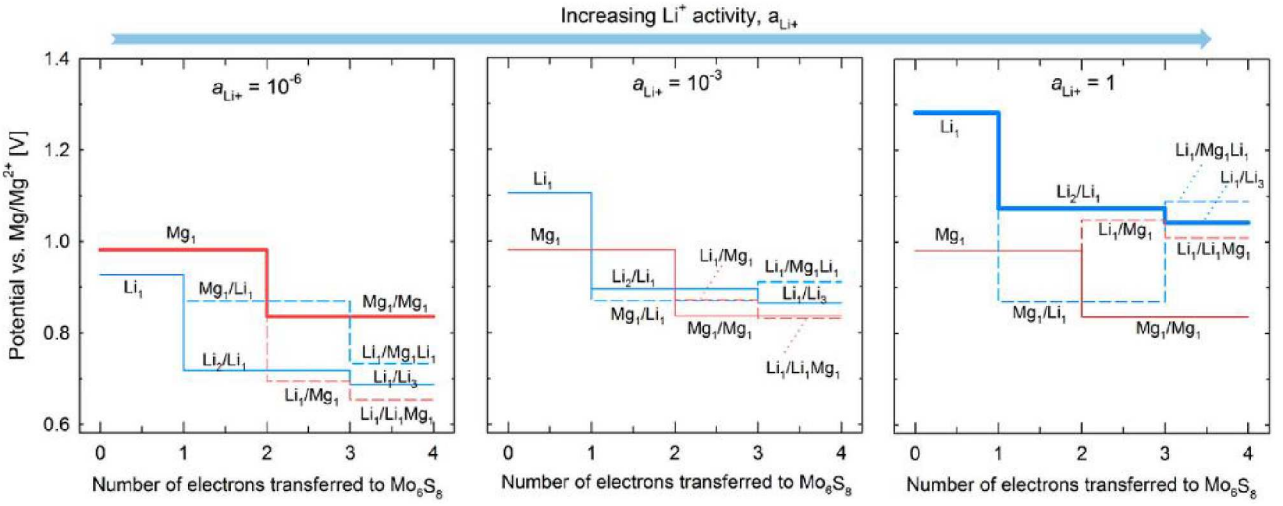

Fig. 51 Lithiation and magnesiation potentials of Mo_6S_8 (vs Mg/Mg^{2+}) at different Li^+ activities (aLi^+) determined by combining DFT energies with the Nernst equation. Mixed-insertion paths where Li^+ and Mg^{2+} occupy different sites in the same Mo_6S_8 host are shown as dashed lines. Full magnesiation and full lithiation paths are shown in bold. Reproduced from ref. 237 with permission from American Chemical Society, Copyright 2014.

$Mg(I_3)_2$, have high solubility in ether-based electrolytes, while its final reduced product, MgI_2, is insoluble.[215] The reaction mechanism for the magnesium/I_2 batteries is proposed as follows:

$$3I_2 + 2e^- + Mg^{2+} \rightarrow Mg(I_3)_2 \quad 2.8-2.0\ V \quad (5)$$

$$Mg(I_3)_2 + 4e^- + 2Mg^{2+} \rightarrow 3MgI_2 \quad 2.0-1.3\ V \quad (6)$$

A rechargeable Mg/I_2 battery provided a high capacity of ~200 mA h/g with an average voltage of 2.0 V at C/4 (Fig. 49a), corresponding to 400 Wh/kg, and excellent long-cycle stability with a capacity retention of 94.6% after 120 cycles at C/2 (Fig. 49b).[215] The rate capability of this battery is remarkable, which demonstrate the potential of enhancing Mg batteries performance by bypassing the solid state diffusion. The electrolyte is 2M Mg-HMDS in tetraglyme, in which the Coulombic efficiency for deposition/stripping of Mg is 94.5 % with the overpotential of 0.34 V. Therefore, the high Coulombic efficiency and stable cycling performance for Mg/I_2 full cells are achieved with the excess of Mg.

The success of this proof-of-concept Mg/I_2 may open an avenue towards utilizing soluble redox couples not relied on solid-state Mg^{2+} diffusion for high-performance cathodes of RMBs.

6. Hybrid System

As discussed above, RMBs suffer much from sluggish solid-state diffusion of Mg^{2+}, leading to the absence of viable cathodes, which has severely restricted the development of RMB.[216] One potential approach is to circumvent the intercalation of clumsy Mg^{2+} by coupling the Mg metal anode with a mature LIB cathode in a mixed Mg^{2+}/Li^+ electrolyte. Thus, the hybrid battery chemistry simultaneously combines the high-capacity/high-voltage LIB cathodes, fast Li^+ intercalation, and the high-capacity/dendrite-free Mg anode.[216, 217] During discharge, Li^+ is inserted into cathodes and Mg is dissolved from Mg foil into electrolyte, while during charge Li^+ is extracted from lithiated cathodes and Mg is deposited onto Mg foil (Fig. 50a).

A list of intercalation compounds have been used for this hybrid battery concept (Figure 50).[216-229] In addition to hybrid MLIBs, hybrid Mg^{2+}/Na^+ and Mg^{2+}/K^+ ion batteries are also reported based on the similar reaction mechanism with MLIBs, and achieved some progress.[230-236] They all show significant performance improvement compared to a pure Mg system, which are mainly attributed to the insertion of Li^+. To unravel the origin of the electrochemical properties of hybrid systems at the atomistic and macroscopic levels, theoretical and experimental investigations were conducted.[237] Energetically preferable occupation sites for the first ion (either Mg^{2+} or Li^+) were calculated in the primitive Mo_6S_8 crystal structure at multiple stage of discharge, and based on that, various paths of Mg^{2+} and Li^+ could be predicted (Fig. 51).[237] The insertion chemistry at the cathode strongly depends on the Li^+ activity in the electrolyte. Increasing in Li^+ activity (αLi^+) lead thermodynamically more favorable lithiation in Mo_6S_8 rather than magnesiation.

The chemical composition of the deposit in the Mg^{2+}/Li^+ mixed-ion electrolyte was examined.[216, 238] All XRD peaks of the deposition can be assigned to Mg, and no peaks can be indexed to Li or Mg–Li alloy, which was further verified by Electron energy loss spectroscopy (EELS). Although Li^+ might electrochemically react with the deposited Mg to form Li–Mg alloy in the potential range of Mg depositing, results of several experimental work confirm that the deposition was pure magnesium with no detectable lithium.[216, 238]

Despite the significantly enhanced kinetics due to Li insertion in the hybrid system, an intrinsic limitation exists for this concept. In traditional rechargeable battery, electrolyte only functions as an ion conductor so its weight does not compromise the overall energy density of the full cell. In the hybrid system, however, the electrolyte also works as an ion reservoir, i.e. storing the Li^+ needed for the cathode intercalation. For this reason, when evaluating the energy density of hybrid systems, it is necessary to consider the amount of electrolyte to make a fair comparison.

In summary, great demonstrations of hybrid systems have been shown in literature using different electrolytes and intercalation compounds. Nevertheless, the influence of electrolyte amount needs to be thoroughly studied to justify the potential of this concept. In addition, the influence of Li intercalation on Mg diffusion also needs to be examined, as co-intercalation could have positive effect on Mg diffusion, which has never been investigated before.

7. Conclusion and perspective

The dawn of the 21th century has witnessed the great success of LIBs, which now power a spectrum of applications in our daily life including portable devices, power tools, and EVs. As LIBs approach its limit, new technologies are inevitable to meet growing demands on energy storage. Despite LIBs will continue to dominate many applications due to its good combination of several performance indexes including energy density, power density and cycling stability, we believe other chemistries will become more competitive in certain applications where one or two performance indexes are critical. Rechargeable magnesium battery, coupling the high volumetric capacity of Mg metal with the safety benefit due to lack of dendrite formation, is highly suitable for applications where volumetric energy density is critical, e.g. portable electronics.

In this review, we have retrospected the latest progress of RMBs cathodes, generally categorized by intercalation compounds, conversion materials, elemental redox chemistry, and new mechanisms/concepts including water co-intercalation and hybrid systems.

Among these, intercalation compounds (with 3D, 2D, and 1D diffusion channel) are most studied. Charge transfer kinetics and Mg diffusion in the solids, especially the latter, are limiting the performance of intercalation compounds. The Mg diffusion in the intercalation compounds highly depends on their structure and chemistry, manifested in 1) connectivity between sites; 2) sizes of the diffusion channel/cavity and intercalant; and 3) interaction strength between the intercalant and host

structure. Chevrel phase shows the best kinetics because of the highly delocalized electrons effectively shielding the charge of Mg2+, and facilitated charge transfer due to the catalyst effect of surface Mo atoms. For a given structure, the chemistry of compounds plays the determining role. Taking spinel compounds as an example, in which Mg migrates along tet → oct → tet pathway, both experiments and calculations show sulfides have better kinetics than oxides due to the lower migration barriers of Mg ion, because larger sulfur anion leads to increasing size of the diffusion channel and the smaller electronegativity induces the less interaction between Mg^{2+} and host anion lattices. Such structural and chemical effects on intercalation kinetics are generalizable to other intercalation compounds including layered structure.

For polyanions, due to thermodynamic instability of magnesiation products and high Mg^{2+} migration barriers, magnesiation of olivine phosphate is prohibited by surface amorphorization. While several reports on olivine silicate ($MgFeSiO_4$, $MgCoSiO_4$ etc.) achieve reversible Mg^{2+} intercalation, which needs to be validated by more experimental and theoretical investigations. With the potential of good Mg^{2+} diffusion kinetics and high energy density, the possible utility of olivine silicates is worth pursuing further.

To improve the kinetics of Mg intercalation, measures can be taken including: 1) choosing structures with large diffusion channels; 2) Replacing anions with soft ones (S or Se) or incorporating monovalent anions (F, Cl et al) to decrease the interaction between hosts and intercalants; 3) Utilizing mixed transition metal ions (Mo, V et al) in inorganic compounds to enhance charge redistribution brought by Mg^{2+} intercalation. (4) Reducing particle sizes to decrease the Mg^{2+} migration length, and elevating temperature to improve the mobility of Mg^{2+}. In addition, more understanding on the charge transfer process at the cathode/electrolyte interface is necessary for engineering the surface of intercalation compounds for better interfacial reaction kinetics. Further systematic investigation is also required on oxides (λ-MnO_2) and polyanions to clear confusions due to some inconsistent results in the literature.

Many conversion cathodes are investigated, including transition metal oxides (MnO_2 etc.), sulfides and selenides (CuS, Cu_2Se etc.) and chloride (AgCl etc.). Due to the thermodynamic instability of the magnesiation products, amorphization occurs on the surface of various manganese oxide after initial intercalation, despite the existence of open tunnel for diffusion in their structures. Such amorphous film prevents Mg^{2+} further intercalation, causing low capacity and huge irreversibility. The amorphization does not occur in layered oxides (V_2O_5, MoO_3 etc.), and whether it will happen in other transition metal oxides with open tunnel need to be further investigated. Sulfides (TiS_2, Ti_2S_4, and TiS_3 etc.) and selenides ($TiSe_2$, WSe_2 etc.) with layered and spinel structure have been reported to undergo an intercalation reaction. While CuS and Cu_2Se without Mg^{2+} diffusion channels demonstrates a displacement reaction, which enables fast magnesiation kinetics as a result of the high mobility of copper ions. Such great performance suggests that displacement reaction could be a promising direction to explore conversion cathode materials with fast kinetics. Chlorides undergoes a solid-liquid two-phase reaction during magnetisation because the formed $MgCl_2$ can dissolve into the electrolyte. The two-phase reaction can significantly increase the kinetics due to circumvent of solid state Mg diffusion, which comes at the cost of fast capacity fading. Such ultrafast kinetics permits chloride suitable for special applications requiring high rates.

Organic materials (DMBQ, 26PAQ, 14PAQ, and PAQS) are reported to show faster kinetics than inorganic compounds, due to the weak interaction between Mg^{2+} and organic molecules. The severe dissolution and low electronic conductivity are limiting their performance, which can be mitigated by developing new electrolytes, organic polymerization, and improving the structure stability.

Mg/O_2 and Mg/S can provide high theoretical capacity and energy density. Mg/O_2 suffer from high overpotential and irreversibility due to the inert discharged products (MgO). Some redox mediators are introduced to catalyze the decomposition of MgO, which can improve the reversibility of Mg/O_2 systems, but the reaction with Mg metal anode needs carefully investigated. Methods can be taken to enhance the reversibility, including increasing oxygen pressure, reducing operation temperature, and developing electrolytes with higher O_2 solubility to produce more reversible MgO_2 et al. For Mg/S system, significant progress regarding electrolyte development has been made. The fundamental understanding of reaction mechanism have been achieved, in which a three stage reaction mechanism corresponding to long chain polysulfide formation, chain shortening to MgS_2 and formation of MgS has been revealed, with the kinetics and thermodynamics of each stage carefully investigated. Yet low sulfur loading and short cycling stability remain major challenges to convert this promising chemistry into usable technology. To address these issues, lessons can be learn from Li/S chemistry, which includes using additives, high concentrated electrolyte, customized separators and special current collector (chemo or physio adsorption).

Water co-intercalation has achieved improved magnesiation kinetics in some oxides (alfa-V_2O_5, Xerogel V_2O_5, and Birnessite MnO_2). Proton cycling has been widely demonstrated. Some fundamental questions remain to be addressed: the amount of intercalated protons; whether hydrated Mg^{2+} are cycled; how co-intercalation improves the kinetics by increasing Mg^{2+} mobility or reducing the desolvation energy.

Regarding hybrid systems, prototype cells have been demonstrated to work reversibly with different intercalation compounds. Further investigations needs to examine carefully how electrolyte amount compromises the energy density of the system, given the fact that electrolyte needs to store sufficient ions for hybrid systems to work. In addition, the influence of Li intercalation on Mg diffusion needs to be clarified. Considering the limited energy density, hybrid systems may be good choice in some certain applications where safety and fast discharge and charge are the priority.

Compared with the success of LIBs, rechargeable Mg batteries are still at the infant stage. Despite some remaining challenges, the last decade has witnessed significant progress in

the understanding of reaction mechanism and kinetic limitations of many cathode materials, which provides precious insights and guidelines for future research. Fortunately, the vast chemical space of new structures and chemistries remains unexplored, which provides possibilities for feasible cathodes with better kinetics and higher energy density. We hope this review will act as a call for more efforts into rechargeable magnesium battery, an emerging and exciting new direction in energy storage research, especially in cathode materials.

Table 1 Summary of cathodes for rechargeable Mg batteries.

		Structure	Materials	Diffusivity (meV)	Potential (V)	Capacity (mA h/g)	Reference
Intercalation	3D	Chevrel phase	Mo_6S_8	360a	0.99,[a] 1-1.3	120	7, 14, 18
		Spinel	Mn_2O_4	~650-850[a]	2.86[a], 2.9	270[a]	13, 29
			Ti_2S_4	615,[a] 550	0.89,[a] 1.2	216,[a] 200	7, 24
	2D	Layered sulfide/selenide (trigonal)	TiS_2	1160[a]	~1	115	22, 33
			$TiSe_2$		~1	130,[a] 110	38
			VSe_2		~1	110	38
		Monoclinic	TiS_3	292-698[a]	~1.2	83.7	46, 49
		Layered oxide	α-V_2O_5	975-1120[a]	2.21,[a] 2.35	150	57, 61, 65
			δ-V_2O_5	600-760[a]	2.56		61, 65
			α-MoO_3	880[a]	1.8	210	57, 77
			$MoO_{2.8}F_{0.2}$	490[a]		70	77, 84
			$Mo_{2.5+y}VO_{9+\delta}$		~2.1	235	89
	1D	olivine	$FePO_4$	580-1025[a]	~2	12	100
			Silicate	740-770[a]	~2.1-4		97, 101
	Open framework	Prussian blue analogues (PBAs)	Nickel hexacyanoferrate		2.9	80	128
		Fullerene	C60		1.2-1.6	50	115
Conversion		oxide	α-MnO_2		~2	80	142, 143, 146
			δ-MnO_2			150	149
		Chalcogenide	CuS		1.3-1.6	200	155, 156
			Cu_2Se		~1.2	230	163
		Chloride	AgCl		2	178	164
		Organic materials	DMBQ		~2	100	171
			PAQ		1.7V	150	175
			14PAQ		1.6-1.7	105	173
Water co-intercalation			α-V_2O_5			260	60
			Birnessite MnO_2		2.8	231.1	150
Elemental redox chemistry			Mg-O_2		~2.9[a]	~1300[a]	182, 189
			Mg-S		1.77[a]	957[a],600	206, 210
			Mg-I_2		2	200	215
Hybrid system		Mg/Li ion batteries					216, 229

a calculated results

Conflicts of interest

The authors declare no conflict of interest.

Acknowledgements

The authors acknowledge the support from the Army Research Office (Grant number: W911NF-15-1-0187) and Nanostructures for Electrical Energy Storage (NEES), an Energy Frontier Research Center funded by the US Department of Energy, Office of Science, Basic Energy Sciences, under Award number DESC0001160. This work was also supported by the National Natural Science Foundation of China (Grant Nos. 51302079), Hunan Provincial Innovation Foundation for Postgraduate (no. CX2016B120). M. Mao's fellowship was supported by China Scholarship Council (grant no. 201606130050). The authors thank Mr. Zengxi Wei from Hunan University for the help on schematic illustration.

Reference

1. M. Armand and J. M. Tarascon, *Nature*, 2008, **451**, 652.
2. M. S. Whittingham, *Chem. Rev.*, 2014, **114**, 11414-11443.
3. B. Scrosati, *Electrochimica Acta*, 2000, **45**, 2461-2466.
4. H. D. Yoo, I. Shterenberg, Y. Gofer, G. Gershinsky, N. Pour and D. Aurbach, *Energy & Environmental Science*, 2013, **6**, 2265-2279.
5. P. Canepa, G. Sai Gautam, D. C. Hannah, R. Malik, M. Liu, K. G. Gallagher, K. A. Persson and G. Ceder, *Chem. Rev.*, 2017, **117**, 4287-4341.
6. J. Muldoon, C. B. Bucur and T. Gregory, *Chem. Rev.*, 2014, **114**, 11683-11720.
7. M. Liu, A. Jain, Z. Rong, X. Qu, P. Canepa, R. Malik, G. Ceder and K. A. Persson, *Energy & Environmental Science*, 2016, **9**, 3201-3209.
8. M. S. Whittingham, *Chem. Rev.*, 2004, **104**, 4271-4302.
9. J. B. Goodenough and Y. Kim, *Chemistry of Materials*, 2010, **22**, 587-603.
10. H. Gwon, S.-W. Kim, Y.-U. Park, J. Hong, G. Ceder, S. Jeon and K. Kang, *Inorganic chemistry*, 2014, **53**, 8083-8087.
11. R. Malik, D. Burch, M. Bazant and G. Ceder, *Nano Letters*, 2010, **10**, 4123-4127.
12. Z. Rong, R. Malik, P. Canepa, G. Sai Gautam, M. Liu, A. Jain, K. Persson and G. Ceder, *Chemistry of Materials*, 2015, **27**, 6016-6021.
13. M. Liu, Z. Rong, R. Malik, P. Canepa, A. Jain, G. Ceder and K. A. Persson, *Energy & Environmental Science*, 2015, **8**, 964-974.
14. D. Aurbach, Z. Lu, A. Schechter, Y. Gofer, H. Gizbar, R. Turgeman, Y. Cohen, M. Moshkovich and E. Levi, *Nature*, 2000, **407**, 724.
15. E. Levi, Y. Gofer, Y. Vestfreed, E. Lancry and D. Aurbach, *Chemistry of Materials*, 2002, **14**, 2767-2773.
16. E. Lancry, E. Levi, Y. Gofer, M. Levi, G. Salitra and D. Aurbach, *Chemistry of Materials*, 2004, **16**, 2832-2838.
17. A. Mitelman, M. D. Levi, E. Lancry, E. Levi and D. Aurbach, *Chemical Communications*, 2007, 4212-4214.
18. C. Ling and K. Suto, *Chemistry of Materials*, 2017, **29**, 3731-3739.
19. E. Levi, E. Lancry, A. Mitelman, D. Aurbach, O. Isnard and D. Djurado, *Chemistry of Materials*, 2006, **18**, 3705-3714.
20. J. K. Burdett and J. H. Lin, *Inorganic chemistry*, 1982, **21**, 5-10.
21. F. Thole, L. F. Wan and D. Prendergast, *Phys. Chem. Chem. Phys.*, 2015, **17**, 22548-22551.
22. X. Sun, P. Bonnick and L. F. Nazar, *ACS Energy Letters*, 2016, **1**, 297-301.
23. M. D. Levi, E. Lancry, H. Gizbar, Z. Lu, E. Levi, Y. Gofer and D. Aurbach, *Journal of The Electrochemical Society*, 2004, **151**, A1044-A1051.
24. X. Sun, P. Bonnick, V. Duffort, M. Liu, Z. Rong, K. A. Persson, G. Ceder and L. F. Nazar, *Energy & Environmental Science*, 2016, **9**, 2273-2277.
25. L. F. Wan, B. R. Perdue, C. A. Apblett and D. Prendergast, *Chemistry of Materials*, 2015, **27**, 5932-5940.
26. Y. Cheng, L. R. Parent, Y. Shao, C. Wang, V. L. Sprenkle, G. Li and J. Liu, *Chemistry of Materials*, 2014, **26**, 4904-4907.
27. S. U. Kim, B. Perdue, C. A. Apblett and V. Srinivasan, *Journal of The Electrochemical Society*, 2016, **163**, A1535-A1542.
28. Z. Feng, X. Chen, L. Qiao, A. L. Lipson, T. T. Fister, L. Zeng, C. Kim, T. Yi, N. Sa, D. L. Proffit, A. K. Burrell, J. Cabana, B. J. Ingram, M. D. Biegalski, M. J. Bedzyk and P. Fenter, *ACS Applied Materials & Interfaces*, 2015, **7**, 28438-28443.
29. K. Chunjoong, P. P. J., K. Baris, Y. Tanghong, N. Dennis, Y. Young‐Sang, B. R. D., H. Sang‐Don, H. Meinan, Z. Zhengcheng, B. A. K., K. R. F. and C. Jordi, *Advanced Materials*, 2015, **27**, 3377-3384.
30. M. Cabello, R. Alcantara, F. Nacimiento, G. Ortiz, P. Lavela and J. L. Tirado, *CrystEngComm*, 2015, **17**, 8728-8735.
31. P. Bonnick, X. Sun, K.-C. Lau, C. Liao and L. F. Nazar, *The Journal of Physical Chemistry Letters*, 2017, **8**, 2253-2257.
32. V. V. Kulish, D. Koch and S. Manzhos, *Phys. Chem. Chem. Phys.*, 2017, **19**, 6076-6081.
33. A. Emly and A. Van der Ven, *Inorganic chemistry*, 2015, **54**, 4394-4402.
34. A. D., S. G. S., L. E., M. A., M. O., C. O. and B. M., *Advanced Materials*, 2007, **19**, 4260-4267.
35. M. D. Levi, E. Lancri, E. Levi, H. Gizbar, Y. Gofer and D. Aurbach, *Solid State Ionics*, 2005, **176**, 1695-1699.
36. G. S. Suresh, M. D. Levi and D. Aurbach, *Electrochimica Acta*, 2008, **53**, 3889-3896.
37. E. Levi, M. D. Levi, O. Chasid and D. Aurbach, *Journal of Electroceramics*, 2009, **22**, 13-19.
38. Y. Gu, Y. Katsura, T. Yoshino, H. Takagi and K. Taniguchi, *Sci. Rep.*, 2015, **5**, 12486.
39. G. Ceder, Y. M. Chiang, D. R. Sadoway, M. K. Aydinol, Y. I. Jang and B. Huang, *Nature*, 1998, **392**, 694.
40. K. Taniguchi, T. Yoshino, Y. Gu, Y. Katsura and H. Takagi, *Journal of The Electrochemical Society*, 2015, **162**, A198-A202.
41. A. Doron, W. Idit, G. Yosef and L. Elena, *The Chemical Record*, 2003, **3**, 61-73.
42. C. M. Fang, R. A. de Groot and C. Haas, *Physical Review B*, 1997, **56**, 4455-4463.
43. M. T. Czyżyk, R. Potze and G. A. Sawatzky, *Physical Review B*, 1992, **46**, 3729-3735.
44. M. Saubanère, M. B. Yahia, S. Lebègue and M. L. Doublet, *Nature Communications*, 2014, **5**, 5559.

45. B. Liu, T. Luo, G. Mu, X. Wang, D. Chen and G. Shen, *ACS Nano*, 2013, **7**, 8051-8058.
46. T. Kouji, G. Yunpeng, K. Yukari, Y. Takafumi and T. Hidenori, *Applied Physics Express*, 2016, **9**, 011801.
47. J. Kang, H. Sahin, H. D. Ozaydin, R. T. Senger and F. M. Peeters, *Physical Review B*, 2015, **92**, 075413.
48. E. Guilmeau, D. Berthebaud, P. R. N. Misse, S. Hébert, O. I. Lebedev, D. Chateigner, C. Martin and A. Maignan, *Chemistry of Materials*, 2014, **26**, 5585-5591.
49. M. Arsentev, A. Missyul, A. V. Petrov and M. Hammouri, *The Journal of Physical Chemistry C*, 2017, **121**, 15509-15515.
50. Y. Liang, H. D. Yoo, Y. Li, J. Shuai, H. A. Calderon, F. C. Robles Hernandez, L. C. Grabow and Y. Yao, *Nano Letters*, 2015, **15**, 2194-2202.
51. J. Desilvestro and O. Haas, *Journal of The Electrochemical Society*, 1990, **137**, 5C-22C.
52. H. Yuan, L. Jiao, J. Cao, X. Liu, M. Zhao and Y. Wang, *Journal of Materials Science and Technology*, 2004, **20**, 41-45.
53. R. Wang, C.-C. Chung, Y. Liu, J. L. Jones and V. Augustyn, *Langmuir*, 2017, **33**, 9314-9323.
54. M. E. Spahr, P. Novák, O. Haas and R. Nesper, *Journal of Power Sources*, 1995, **54**, 346-351.
55. P. Novák and J. Desilvestro, *Journal of The Electrochemical Society*, 1993, **140**, 140-144.
56. W.-h. Yu, D.-z. Wang, B. Zhu, S.-j. Wang and L.-x. Xue, *Solid State Communications*, 1987, **61**, 271-273.
57. G. Gershinsky, H. D. Yoo, Y. Gofer and D. Aurbach, *Langmuir*, 2013, **29**, 10964-10972.
58. B. Zhou, H. Shi, R. Cao, X. Zhang and Z. Jiang, *Phys. Chem. Chem. Phys.*, 2014, **16**, 18578-18585.
59. S. H. Lee, R. A. DiLeo, A. C. Marschilok, K. J. Takeuchi and E. S. Takeuchi, *ECS Electrochemistry Letters*, 2014, **3**, A87-A90.
60. N. Sa, H. Wang, D. L. Proffit, A. L. Lipson, B. Key, M. Liu, Z. Feng, T. T. Fister, Y. Ren, C.-J. Sun, J. T. Vaughey, P. A. Fenter, K. A. Persson and A. K. Burrell, *Journal of Power Sources*, 2016, **323**, 44-50.
61. G. Sai Gautam, P. Canepa, A. Abdellahi, A. Urban, R. Malik and G. Ceder, *Chemistry of Materials*, 2015, **27**, 3733-3742.
62. A. Parija, D. Prendergast and S. Banerjee, *ACS Applied Materials & Interfaces*, 2017, **9**, 23756-23765.
63. A. Mukherjee, N. Sa, P. J. Phillips, A. Burrell, J. Vaughey and R. F. Klie, *Chemistry of Materials*, 2017, **29**, 2218-2226.
64. A. Parija, Y. Liang, J. L. Andrews, L. R. De Jesus, D. Prendergast and S. Banerjee, *Chemistry of Materials*, 2016, **28**, 5611-5620.
65. G. S. Gautam, P. Canepa, R. Malik, M. Liu, K. Persson and G. Ceder, *Chemical Communications*, 2015, **51**, 13619-13622.
66. G. Sai Gautam, P. Canepa, W. D. Richards, R. Malik and G. Ceder, *Nano Letters*, 2016, **16**, 2426-2431.
67. N. Sa, T. L. Kinnibrugh, H. Wang, G. Sai Gautam, K. W. Chapman, J. T. Vaughey, B. Key, T. T. Fister, J. W. Freeland, D. L. Proffit, P. J. Chupas, G. Ceder, J. G. Bareno, I. D. Bloom and A. K. Burrell, *Chemistry of Materials*, 2016, **28**, 2962-2969.
68. V. Petkov, P. N. Trikalitis, E. S. Bozin, S. J. L. Billinge, T. Vogt and M. G. Kanatzidis, *J. Am. Chem. Soc.*, 2002, **124**, 10157-10162.
69. C. Delmas, H. Cognac-Auradou, J. M. Cocciantelli, M. Ménétrier and J. P. Doumerc, *Solid State Ionics*, 1994, **69**, 257-264.
70. T. Yao, Y. Oka and N. Yamamoto, *Journal of Materials Chemistry*, 1992, **2**, 337-340.
71. S. Tepavcevic, H. Xiong, V. R. Stamenkovic, X. Zuo, M. Balasubramanian, V. B. Prakapenka, C. S. Johnson and T. Rajh, *ACS Nano*, 2012, **6**, 530-538.
72. P. Novák, R. Imhof and O. Haas, *Electrochimica Acta*, 1999, **45**, 351-367.
73. W. Li, F. Cheng, Z. Tao and J. Chen, *The Journal of Physical Chemistry B*, 2006, **110**, 119-124.
74. J. Światowska-Mrowiecka, S. de Diesbach, V. Maurice, S. Zanna, L. Klein, E. Briand, I. Vickridge and P. Marcus, *The Journal of Physical Chemistry C*, 2008, **112**, 11050-11058.
75. T. S. Sian and G. B. Reddy, *Applied Surface Science*, 2004, **236**, 1-5.
76. T. S. Sian and G. B. Reddy, *Solid State Ionics*, 2004, **167**, 399-405.
77. L. F. Wan, J. T. Incorvati, K. R. Poeppelmeier and D. Prendergast, *Chemistry of Materials*, 2016, **28**, 6900-6908.
78. T. S. Sian, G. B. Reddy and S. M. Shivaprasad, *Electrochemical and Solid-State Letters*, 2006, **9**, A120-A122.
79. S. S. Tarsame, B. R. Gade and M. S. Sonnada, *Jpn. J. Appl. Phys.*, 2004, **43**, 6248.
80. J. W. Bullard and R. L. Smith, *Solid State Ionics*, 2003, **160**, 335-349.
81. C. Julien and G. A. Nazri, *Solid State Ionics*, 1994, **68**, 111-116.
82. C. Julien, O. Mohammad Hussain, L. El-Farh and M. Balkanski, *Solid State Ionics*, 1992, **53-56**, 400-404.
83. T. S. Arthur, R. Zhang, C. Ling, P.-A. Glans, X. Fan, J. Guo and F. Mizuno, *ACS Applied Materials & Interfaces*, 2014, **6**, 7004-7008.
84. J. T. Incorvati, L. F. Wan, B. Key, D. Zhou, C. Liao, L. Fuoco, M. Holland, H. Wang, D. Prendergast, K. R. Poeppelmeier and J. T. Vaughey, *Chemistry of Materials*, 2016, **28**, 17-20.
85. F. Sauvage, V. Bodenez, H. Vezin, T. A. Albrecht, J.-M. Tarascon and K. R. Poeppelmeier, *Inorganic chemistry*, 2008, **47**, 8464-8472.
86. D. B. Rogers, R. D. Shannon, A. W. Sleight and J. L. Gillson, *Inorganic chemistry*, 1969, **8**, 841-849.
87. M. D. Donakowski, A. Görne, J. T. Vaughey and K. R. Poeppelmeier, *J. Am. Chem. Soc.*, 2013, **135**, 9898-9906.
88. M. C. Bonatto, G. Ping, Z. K. Zhirong, M. Xiaoke, D. Thomas, P. Maxim, C. V. S. K., B. R. Juergen and F. Maximilian, *ChemElectroChem*, 2017, **4**, 738-745.
89. W. Kaveevivitchai and A. J. Jacobson, *Chemistry of Materials*, 2016, **28**, 4593-4601.
90. W. Kaveevivitchai and A. J. Jacobson, *Chemistry of Materials*, 2013, **25**, 2708-2715.
91. M. Sadakane, S. Ohmura, K. Kodato, T. Fujisawa, K. Kato, K.-i. Shimidzu, T. Murayama and W. Ueda, *Chemical Communications*, 2011, **47**, 10812-10814.
92. S. Masahiro, K. Katsunori, K. Takao, N. Yoshinobu, S. Kenji, S. Norihito, N. Takuro, M. Yoshio and U. Wataru, *Angewandte Chemie International Edition*, 2008, **47**, 2493-2496.
93. A. K. Padhi, K. S. Nanjundaswamy and J. B. Goodenough, *Journal of The Electrochemical Society*, 1997, **144**, 1188-1194.
94. Z. Gong and Y. Yang, *Energy & Environmental Science*, 2011, **4**, 3223-3242.

95. H. Kim, I. Park, D.-H. Seo, S. Lee, S.-W. Kim, W. J. Kwon, Y.-U. Park, C. S. Kim, S. Jeon and K. Kang, *J. Am. Chem. Soc.*, 2012, **134**, 10369-10372.
96. J.-M. Tarascon and M. Armand, in *Materials for Sustainable Energy*, Co-Published with Macmillan Publishers Ltd, UK, 2012, pp. 171-179.
97. C. Ling, D. Banerjee, W. Song, M. Zhang and M. Matsui, *Journal of Materials Chemistry*, 2012, **22**, 13517-13523.
98. G. K. P. Dathar, D. Sheppard, K. J. Stevenson and G. Henkelman, *Chemistry of Materials*, 2011, **23**, 4032-4037.
99. D. Morgan, A. Van der Ven and G. Ceder, *Electrochemical and Solid-State Letters*, 2004, **7**, A30-A32.
100. R. Zhang and C. Ling, *ACS Applied Materials & Interfaces*, 2016, **8**, 18018-18026.
101. X. Chen, F. L. Bleken, O. M. Løvvik and F. Vullum-Bruer, *Journal of Power Sources*, 2016, **321**, 76-86.
102. Z. Feng, J. Yang, Y. NuLi, J. Wang, X. Wang and Z. Wang, *Electrochemistry Communications*, 2008, **10**, 1291-1294.
103. Z. Feng, J. Yang, Y. NuLi and J. Wang, *Journal of Power Sources*, 2008, **184**, 604-609.
104. Y. Zheng, Y. NuLi, Q. Chen, Y. Wang, J. Yang and J. Wang, *Electrochimica Acta*, 2012, **66**, 75-81.
105. Y. NuLi, J. Yang, J. Wang and Y. Li, *The Journal of Physical Chemistry C*, 2009, **113**, 12594-12597.
106. Y. NuLi, J. Yang, Y. Li and J. Wang, *Chemical Communications*, 2010, **46**, 3794-3796.
107. Y. Li, Y. Nuli, J. Yang, T. Yilinuer and J. Wang, *Chinese Science Bulletin*, 2011, **56**, 386-390.
108. Y. NuLi, Y. Zheng, F. Wang, J. Yang, A. I. Minett, J. Wang and J. Chen, *Electrochemistry Communications*, 2011, **13**, 1143-1146.
109. Y. NuLi, Y. Zheng, Y. Wang, J. Yang and J. Wang, *Journal of Materials Chemistry*, 2011, **21**, 12437-12443.
110. Y. Orikasa, T. Masese, Y. Koyama, T. Mori, M. Hattori, K. Yamamoto, T. Okado, Z.-D. Huang, T. Minato, C. Tassel, J. Kim, Y. Kobayashi, T. Abe, H. Kageyama and Y. Uchimoto, *Sci. Rep.*, 2014, **4**, 5622.
111. R. Kitaura, F. Iwahori, R. Matsuda, S. Kitagawa, Y. Kubota, M. Takata and T. C. Kobayashi, *Inorganic chemistry*, 2004, **43**, 6522-6524.
112. C. A. K., F. Gérard and L. Thierry, *Angewandte Chemie International Edition*, 1999, **38**, 3268-3292.
113. S. L. Suib, *Annual Review of Materials Science*, 1996, **26**, 135-151.
114. Z. Yaming, Z. Haoguo, C. Zhenxia, C. Minqin, X. Yan, Z. Haoyu and Z. Dongyuan, *Angewandte Chemie*, 2001, **113**, 2224-2226.
115. R. Zhang, F. Mizuno and C. Ling, *Chemical Communications*, 2015, **51**, 1108-1111.
116. M. Pasta, C. D. Wessells, N. Liu, J. Nelson, M. T. McDowell, R. A. Huggins, M. F. Toney and Y. Cui, *Nature Communications*, 2014, **5**, 3007.
117. M. P. Shores, L. G. Beauvais and J. R. Long, *J. Am. Chem. Soc.*, 1999, **121**, 775-779.
118. S. Yagi, M. Fukuda, T. Ichitsubo, K. Nitta, M. Mizumaki and E. Matsubara, *Journal of The Electrochemical Society*, 2015, **162**, A2356-A2361.
119. K. Itaya, I. Uchida and V. D. Neff, *Accounts of Chemical Research*, 1986, **19**, 162-168.
120. H. Lee, Y.-I. Kim, J.-K. Park and J. W. Choi, *Chemical Communications*, 2012, **48**, 8416-8418.
121. Y. Mizuno, M. Okubo, E. Hosono, T. Kudo, H. Zhou and K. Oh-ishi, *The Journal of Physical Chemistry C*, 2013, **117**, 10877-10882.
122. M. Yutaka, I. Kazuhiro, K. Jungeun and T. Hiroshi, *Applied Physics Express*, 2009, **2**, 085001.
123. W. R. Y., S. Badri, S. K. H., W. J. Nelson, P. Mauro, L. Hyun‐Wook, T. M. F. and C. Yi, *Advanced Energy Materials*, 2015, **5**, 1401869.
124. C. D. Wessells, R. A. Huggins and Y. Cui, *Nature Communications*, 2011, **2**, 550.
125. Y. Lu, L. Wang, J. Cheng and J. B. Goodenough, *Chemical Communications*, 2012, **48**, 6544-6546.
126. W. Long, L. Yuhao, L. Jue, X. Maowen, C. Jinguang, Z. Dawei and G. J. B., *Angewandte Chemie International Edition*, 2013, **52**, 1964-1967.
127. C. D. Wessells, S. V. Peddada, R. A. Huggins and Y. Cui, *Nano Letters*, 2011, **11**, 5421-5425.
128. A. L. Lipson, S.-D. Han, S. Kim, B. Pan, N. Sa, C. Liao, T. T. Fister, A. K. Burrell, J. T. Vaughey and B. J. Ingram, *Journal of Power Sources*, 2016, **325**, 646-652.
129. R. Y. Wang, C. D. Wessells, R. A. Huggins and Y. Cui, *Nano Letters*, 2013, **13**, 5748-5752.
130. Y. Mizuno, M. Okubo, E. Hosono, T. Kudo, K. Oh-ishi, A. Okazawa, N. Kojima, R. Kurono, S.-i. Nishimura and A. Yamada, *Journal of Materials Chemistry A*, 2013, **1**, 13055-13059.
131. F. Wu and G. Yushin, *Energy & Environmental Science*, 2017, **10**, 435-459.
132. R. Malini, U. Uma, T. Sheela, M. Ganesan and N. G. Renganathan, *Ionics*, 2009, **15**, 301-307.
133. Y. Seung‐Ho, L. S. Hong, L. D. Jun, S. Yung‐Eun and H. Taeghwan, *Small*, 2016, **12**, 2146-2172.
134. C. Ling, R. Zhang and F. Mizuno, *ACS Applied Materials & Interfaces*, 2016, **8**, 4508-4515.
135. D. A. Kitchaev, S. T. Dacek, W. Sun and G. Ceder, *J. Am. Chem. Soc.*, 2017, **139**, 2672-2681.
136. B. Li, G. Rong, Y. Xie, L. Huang and C. Feng, *Inorganic chemistry*, 2006, **45**, 6404-6410.
137. J. Dai, S. F. Y. Li, K. S. Siow and Z. Gao, *Electrochimica Acta*, 2000, **45**, 2211-2217.
138. C. S. Johnson, M. F. Mansuetto, M. M. Thackeray, Y. Shao‐Horn and S. A. Hackney, *Journal of The Electrochemical Society*, 1997, **144**, 2279-2283.
139. D. A. Tompsett and M. S. Islam, *Chemistry of Materials*, 2013, **25**, 2515-2526.
140. M. M. Huie, D. C. Bock, E. S. Takeuchi, A. C. Marschilok and K. J. Takeuchi, *Coordination Chemistry Reviews*, 2015, **287**, 15-27.
141. C. Ling, R. Zhang, T. S. Arthur and F. Mizuno, *Chemistry of Materials*, 2015, **27**, 5799-5807.
142. R. Zhang, X. Yu, K.-W. Nam, C. Ling, T. S. Arthur, W. Song, A. M. Knapp, S. N. Ehrlich, X.-Q. Yang and M. Matsui, *Electrochemistry Communications*, 2012, **23**, 110-113.
143. R. Zhang, T. S. Arthur, C. Ling and F. Mizuno, *Journal of Power Sources*, 2015, **282**, 630-638.
144. S. Rasul, S. Suzuki, S. Yamaguchi and M. Miyayama, *Solid State Ionics*, 2012, **225**, 542-546.
145. Y. S. Meng and M. E. Arroyo-de Dompablo, *Energy & Environmental Science*, 2009, **2**, 589-609.
146. S. Rasul, S. Suzuki, S. Yamaguchi and M. Miyayama, *Electrochimica Acta*, 2013, **110**, 247-252.

147. J.-Y. Luo, J.-J. Zhang and Y.-Y. Xia, *Chemistry of Materials*, 2006, **18**, 5618-5623.
148. X. Wang and Y. Li, *J. Am. Chem. Soc.*, 2002, **124**, 2880-2881.
149. X. Sun, V. Duffort, B. L. Mehdi, N. D. Browning and L. F. Nazar, *Chemistry of Materials*, 2016, **28**, 534-542.
150. K. W. Nam, S. Kim, S. Lee, M. Salama, I. Shterenberg, Y. Gofer, J.-S. Kim, E. Yang, C. S. Park, J.-S. Kim, S.-S. Lee, W.-S. Chang, S.-G. Doo, Y. N. Jo, Y. Jung, D. Aurbach and J. W. Choi, *Nano Letters*, 2015, **15**, 4071-4079.
151. N. Balke, S. Jesse, A. N. Morozovska, E. Eliseev, D. W. Chung, Y. Kim, L. Adamczyk, R. E. García, N. Dudney and S. V. Kalinin, *Nature Nanotechnology*, 2010, **5**, 749.
152. P. Yu, B. N. Popov, J. A. Ritter and R. E. White, *Journal of The Electrochemical Society*, 1999, **146**, 8-14.
153. K. Xu and A. von Wald Cresce, *Journal of Materials Research*, 2012, **27**, 2327-2341.
154. T. Abe, H. Fukuda, Y. Iriyama and Z. Ogumi, *Journal of The Electrochemical Society*, 2004, **151**, A1120-A1123.
155. V. Duffort, X. Sun and L. F. Nazar, *Chemical Communications*, 2016, **52**, 12458-12461.
156. F. Xiong, Y. Fan, S. Tan, L. Zhou, Y. Xu, C. Pei, Q. An and L. Mai, *Nano Energy*, 2018, **47**, 210-216.
157. H. Liu, X. Shi, F. Xu, L. Zhang, W. Zhang, L. Chen, Q. Li, C. Uher, T. Day and G. J. Snyder, *Nature materials*, 2012, **11**, 422.
158. M. A. Korzhuev, *Physics of the Solid State*, 1998, **40**, 217-219.
159. M. K. Balapanov, R. A. Yakshibaev and U. K. Mukhamed'yanov, *Physics of the Solid State*, 2003, **45**, 634-638.
160. C. Jordi, M. Laure, L. Dominique and P. M. Rosa, *Advanced Materials*, 2010, **22**, E170-E192.
161. R. G. Pearson, *J. Chem. Educ.*, 1968, **45**, 581.
162. K. He, Z. Yao, S. Hwang, N. Li, K. Sun, H. Gan, Y. Du, H. Zhang, C. Wolverton and D. Su, *Nano Letters*, 2017, **17**, 5726-5733.
163. Y. Tashiro, K. Taniguchi and H. Miyasaka, *Electrochimica Acta*, 2016, **210**, 655-661.
164. R. Zhang, C. Ling and F. Mizuno, *Chemical Communications*, 2015, **51**, 1487-1490.
165. S. Renault, D. Brandell, T. Gustafsson and K. Edstrom, *Chemical Communications*, 2013, **49**, 1945-1947.
166. Z. Song and H. Zhou, *Energy & Environmental Science*, 2013, **6**, 2280-2301.
167. W. Deng, X. Liang, X. Wu, J. Qian, Y. Cao, X. Ai, J. Feng and H. Yang, *Sci. Rep.*, 2013, **3**, 2671.
168. L. Yanliang, T. Zhanliang and C. Jun, *Advanced Energy Materials*, 2012, **2**, 742-769.
169. H. Sano, H. Senoh, M. Yao, H. Sakaebe and T. Kiyobayashi, *Chemistry Letters*, 2012, **41**, 1594-1596.
170. M. Yao, H. Senoh, S.-i. Yamazaki, Z. Siroma, T. Sakai and K. Yasuda, *Journal of Power Sources*, 2010, **195**, 8336-8340.
171. B. Pan, D. Zhou, J. Huang, L. Zhang, A. K. Burrell, J. T. Vaughey, Z. Zhang and C. Liao, *Journal of The Electrochemical Society*, 2016, **163**, A580-A583.
172. H. Senoh, H. Sakaebe, H. Sano, M. Yao, K. Kuratani, N. Takeichi and T. Kiyobayashi, *Journal of The Electrochemical Society*, 2014, **161**, A1315-A1320.
173. P. Baofei, H. Jinhua, F. Zhenxing, Z. Li, H. Meinan, Z. Lu, V. J. T., B. M. J., F. Paul, Z. Zhengcheng, B. A. K. and L. Chen, *Advanced Energy Materials*, 2016, **6**, 1600140.
174. Z. Song, Y. Qian, X. Liu, T. Zhang, Y. Zhu, H. Yu, M. Otani and H. Zhou, *Energy & Environmental Science*, 2014, **7**, 4077-4086.
175. B. Jan, P. Klemen, B. Tanja, G. Miran, G. Boštjan, R. V. Anna and D. Robert, *ChemSusChem*, 2015, **8**, 4128-4132.
176. S. Tepavcevic, Y. Liu, D. Zhou, B. Lai, J. Maser, X. Zuo, H. Chan, P. Král, C. S. Johnson, V. Stamenkovic, N. M. Markovic and T. Rajh, *ACS Nano*, 2015, **9**, 8194-8205.
177. S.-C. Lim, J. Lee, H. H. Kwak, J. W. Heo, M. S. Chae, D. Ahn, Y. H. Jang, H. Lee and S.-T. Hong, *Inorganic chemistry*, 2017, **56**, 7668-7678.
178. Y. P. Chabre, *Journal of The Electrochemical Society*, 1991, **138**, 329-330.
179. G. J. Browning and S. W. Donne, *Journal of Applied Electrochemistry*, 2005, **35**, 871-878.
180. C.-X. Zu and H. Li, *Energy & Environmental Science*, 2011, **4**, 2614-2624.
181. Y.-C. Lu, B. M. Gallant, D. G. Kwabi, J. R. Harding, R. R. Mitchell, M. S. Whittingham and Y. Shao-Horn, *Energy & Environmental Science*, 2013, **6**, 750-768.
182. J. G. Smith, J. Naruse, H. Hiramatsu and D. J. Siegel, *Chemistry of Materials*, 2016, **28**, 1390-1401.
183. , !!! INVALID CITATION !!!
184. Z. Peng, S. A. Freunberger, Y. Chen and P. G. Bruce, *Science*, 2012.
185. G. Girishkumar, B. McCloskey, A. C. Luntz, S. Swanson and W. Wilcke, *The Journal of Physical Chemistry Letters*, 2010, **1**, 2193-2203.
186. P. Hartmann, C. L. Bender, M. Vračar, A. K. Dürr, A. Garsuch, J. Janek and P. Adelhelm, *Nature materials*, 2012, **12**, 228.
187. B. C. L., H. Pascal, V. Miloš, A. Philipp and J. Jürgen, *Advanced Energy Materials*, 2014, **4**, 1301863.
188. X. Ren and Y. Wu, *J. Am. Chem. Soc.*, 2013, **135**, 2923-2926.
189. G. Vardar, E. G. Nelson, J. G. Smith, J. Naruse, H. Hiramatsu, B. M. Bartlett, A. E. S. Sleightholme, D. J. Siegel and C. W. Monroe, *Chemistry of Materials*, 2015, **27**, 7564-7568.
190. J. Lu, L. Li, J.-B. Park, Y.-K. Sun, F. Wu and K. Amine, *Chem. Rev.*, 2014, **114**, 5611-5640.
191. P. G. Bruce, S. A. Freunberger, L. J. Hardwick and J.-M. Tarascon, *Nature materials*, 2011, **11**, 19.
192. V. Viswanathan, J. K. Nørskov, A. Speidel, R. Scheffler, S. Gowda and A. C. Luntz, *The Journal of Physical Chemistry Letters*, 2013, **4**, 556-560.
193. B. D. McCloskey, J. M. Garcia and A. C. Luntz, *The Journal of Physical Chemistry Letters*, 2014, **5**, 1230-1235.
194. T. Shiga, Y. Hase, Y. Kato, M. Inoue and K. Takechi, *Chemical Communications*, 2013, **49**, 9152-9154.
195. T. Shiga, Y. Hase, Y. Yagi, N. Takahashi and K. Takechi, *The Journal of Physical Chemistry Letters*, 2014, **5**, 1648-1652.
196. Q. Dong, X. Yao, J. Luo, X. Zhang, H. Hwang and D. Wang, *Chemical Communications*, 2016, **52**, 13753-13756.
197. G. Vardar, J. G. Smith, T. Thompson, K. Inagaki, J. Naruse, H. Hiramatsu, A. E. S. Sleightholme, J. Sakamoto, D. J. Siegel and C. W. Monroe, *Chemistry of Materials*, 2016, **28**, 7629-7637.
198. T. H. Hwang, D. S. Jung, J.-S. Kim, B. G. Kim and J. W. Choi, *Nano Letters*, 2013, **13**, 4532-4538.
199. E. Ran, S. Gregory, G. Arnd, P. Alexander and A. Doron, *Advanced Materials*, 2011, **23**, 5641-5644.
200. X. Ji, K. T. Lee and L. F. Nazar, *Nature materials*, 2009, **8**, 500.

201. X. Sen, Y. Ya‐Xia, G. Yu‐Guo and W. Li‐Jun, *Advanced Materials*, 2014, **26**, 1261-1265.
202. T. Gao, M. Noked, A. J. Pearse, E. Gillette, X. Fan, Y. Zhu, C. Luo, L. Suo, M. A. Schroeder, K. Xu, S. B. Lee, G. W. Rubloff and C. Wang, *J. Am. Chem. Soc.*, 2015, **137**, 12388-12393.
203. A. Du, Z. Zhang, H. Qu, Z. Cui, L. Qiao, L. Wang, J. Chai, T. Lu, S. Dong, T. Dong, H. Xu, X. Zhou and G. Cui, *Energy & Environmental Science*, 2017, **10**, 2616-2625.
204. Y. Diao, K. Xie, S. Xiong and X. Hong, *Journal of Power Sources*, 2013, **235**, 181-186.
205. C. Barchasz, J.-C. Leprêtre, F. Alloin and S. Patoux, *Journal of Power Sources*, 2012, **199**, 322-330.
206. Z. K. Zhirong, Z. Xiangyu, W. Di, D. Thomas, B. R. Jürgen and F. Maximilian, *Advanced Energy Materials*, 2015, **5**, 1401155.
207. G. Tao, J. Xiao, H. Singyuk, F. Xiulin, L. Xiaogang, Y. Chongying, H. Fudong, W. Fei, J. Jianjun, X. Kang and W. Chunsheng, *Advanced Materials*, 2018, **30**, 1704313.
208. H. S. Kim, T. S. Arthur, G. D. Allred, J. Zajicek, J. G. Newman, A. E. Rodnyansky, A. G. Oliver, W. C. Boggess and J. Muldoon, *Nature Communications*, 2011, **2**, 427.
209. L. Wanfei, C. Shuang, W. Jian, Q. Yongcai, Z. Zhaozhao, L. Hongzhen, N. Sanjay, M. Qian, X. Yan, Y. Fangmin, L. Meinan, Z. Lisha and Z. Yuegang, *Angewandte Chemie International Edition*, 2016, **55**, 6406-6410.
210. G. Tao, H. Singyuk, W. Fei, M. Zhaohui, L. Xiaogang, X. Kang and W. Chunsheng, *Angewandte Chemie International Edition*, 2017, **56**, 13526-13530.
211. X. Yu and A. Manthiram, *ACS Energy Letters*, 2016, **1**, 431-437.
212. B. P. Vinayan, Z. Zhao-Karger, T. Diemant, V. S. K. Chakravadhanula, N. I. Schwarzburger, M. A. Cambaz, R. J. Behm, C. Kubel and M. Fichtner, *Nanoscale*, 2016, **8**, 3296-3306.
213. T. Gao, S. Hou, K. Huynh, F. Wang, N. Eidson, X. Fan, F. Han, C. Luo, M. Mao, X. Li and C. Wang, *ACS Applied Materials & Interfaces*, 2018, **10**, 14767-14776.
214. S.-B. Son, T. Gao, S. P. Harvey, K. X. Steirer, A. Stokes, A. Norman, C. Wang, A. Cresce, K. Xu and C. Ban, *Nature Chemistry*, 2018, **10**, 532-539.
215. H. Tian, T. Gao, X. Li, X. Wang, C. Luo, X. Fan, C. Yang, L. Suo, Z. Ma, W. Han and C. Wang, *Nature Communications*, 2017, **8**, 14083.
216. G. Tao, H. Fudong, Z. Yujie, S. Liumin, L. Chao, X. Kang and W. Chunsheng, *Advanced Energy Materials*, 2015, **5**, 1401507.
217. Y. Cheng, H. J. Chang, H. Dong, D. Choi, V. L. Sprenkle, J. Liu, Y. Yao and G. Li, *Journal of Materials Research*, 2016, **31**, 3125-3141.
218. S. Yagi, T. Ichitsubo, Y. Shirai, S. Yanai, T. Doi, K. Murase and E. Matsubara, *Journal of Materials Chemistry A*, 2014, **2**, 1144-1149.
219. W. Na, Y. Zhen‐Zhong, Y. Hu‐Rong, Y. Ya‐Xia, G. Lin and G. Yu‐Guo, *Angewandte Chemie International Edition*, 2015, **54**, 5757-5761.
220. Z. Ye, X. Junjie, H. Yanlin and L. Chilin, *Advanced Functional Materials*, 2015, **25**, 7300-7308.
221. H. D. Yoo, Y. Liang, Y. Li and Y. Yao, *ACS Applied Materials & Interfaces*, 2015, **7**, 7001-7007.
222. Q. Miao, Y. NuLi, N. Wang, J. Yang, J. Wang and S.-i. Hirano, *RSC Advances*, 2016, **6**, 3231-3234.
223. S. Su, Y. NuLi, Z. Huang, Q. Miao, J. Yang and J. Wang, *ACS Applied Materials & Interfaces*, 2016, **8**, 7111-7117.
224. S. Xiaoqi, D. Victor and N. L. F., *Advanced science*, 2016, **3**, 1600044.
225. A. Byeon, M.-Q. Zhao, C. E. Ren, J. Halim, S. Kota, P. Urbankowski, B. Anasori, M. W. Barsoum and Y. Gogotsi, *ACS Applied Materials & Interfaces*, 2017, **9**, 4296-4300.
226. Y. Meng, D. Wang, Y. Wei, K. Zhu, Y. Zhao, X. Bian, F. Du, B. Liu, Y. Gao and G. Chen, *Journal of Power Sources*, 2017, **346**, 134-142.
227. C. Pei, F. Xiong, J. Sheng, Y. Yin, S. Tan, D. Wang, C. Han, Q. An and L. Mai, *ACS Applied Materials & Interfaces*, 2017, **9**, 17060-17066.
228. F. Xin, G. R. Ranganathan, K. N. Ashok and Z. X. Song, *Advanced Energy Materials*, 2017, **7**, 1700317.
229. Y. Cheng, Y. Shao, J.-G. Zhang, V. L. Sprenkle, J. Liu and G. Li, *Chemical Communications*, 2014, **50**, 9644-9646.
230. J. Zheng, W. Deng, Z. Hu, Z. Zhuo, F. Liu, H. Chen, Y. Lin, W. Yang, K. Amine, R. Li, J. Lu and F. Pan, *ACS Energy Letters*, 2018, **3**, 65-71.
231. M. Cabello, R. Alcántara, F. Nacimiento, P. Lavela, M. J. Aragón and J. L. Tirado, *Electrochimica Acta*, 2017, **246**, 908-913.
232. Y. Li, Q. An, Y. Cheng, Y. Liang, Y. Ren, C.-J. Sun, H. Dong, Z. Tang, G. Li and Y. Yao, *Nano Energy*, 2017, **34**, 188-194.
233. X. Bian, Y. Gao, Q. Fu, S. Indris, Y. Ju, Y. Meng, F. Du, N. Bramnik, H. Ehrenberg and Y. Wei, *Journal of Materials Chemistry A*, 2017, **5**, 600-608.
234. H. Dong, Y. Li, Y. Liang, G. Li, C.-J. Sun, Y. Ren, Y. Lu and Y. Yao, *Chemical Communications*, 2016, **52**, 8263-8266.
235. M. Walter, K. V. Kravchyk, M. Ibáñez and M. V. Kovalenko, *Chemistry of Materials*, 2015, **27**, 7452-7458.
236. M. Cabello, F. Nacimiento, R. Alcántara, P. Lavela, G. Ortiz and J. L. Tirado, *Journal of The Electrochemical Society*, 2016, **163**, A2781-A2790.
237. J.-H. Cho, M. Aykol, S. Kim, J.-H. Ha, C. Wolverton, K. Y. Chung, K.-B. Kim and B.-W. Cho, *J. Am. Chem. Soc.*, 2014, **136**, 16116-16119.
238. Y. Gofer, O. Chusid, H. Gizbar, Y. Viestfrid, H. E. Gottlieb, V. Marks and D. Aurbach, *Electrochemical and Solid-State Letters*, 2006, **9**, A257-A260.

A Critical Review on Cathodes for Rechargeable Mg Batteries

Minglei Mao, Tao Gao,* Singyuk Hou, Chunsheng Wang*

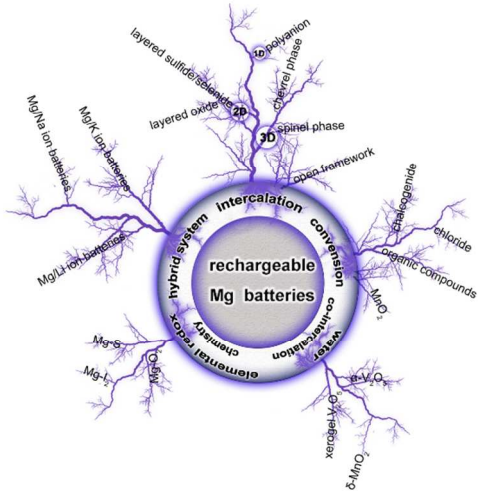

This review provide a critical and rigorous review on Mg battery cathodes, focusing on the impact of structure and composition on magnesiation kinetics.